Synthesis and characterization of $NaYGdF_4$ upconversion nanoparticles and an investigation of their effects on the spectroscopic properties of two phthalocyanine dyes.

A thesis submitted in fulfilment of the requirements for the degree of

MASTER OF SCIENCE

OF

RHODES UNIVERSITY

By

Jessica Mary Taylor

February 2014

ACKNOWLEDGEMENTS

I would like to express my most sincere gratitude to my supervisor, Dr Edith Antunes. Thank you so much for all your support, patience, guidance, encouragement, insight and time – I truly appreciate them and have sincerely enjoyed working with you. A special thank you to my co-supervisor, Professor T. Nyokong, for all her advice and for the many opportunities she has afforded me. I sincerely appreciate it. To Dr Christian Litwinski and to the team at Picoquant in Berlin, thank you for the fantastic Fluotime 300 and for all your assistance in acquiring and analysing upconversion fluorescence spectra. Many thanks, also, to my friend and colleague, Mr Matthew Coombs, for his assistance with powder diffraction and Rietveld refinement and to Ms Gail Cobus for all her administrative assistance.

To my friends and colleagues in the S22 research group – thank you so much for all your support, for your positivity and your understanding. You are a truly amazing group of people and I have enjoyed working alongside you. A special thank you, in particular, to Mr Adedayo Fashina for his kind advice and guidance.

Lastly, a big thank you to my friends and family for all their support and encouragement and especially to my boyfriend, Glyn, for all his help in getting through the last two years.

ABSTRACT

Sphere and star shaped $NaYGdF_4$:Yb/Er(Tm) upconversion nanoparticles were successfully synthesized utilizing a methanol assisted thermal decomposition approach and their chemical, spectroscopic and fluorescence properties were fully characterized. In addition, their influence on the spectroscopic and fluorescence properties of two phthalocyanines (Pcs) (unsubstituted tetrathiophenoxy phthalocyanine (H_2Pc) and aluminium octacarboxy phthalocyanine (Cl)AlOCPc) was investigated. Upconversion nanoparticles were found to produce characteristic upconversion fluorescence emissions in the blue, green, red and NIR regions and were also shown to possess paramagnetic properties. Simple mixing with an H_2Pc in toluene was found to exert no change on the spectroscopic or fluorescence properties of the Pc while covalent conjugation to a (Cl)AlOCPc resulted in a large Q band blue shift accompanied by a decrease in fluorescence lifetimes in DMSO. The red light excitation mediated singlet oxygen generation of the H_2Pc mixed with upconversion nanoparticles was investigated and singlet oxygen fluorescence lifetimes were found to decrease in the presence of the nanoparticles. Upconversion mediated singlet oxygen generation, by way of resonance energy transfer to the Pc, was also attempted using 972 nm excitation; however, no singlet oxygen was detected utilizing singlet oxygen NIR emission detection. Pending further work using alternative singlet oxygen detection methods, this suggests that while upconversion nanoparticles possess excellent fluorescent imaging capabilities, they are relatively inefficient in inducing singlet oxygen production simply when mixed with phthalocyanines. Despite this, by combining phthalocyanines and upconversion nanoparticles, we present a system capable of: multimodal imaging, using both upconversion and phthalocyanines emissions, singlet oxygen generation, via direct excitation of the phthalocyanine with red laser light, and, possibly, magnetic resonance imaging, as a result of doping the upconversion nanoparticles with Gd^{3+} ions.

TABLE OF CONTENTS

LIST OF ABBREVIATIONS

A/ abs	absorbance
ADC	analog to digital converter
ADMA	anthracene-9,10-diyl-bis-methylmalonate
APTES	3-aminopropyltriethoxysilane
CR	cross relaxation
DBU	1,8-diazabicyclo[5,4,0]undec-7-ene
DMAE	N,N-dimethylaminoethanol
DMF	dimethyl formamide
DMSO	dimethyl sulfoxide
DNA	deoxyribonucleic acid
DPBF	diphenylisobenzofuran
DPPH	2, 2-diphenyl-1-picrylhydrazyl
EDC	N-(3-dimethylaminopropyl)-N- ethylcarbodiimide
EPR	electron paramagnetic resonance
ESA	excited state absorption
ETU	energy transfer upconversion
F	fluorescence
FWHM	full width at half maximum

GSA	ground state absorption
HOMO	highest occupied molecular orbital
HRTEM	high resolution transmission electron microscopy
IC	internal conversion
ICDD	international centre for diffraction data
IRF	instrument response function
LUMO	lowest unoccupied molecular orbital
MCA	multichannel analyser
MRI	magnetic resonance imaging
NHS	N-hydroxysuccinimide
NIR	near infrared
NMR	nuclear magnetic resonance
NP	nanoparticle
OC	octacarboxy
P	phosphorescence
Pc	phthalocyanine
PDT	photodynamic therapy
PEI	polyethylenimine
PXRD	powder x-ray diffraction
RE	rare earth

ROS	reactive oxygen species
RWP	weighted profile residuals
S	singlet state
SHG	second harmonic generation
SOC	N-succinyl-N’-octyl chitosan
T	triplet state
TAC	time to amplitude converter
TC	tetracarboxy
TCSPC	time correlated single photon counting
TEM	transmission electron microscopy
TEOS	tetraethoxysilane
TGA	thermogravimetric analysis
TPA	two photon absorption
TSA	two step absorption
UC	upconversion
UCNP	upconversion nanoparticle
UV-vis	ultraviolet-visible

LIST OF SYMBOLS

S_0	singlet ground state
S_1	first singlet excited state
S_n	n^{th} singlet excited state
Φ	quantum yields
Φ_F	fluorescence quantum yield
Φ_Δ	singlet oxygen quantum yield
F	area under the fluorescence emission curve
A	fluorophore absorbencies
η	refractive index
τ, τ_F	fluorescence lifetime
τ_Δ	singlet oxygen fluorescence lifetime
k_f	radiative decay rate
k_{nr}	non-radiative decay rate
λ	wavelength
R	rate of photodegradation
I	rate of light absorbance
d	mean particle size
k	shape factor constant

β	peripheral position/ full width at half maximum/ hexagonal
α	non-peripheral position/ cubic
θ	Bragg angle
T_1	first triplet exited state
T_n	n^{th} triplet excited state

LIST OF FIGURES

LIST OF SCHEMES

LIST OF TABLES

Chapter 1

Introduction

1.1 Nanoparticles and nanotechnology

"In the year 2000, when they look back at this age, they will wonder why it was not until the year 1960 that anybody began seriously to move in this direction" is a rather prophetic quote from Richard Feynman's entertaining and very aptly named speech, *There's plenty of room at the bottom* [1]. The "direction" referred to by Feynman is nanoscience, and it has become one of the most important and most studied fields in modern day scientific research, possessing massive industrial, commercial and technological potential.

The prefix 'nano', refers to dimensions in the range of one billionth of a metre while 'nanomaterials' refer specifically to atomic clusters with a length of 100 nm or less in at least one dimension [2, 3]. Based on this definition, nanomaterials may be loosely classified into one of three categories, namely: quantum wells (where spatial confinement occurs in one dimension), quantum wires (where confinement occurs in 2 dimensions) and quantum dots (where all dimensions are spatially confined) [2]. The consequence of this spatial confinement leads to the appearance of unique properties in certain materials which are not observed in bulk states. The dependence of a particular material's properties on its size results from the fact that each property possesses a critical length over which it operates [4]. Once the dimensions of a material approximate this length, adherence to the laws governing some bulk state properties ceases and new properties arise [4]. A good example is the effect of quantum confinement in semiconductor quantum dots [5]. Here, electronic energy levels take on distinct values when the particle size is smaller than that of the exciton Bohr radius between the hole and electron pair, resulting in a tuneable band gap inversely proportional to particle size [5]. Another factor influencing the unique characteristics of some nanomaterials is their large surface area to volume ratio [3]. With a larger proportion of constituent atoms at the surface, some nanoparticles possess unusual properties with regards to thermal stability [3]. For instance, a significant decrease in melting temperature has been observed for indium nanostructures of 10 nm when compared to those of 100 nm [6]. Other interesting properties of some nanoparticles include superparamagnetism [7, 8], electric field effects [9], surface plasmon resonance [10, 11] and remarkable optical attributes [12].

The fabrication of nanoparticles may be achieved by several processes using one of two approaches: bottom up or top down [13]. Bottom up methods, as might be inferred from their title, involve the construction of nanoparticles from smaller atomic units, i.e. via chemical synthesis [13]. Top down methods, in contrast, involve the breakup of larger scale materials using methods such as ball milling [13]. Nanomaterials are versatile in their composition and may include inorganic crystals such as metal oxides [14, 15], sulfides [16] and fluorides [17], metallic particles [18, 19], various carbon allotropes [20], metalloids [21], amalgamated organic molecules like dendrimers [22] and polymers [23], as well as naturally occurring, large biological molecules such as DNA [24]. The application potential of nanomaterials is great indeed and they have found usage in many fields including renewable energy (in particular through the development of solar cells [25]), catalysis [26], environmental clean-up [27], data storage [28], quantum computing [29] and, naturally, medicine [30].

In the field of medicine, nanoparticles are especially advantageous not solely as a result of any unique properties they may possess, but because of their small size. Compared to bulk materials, such small particles are better able to enter living cells and tissue. In particular, nanoparticles have been shown to readily enter the tissue of solid tumours, which possess leaky vasculature, in a phenomenon known as the enhanced permeability and retention effect [31]. Thus, they may act as effective drugs or drug carriers with the added advantage of possessing specific cell targeting through rational design and adjustment of their surface functionalities [32]. In addition to the treatment of disease, nanoparticles have also shown great potential in the field of medical diagnostics. This area in particular, is of great research interest for nanoparticles with fluorescent properties where they are applied in tissue imaging [33, 34] and fluorescence sensing [35]. At this point, it should be noted, that some fluorescent nanoparticles like quantum dots, possess their fluorescent properties because of their nanoscale spatial confinement. In the case of upconversion nanoparticles, which are the focus of this work, a unique type of fluorescence found in bulk materials has been applied to several fields which require the use of small materials, including medical diagnostics, through the use of nanoparticles.

1.2 A brief introduction to fluorescence

The following paragraphs aim to introduce the essential concepts and important characteristics of fluorescence in order to facilitate later discussions concerning fluorescence in phthalocyanine dye molecules, lanthanide elements and, especially, upconversion, a special type of fluorescence found in some rare earth doped materials.

The phenomenon of fluorescence, its provenance within a system composed of electronic excited states as well as other processes associated with it, are best elucidated though the utilization of a Jablonski diagram (Figure 1.1). Figure 1.1 displays the excited states and associated energy transfer processes of the two spin multiplicities which exist for neutral organic molecules where multiplicity refers to "the number of possible orientations, calculated as 2S + 1, of the spin angular momentum corresponding to a given total spin quantum number S" [36]. For singlet states, where all electrons are paired, the total spin is equal to 0 while for triplet states, 2 unpaired electrons with parallel spins result in a total spin of 1 [37]. In Figure 1.1, S_0, S_1 and S_n represent the ground state, first excited state and nth (2, 3 etc.) excited states respectively. Each electronic state also encompasses several smaller vibrational states [37-39]. Absorption of a photon results in the promotion of an electron occupying a state of singlet or triplet multiplicity to a higher excited state of the same multiplicity. At room temperature, absorption usually occurs from the lowest vibrational level of the ground state to another vibrational level of a higher excited state [37-40]. The higher probability of electron occupancy of the lowest vibrational level of the ground state is predicted by the Boltzmann distribution [37]. Once an electron is raised to an excited state, it may undergo one or more of several decay, or relaxation, processes. Decay processes which occur via the loss of photons are referred to as radiative processes and include fluorescence and phosphorescence. Decay via fluorescence always occurs between an excited state and the ground state where both states possess the same multiplicity [37-39]. Normally, fluorescent emissions originate from the lowest vibrational level of the lowest excited state [37-39]. In contrast, phosphorescence involves the decay of an electron from an excited state to a ground state where the multiplicities of those states are different [37-39]. Transitions between states of different multiplicities involve an electronic spin flip, which is quantum mechanically forbidden, and only

occur as a result of spin orbit coupling [37-39]. Consequently, phosphorescence takes place on a significantly longer timescale with a half-life between of 10^{-3} to 1 second and is often outcompeted by faster non-radiative relaxation processes [37-39].

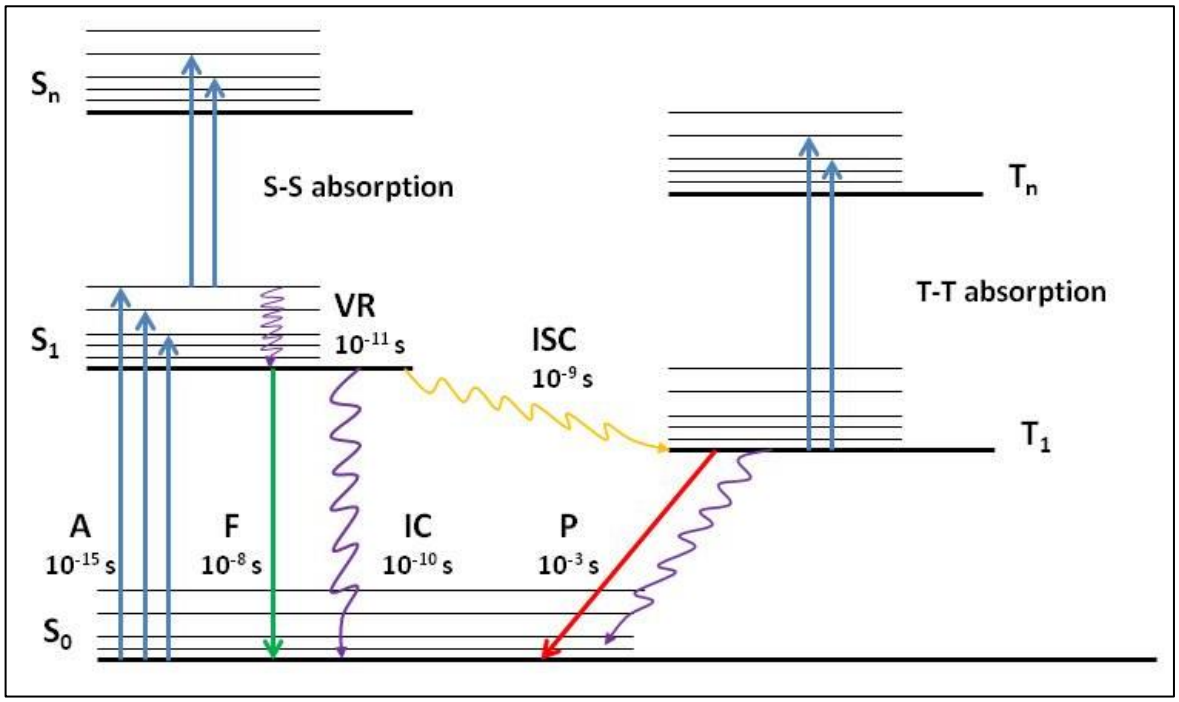

Figure 1.1: Modified Jablonski diagram depicting electronic transitions between the ground state and excited states as well as several non-radiative decay processes. S-S and T-T absorption refer to the excitation of electrons already occupying an excited singlet (S) or triplet (T) state. A = absorption, F = fluorescence, P = phosphorescence, VR = vibrational relaxation, IC = internal conversion and ISC = intersystem crossing. S_0 = singlet ground state, S_1 = first singlet excited state, S_n = nth singlet excited state. T_1 = first triplet excited state, T_n = nth triplet excited state.

Non-radiative relaxation refers to energy loss not accompanied by the emission of a photon [36]. A system in a particular excited state may undergo decay transitions to the lowest vibrational levels of the same excited state or to vibrational levels of lower excited (or ground) states of the same multiplicity [37, 39, 40]. These processes are referred to as vibrational relaxation and internal conversion respectively and result from the conversion, and subsequent loss, of the absorbed energy into heat energy through molecular vibrations and collisions [37-39]. Similar to internal conversion is

intersystem crossing which occurs between two states of dissimilar multiplicities and, like phosphorescence, is spin forbidden, occurring only as a result of spin orbit coupling [37-39].

1.2.1 Characteristics of fluorescence

In most fluorescent molecules, or fluorophores, the emissions produced possess several important traits [37, 38]. Firstly, emission spectra are generally noted to be red shifted (or lower in energy) in comparison to their corresponding excitation spectra. This observation is referred to as a Stokes shift and results from the fact that, regardless of the energy used to excite a particular system, the primary emission will always originate from the first (or lowest) excited state as stipulated by Kasha's rule [41] . The relaxation of electrons from higher excited states to the S_1 level is facilitated by ultrafast non-radiative energy loss where the energy gap between the higher excited states is small and allows for possible overlapping of vibrational sublevels. Contrastingly, the energy difference between the S_1 and S_0 (ground state) level is large, allowing slower decay by fluorescence to effectively compete with non-radiative relaxation. Excitation itself occurs with the highest probability when not accompanied by changes in nuclear position or momentum according to the Franck – Condon principle [37, 38]. This is because the absorption processes occur far faster than nuclear oscillations. After absorption has promoted an electron to a higher excited state, the excited state nucleus may adjust its position through oscillation resulting in a loss of vibrational energy and subsequent decay of the excited electron to a lower vibrational sublevel. Thus, fluorescent emissions often originate from the lowest vibrational sublevels of the S_1 excited state. The vibrational sublevels existing in the S_0, S_1 and S_n excited states possess very similar distributions and since absorption and emission processes involve the same transitions, emission and absorbance spectra are very often observed to be mirror images. Deviation from the mirror image trend is indicative of changes in molecular geometry or of excited state reactions involving the fluorophore.

1.2.2 Fluorescence quantum yields and lifetimes

Fluorescence emissions may be expressed quantitatively utilizing quantum yields and lifetimes. Quantum yields are employed to convey fluorescent emission productivity, especially in relation to other radiative and non-radiative de-excitation processes. Fluorescence quantum yields are expressed as the proportion of the total number of photons absorbed by the fluorophore which decay via fluorescence [42, 43]. Typically, quantum yields possess a value of less than one, owing to energy loss via competing decay mechanisms, and may be described as either relative or absolute where these terms refer to the experimental methods used in quantum yield acquisition. Absolute quantum yields are obtained utilizing specialized equipment such as integrating spheres [44] and photocalorimeters [45] while relative quantum yields are measured by comparing a sample's fluorescent emissions with that of a known standard [43]. The latter technique is more ubiquitous in experimental research owing to the relative ease with which it is performed; however, resulting quantum yields may be less reliable because of the technique's dependence on the standard's quantum yield value and the assumption that all factors influencing excitation of both the sample and standard are equal [43]. Quantum yields in this work have been recorded using the standard comparison method and Equation 1.1 [42]:

$$\Phi_F = \Phi_{Std} \frac{F.\ A_{Std}.\eta^2}{F_{Std}.\ A\ .\eta_{Std}^2} \qquad (1.1)$$

Here, Φ_F is the quantum yield of the sample and Φ_{Std} that of the standard; F and F_{std} represent the area under the fluorescence emission curve for the sample and standard respectively; A and A_{std} refer to the I of the sample and standard and η and η_{Std} are the refractive indices of the sample and standard solutions respectively.

The fluorescence lifetime refers to the time spent by a system in the excited state from which decay by fluorescence occurs and is equal to the reciprocal of the sum of the decay constants for all the relaxation processes acting upon the excited state, as illustrated by Equation 1.2 [46, 47]:

$$\tau = \frac{1}{(k_f + k_{nr})} \qquad (1.2)$$

where τ refers to the molecular fluorescence lifetime and k_f and k_{nr} represent rate constants for radiative and non-radiative decay processes respectively. Fluorescence lifetimes are intrinsic, or state properties, and therefore, they are characteristic of a particular fluorophore and independent of its concentration, as well as the excitation wavelength, intensity and time [46, 47]. They are widely used to investigate the radiative and non-radiative decay rates acting on fluorophore excited states, the interaction of these states with the environment (i.e. with solvents), as well as excited state reaction rates. Lifetime measurements are acquired using either time domain or frequency domain techniques. The most widely used time domain technique is time correlated single photon counting which has been used extensively in this work.

1.2.2.1 Time correlated single photon counting (TCSPC)

In time correlated single photon counting, the decay curve of a sample fluorophore is obtained utilizing pulsed excitation to generate emission photons which are detected, facilitating the incrementation of counts within a 'time bin' of a time channel array based upon the time taken between excitation and detection [38, 48, 49]. After multiple cycles of excitation and detection have been completed, the detected photons categorised by time channel take the form of a histogram with the photon counts plotted against time. The essential components of a TCSPC are displayed in Scheme 1.1. In the course of a measurement, a sample is excited by a pulsed light source (i.e. a flash lamp or diode laser) while a separate pulse is simultaneously sent to a time-to-amplitude converter (TAC) [38, 48, 49]. This initiates a 'start mode' and the subsequent charging of a capacitor within the TAC. The pulse sent to the sample results in the emission of a photon which is passed through a monochromator of a specified wavelength. It is then received by a detector (often a photomultiplier tube) where the signal is amplified [38, 48, 49]. At this point, the signal may have undergone shifts or

changes in its phase and amplitude, partly as a result of passing through the detector. This is corrected for by directing the signal through a constant fraction discriminator. Once the emission signal reaches the TAC, it initiates a 'stop mode' which halts the voltage accumulation in the capacitor. This voltage pulse is then converted to a digital signal by an analog to digital converter and sorted by amplitude within a multichannel analyser [38, 48, 49]. The final voltage pulse generated by the capacitor is proportional to the delay time between the start and stop modes; thus, the longer it takes for a photon to reach the TAC, the higher the capacitor voltage.

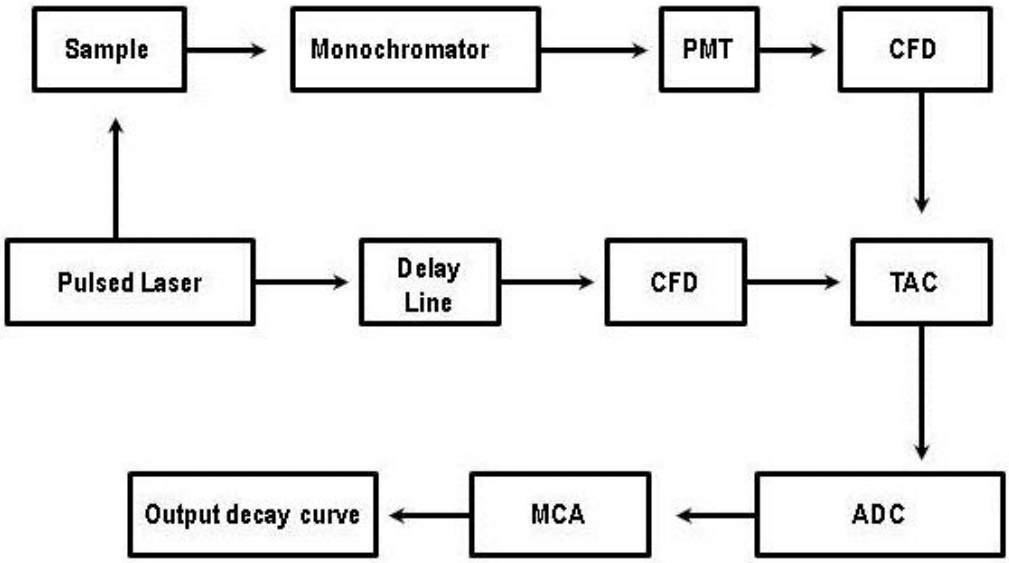

Scheme 1.1: Components of a typical TCSPC where PMT = Photomultiplier tube, CFD = Constant fraction discriminator, TAC= Time to amplitude converter, ADC= Analog to digital converter and MCA = Multichannel analyser.

1.3 Fluorescence in inorganic fluorophores containing lanthanide ions

Fluorescence in inorganic solids can be facilitated by the intentional addition of impurities into a host material, typically a crystal or glass, in a process called doping [50, 51]. This differs from band model fluorescence in that emissions occur as a result of electronic transitions taking place at, or within, impurity centres (dopants) and not between valence and conduction bands where electrons are delocalised across a solid crystal lattice as in semiconducting quantum dots [50-52].The majority of

dopants are transition or rare earth metals. Within lanthanide rare earth centres, electronic transitions may occur via charge transfer and d-f or f-f orbital transitions [53, 54]. The latter are symmetry, or Laporte forbidden, transitions implying that they occur with low probability and display weak absorption spectra [53-55]. In the transition metals, d – orbitals often participate in the formation of chemical bonds, making their nuclear and electronic configurations highly sensitive to their immediate environment [53-55]. As a result, host lattice compositions, atomic positions and site symmetries in crystallographic unit cells can influence absorbance and fluorescence spectra to a great extent [56]. For atoms participating in bonding, nuclei may undergo positional shifts as excitation can result in the alteration of bond lengths, causing relatively large Stokes shifts and broad fluorescence bands [53-55]. In stark contrast, the 4f valence orbitals of the rare earth metals are shielded from environmental influences by the outer 5s and 5p subshells and do not participate directly in bonding [53-55]. It is this fundamental characteristic that makes the fluorescent properties of lanthanide metals both fascinating and unique and has initiated their application in numerous fluorescence related technologies. The shielding of the 4f orbitals generates emission spectra with especially narrow bandwidths and small Stokes shifts. As most lanthanide atoms possess a vast ladder-like arrangement of excited states, they are often able to produce more than one emission band and, together, their emissions range from the UV to the NIR regions [54].

As with all forbidden transitions, excited states tend to be long lived with fluorescence lifetimes commonly recorded in the millisecond range [57]. Symmetry forbidden transitions, however, also create a problem wherein successful excitation events are rare. In such instances, a common technique employed in many inorganic fluorophores is the inclusion of another dopant species, with a higher absorption coefficient, which passes absorbed energy to the fluorescent centre non-radiatively via resonance [50]. This is termed sensitization and may also be accomplished by the host lattice itself [50]. The longevity of the excited states in rare earth metals has also facilitated the occurrence of several interesting phenomena one of which is photon upconversion (UC).

1.3.1 Photon upconversion (UC)

Utilizing a comparison to normal fluorescence, discussed earlier, one might describe upconversion, in the most simplistic terms, as fluorescence 'backwards'. Unlike the vast majority of fluorophores, upconverters produce emission wavelengths which are shorter (and therefore higher in energy) than those used to excite them [57]. Emissions result from the relaxation of higher level excited states, effectively violating Kasha's rule and precipitating the appearance of large anti-stokes shifts.

Photon upconversion belongs to a group of several separate processes in which emission energies exceed excitation energies. These processes may be subdivided into two broad categories based upon whether they undergo single-photon or multi-photon absorption. Single-photon processes are uncommon and inefficient and include anti-stokes Raman emission [58]. This process considers the absorption of a photon by an ion already occupying an excited vibrational level as opposed to the ground state [58]. The ion is excited to a virtual, instantaneous, excited state from which it relaxes, not to the original excited vibrational level, but to the ground state resulting in the observed higher energy emissions. The most notable multi-photon processes are displayed below in Figure 1.2.

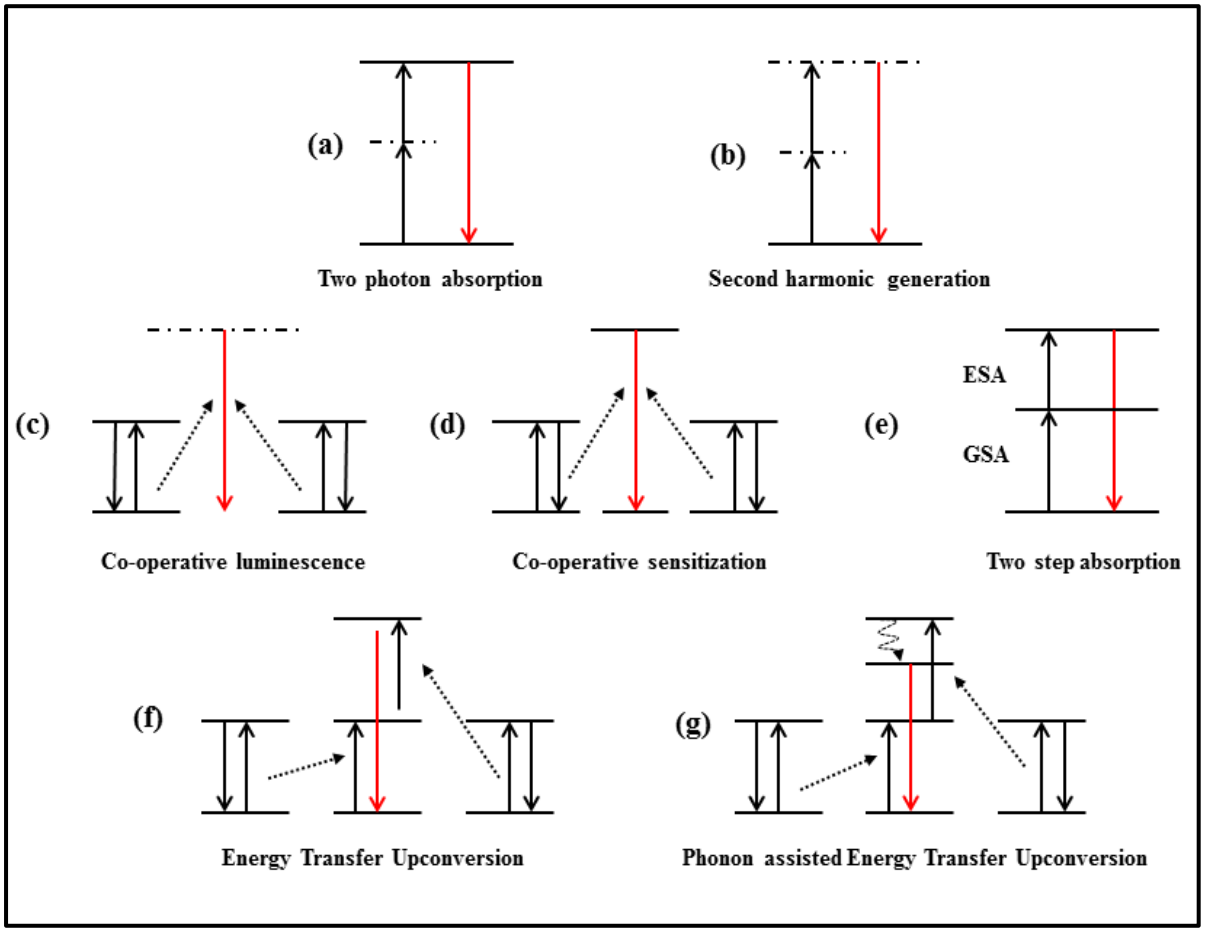

Figure 1.2: Multiphoton absorption processes where solid and dotted lines represent real and virtual excited states respectively. Revised from [58] and [57].

Key to differentiating between several of these processes is to secernate the real excited state and the virtual excited state. While excited states are discrete, stable energy levels which exist for electrons in a system, virtual states are described as instantaneous imaginary states occurring between defined excited states [59]. From a quantum mechanical perspective, they possess no eigen value and have no measurable lifetime.

Multiphoton absorption processes may be further classified as being either simultaneous or sequential. Simultaneous processes refer to the absorption of 2 photons at once, where a virtual excited state exists between the absorption of the first and second photon. The two best known examples are two photon absorption (TPA) [60, 61] and second harmonic generation (SHG) [62] . In TPA, the excited

state giving rise to fluorescence is real and photons being absorbed may be of unequal frequencies (Figure 1.2a). In contrast, the highest excited state in SHG is virtual and excitation photons must possess equal frequencies (Figure 1.2b). As a result, emission wavelengths are equal to half that of the excitation wavelength. Both processes are utilized extensively in laser technologies as well as in microscopy [63].

Sequential photon absorption processes include co-operative luminescence, co-operative sensitization, two step absorption (TSA) and energy transfer upconversion (ETU). These processes have been reviewed in [57, 58] and [64], from where the following explanations have been revised. In co-operative luminescence two separate ions each absorb a photon, promoting both ions to excited states (Figure 1.2c). The two photons then simultaneously relax to the ground state emitting one photon with the total energy of both absorbed photons from a virtual excited state (Figure 1.2c). Co-operative sensitisation is similar to co-operative luminescence; however, on the decay of the two excited states, the combined energy is used to excite a third ion (Figure 1.2d). The emission, in this case, results from the decay of a real excited state in the third ion, making it a more efficient process. TSA involves the ground state absorption (GSA) of a photon which promotes the system to a real, metastable, intermediate excited state (Figure 1.2e). This is followed by the absorption of a second photon (ESA) which initiates the occupation of a higher state, from where the system relaxes to the ground state, producing a single emission photon of higher energy (Figure 1.2e). Energy transfer upconversion involves the non-radiative resonance transfer of energy from one ion, decaying from an excited state to the ground state, to another ion (Figure 1.2f). This process may occur several times until the second ion is promoted to a certain higher energy excited state from which it decays, emitting a single photon with the combined energy of all those that had been absorbed (Figure 1.2f). ETU may involve a single or multiple ionic species. In the latter case, one acts specifically as a sensitizer and the other as an activator. ETU involving specific activator and sensitizer ions is referred to as sensitised ETU. In order for energy transfer to occur with high efficiency, the energy gaps between the excited and ground states of the activator and sensitizer atoms should be similar. When this is not the case, population of lower excited states of the activator may be assisted by the loss of vibrational energy in the form of phonons (Figure 1.2g).

The last two processes mentioned, TSA and ETU, may be referred to as true UC processes because all the involved intermediate and excited states are real [57, 58, 64] . Thus, they fulfil the fundamental requirement for upconversion in that the intermediate states possess determinate lifetimes. The long lifetime of an intermediate state is of crucial importance in UC systems. These states behave as excited photon reservoirs, effectively preserving an ion in an excited state long enough for it to be excited to a higher energy level upon the absorption of another photon. Generally, UC requires intermediate state lifetimes in the micro- to milli-second range and, consequentially, any process resulting in the decrease of excited state and intermediate lifetimes is highly undesirable [57]. These include phonon losses and cross relaxation (CR). Cross relaxation involves the excitation of one ion to a higher energy state utilising energy provided through resonant energy transfer by another ion undergoing decay [58]. In this way it is similar to ETU; however, in cross relaxation, neither ion is promoted to an excited state higher than that possessed by either ion initially.

1.3.2 Upconversion nanoparticles: activators, sensitizers and host lattices

While the investigation into UC fluorescence began in bulk materials, the vast majority of research publications appearing in the last 10 to 15 years have dealt with the application of this unique fluorescence mechanism to nanomaterials [65, 66].

The UC efficiency of a particular nanoparticle depends upon the identity of its activator and sensitizer atoms, the composition of the host lattice and the arrangement of atoms therein. The suitability of a particular ion to its role as an activator or sensitizer is largely dependent on its number and arrangement of excited states.

1.3.2.1 Activators and Sensitizers

Good activating ions should possess several excited 4f energy levels separated by similar differences in energy. Gaps separating energy levels should be small enough to facilitate inter excited state

transitions, yet large enough to decrease the probability of energy loss through vibrational processes [65, 66]. This is according to the energy gap law which denotes the exponential decrease in multi-phonon relaxation with an increase in the energy difference between two excited states [67]. The most effective and most commonly used activators in the lanthanide series include the Er^{3+}, Tm^{3+} and Ho^{3+} ions [68] with the former two having been used extensively in this work. Different activator atoms emit characteristic colours when doped into a host lattice. Er^{3+} ions produce green, red and occasionally blue emissions arising from the relaxation of electrons occupying the $^2H_{11/2}$ and $^4S_{3/2}$, $^4F_{9/2}$ and $^2H_{9/2}$ levels respectively [68, 69] (Figure 1.3). Tm^{3+} ions in contrast, produce blue emissions from the $^1D_2$ and $^1G_4$ levels; however, red fluorescence from the $^1G_4$ to $^3F_4$ is also observable [68, 69] (Figure 1.3). Tm^{3+} ions are also known to produce highly intense emissions in the NIR arising from de-excitation of the $^3H_4$ level. In the case of both ions, other emissions are possible and have been recorded [69]. The population of excited states in both Er^{3+} and Tm^{3+} is phonon assisted, with Er^{3+} emissions resulting from the absorption of 2 photons while the red and blue emissions in Tm^{3+} require the absorption of 3 photons.

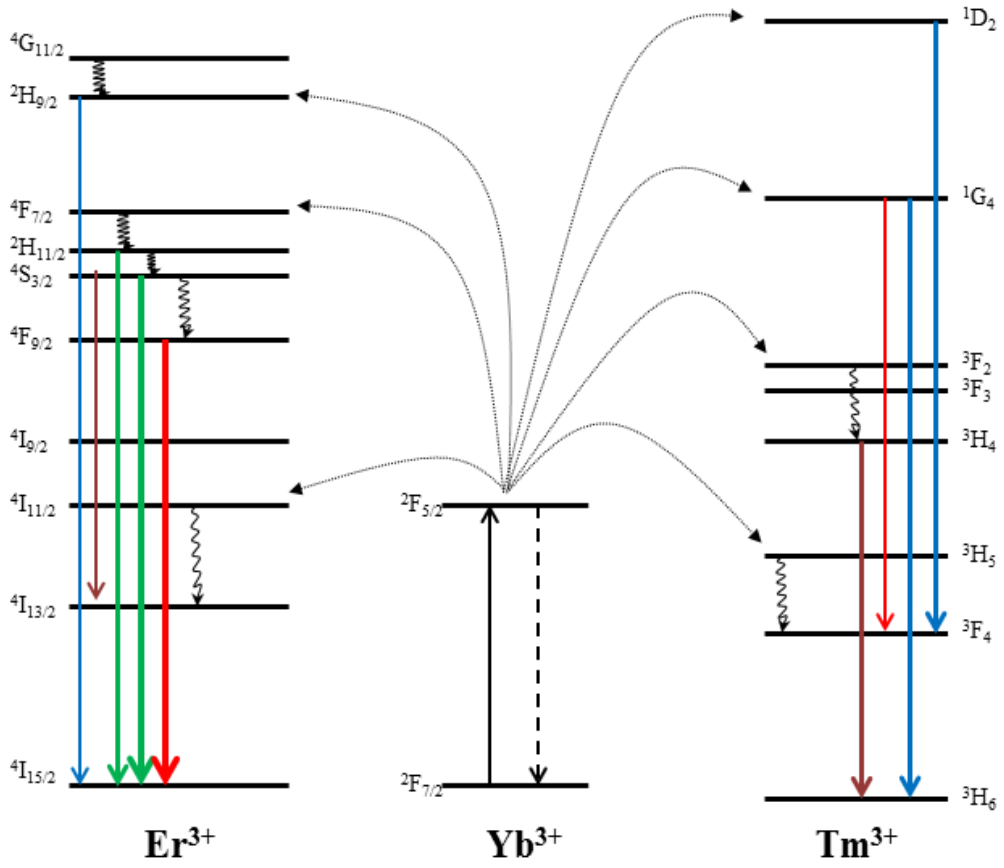

Figure 1.3: Electronic transitions giving rise to fluorescent emissions in Er^{3+} and Tm^{3+} ions via Yb^{3+} sensitization. Revised from [68].

Paradoxically, the emissions of activators are relatively intense despite transitions being Laporte forbidden. In f-f transitions, lifting of the Laporte rule can occur as a result of 'mixing' with orbitals of opposite parity i.e. 5d orbitals [70]. Parity mixing is a direct consequence of the crystal field splitting effect on shielded 4f orbitals and the influence of the host crystal field on the point symmetry of the lanthanide dopant, in particular, when the centrosymmetricity is disrupted [70]. These transitions are termed 'induced dipole transitions' and their probabilities and intensities may be explained and calculated using Judd-Ofelt theory [70].

The most effective and popular sensitizer employed for UC materials is the Yb^{3+} ion. Yb^{3+} possesses only one excited state, the $^2F_{5/2}$ level, from which it transfers energy to activator ions via ETU [68, 69]. The energy difference between the ground and excited states of Yb^{3+} is similar to those between

some energy levels in several activators including Ho^{3+}, Er^{3+} and Tm^{3+}. This effectively facilitates resonant energy transfer. As excitation of the activators is performed by the Yb^{3+} ion, it is possible to induce multi emission UC by exciting Yb^{3+} only. Consequently, several UC emissions may be obtained utilizing only one excitation wavelength at around 980 nm. The concentration of activator and sensitizer ions within a host lattice is of crucial importance for UC efficiency. Whilst it may seem counter-intuitive, high activator ion concentrations can induce higher rates of cross relaxation and greatly reduce UC emission intensities [71]. An optimum concentration of 2 – 3 mol % and 0.2 – 0.5 mol % has been determined for Er^{3+} and Tm^{3+} ions respectively [72]. Dissimilarly, sensitizer atoms are added at larger concentrations in order to facilitate closer proximity to activators and greater absorption. Yb^{3+} is usually added in concentrations between 18 – 25 mol % [72].

1.3.2.2 Host lattices

Ideal host lattices for UC materials should possess constituent ions with similar ionic radii to the lanthanide dopants to facilitate their inclusion in the lattice and minimise crystal defects which may reduce UC efficiency. Host lattice elements should also possess low phonon, or vibrational, energies as these result in excited state relaxation.

Many host lattices are based either on oxide or fluoride compounds. Oxide hosts include transition or rare earth metal oxides [73, 74], phosphates [75] and oxysulfides [76] and, while they are particularly stable, they also possess high phonon energies and, as a result, low UC efficiencies. In contrast, fluoride hosts experience relatively low phonon energies and are therefore considered to be superior. Fluoride hosts often occur as MF_3 or AMF_4 where M and A represent transition or rare earth metals and alkali or alkali earth metals respectively. A number of fluoride host lattices, with an accompanying variety of alkali and alkali earth metals, have been investigated to date [77-81]. However, the $NaYF_4$ host lattice is known to be the most effective [66].

1.3.3 Upconversion in $NaYF_4$: size, phase and shape control

The two most highly researched $NaYF_4$ UC nanocrystals are based on the notably efficient Tm^{3+} Yb^{3+} and Er^{3+} Yb^{3+} combinations. The UC efficiency in upconversion nanoparticles (UCNP's) is profoundly affected by the size and phase of the crystals. Two main crystallographic phases occur for this system: α, cubic, and β, hexagonal [82]. β phase crystals are known to possess higher thermodynamic stability than their α phase counterparts and produce UC emissions which are several orders of magnitude higher [83]. This is directly attributable to the symmetry of the crystallographic sites occupied by the rare earth ions within the unit cell as these sites possess lower symmetry in hexagonal crystals than in cubic ones [83]. This in turn encourages induced electronic dipole transitions. The control of phase within these crystal species has been a popular research topic in the literature in recent years. Key factors known to influence nanoparticle size and phase include reaction temperature and reaction time [84]. β phase crystal formation is favoured by higher temperature syntheses (280 ^{o}C or more) and longer reaction times. The effect of size is also important, where small sizes designate a high surface area to volume ratio and a subsequent reduction in UC emission intensity owing to quenching effects from solvents and capping agents. Another technique which has been shown to simultaneously control both size and phase is the addition of Gd^{3+} ions [85]. The inclusion of these large ions, was shown to lower crystal site symmetry in favour of the hexagonal phase and rearrange electron cloud distributions at the nanoparticle surface, thereby limiting crystal growth by repelling incoming F^- ions [85]. These effects were noted upon the inclusion of other large lanthanide atoms as well; however, only the Gd^{3+} ion, with its lowest excited state occupying a much higher energy position than any of the activator or sensitizer states involved in UC fluorescence, was found to have no detrimental effect on fluorescent emissions [85]. This use of Gd^{3+} in the phase and size control of UCNPs has been applied in this work.

1.3.4 Synthetic approaches

A number of synthetic approaches have been employed for UCNP synthesis. These include thermal decomposition [86, 87], co-precipitation [88, 89], hydro(solvo) thermal methods [90, 91], sol gel processing [74, 92] as well as combustion [93] and flame techniques [94] with the former three being employed ubiquitously. These processes have been reviewed in [65] and [95] from where the following points have been revised. Co-precipitation methods are relatively cheap, time efficient and simple and require no specialised reaction vessels. However, high temperature post-reaction annealing steps are often necessary in order to improve crystallinity. Hydro(solvo) thermal syntheses need no post-reaction annealing. They do, however, require high pressure reaction conditions and are usually carried out in sealed, steel walled autoclave reaction vessels. Thermal decomposition is used to produce monodispersed nanocrystals with good size distributions. This method involves the decomposition of metal precursors at high reaction temperatures and requires the use of high boiling point solvents, such as 1-octadecene. One disadvantage of thermal decomposition is the usage of metal triflouroacetate precursors which can cause the release of toxic gases. In some cases, these have been replaced by rare earth oleates [85]. Most synthetic techniques also require the use of chemical stabilizers, or surface capping agents, such as oleic acid [96], oleylamine [97], polyethylenimine (PEI) [98] and ethylenediaminetetraacetic acid (EDTA) [99]. The composition of the capping agent exerts a large influence on nanoparticle solubility, with many unmodified nanoparticles being hydrophobic. Where water dispersability or biological compatibility is desired, surfaces may be modified through processes like ligand exchange [100] or surface silanization [101]. The surface constitution of UCNPs may also affect their fluorescence through quenching and non-radiative energy loss.

1.3.5 Upconversion applications

Undeniably, the process of photon UC affords upconverting phosphors a multitude of applications and has been, amusingly but very aptly, described as the ‘El dorado’ of the fluorescence world by Ong and co-workers [102] . Apart from their application in the development of lasers [103], UC phosphors

have also shown promise in security and anti-counterfeiting fields [104-106], photovoltaic solar cells [107-109] and a variety of biological and medicinal applications. UCNPs in particular have been found to have great value in the fields of *in vivo* bioimaging [110-112] and bio assays [113, 114] as well as in chemical sensing [115]. The inclusion of Gd^{3+} ion dopants into UC phosphors has also allowed for their application as multi-modal imaging probes where Gd^{3+} ions facilitate additional imaging capabilities through magnetic resonance techniques.

1.3.5.1 The application of UCNPs in magnetic resonance imaging utilizing Gd^{3+} ion inclusion

Magnetic resonance imaging (MRI) is a powerful imaging technique used to evaluate diseased and/ or damaged tissue and has become a ubiquitous feature in the health care industry [116]. Hailed for being non-intrusive and for utilizing ionization free radiation, MRI is a now a popular alternative to traditional x-ray computed tomography techniques. The principle of MRI involves the relaxation of hydrogen nuclei within water molecules when inside a magnetic field [116]. The presence of a magnetic field results in the formation of two energy levels for the hydrogen nucleus based upon whether the spin induced magnetic moment of the nucleus aligns with or against the external magnetic field [116]. The majority of hydrogen nuclei possess magnetic moments which align parallel to the external field, resulting in their occupation of the lower of the two energy levels. Electromagnetic radiation excitation is used to promote the nuclei to the higher energy level after which they undergo relaxation [116]. The time taken for the relaxation of a hydrogen nucleus to occur is measured and used to generate an image. Relaxation times are dependent upon the local environment associated with the water molecule and, thus, different tissues within the body induce different relaxation times. Overall relaxation of a hydrogen nucleus encompasses two relaxation mechanisms, namely, T_1 and T_2 [116]. Although the relaxation times of various tissues do differ, often these differences are not great enough to induce distinguishable features in an image. To counter this problem, MRI techniques make use of contrast agents [117]. Such systems include chelates of highly paramagnetic metal ions like Gd^{3+} [117]. Gd^{3+} contrast agents are known to improve the contrast of tissue images by binding to water molecules and significantly reducing their T_1 relaxation time [118]. Gd^{3+} containing

nanoparticles have also been proven to act as excellent *in vivo* contrast agents in rats [118]. Recently, some of the focus on nanoparticle applications has moved to include the fabrication and design of multifunctional nano-systems by combining the functional properties of their constituent elements. One such example is the combined MRI and fluorescence imaging capability of Gd^{3+} doped UCNPs [119-122].

Fairly recently, UCNPS have also been investigated as simultaneous drug carriers and photon harvesters for deep tissue photodynamic therapy in conjunction with conventional, visible light absorbing photosensitizers. One class of photosensitizer, which has been investigated under such circumstances, is the phthalocyanine. By combining UCNPs with both Gd^{3+} and photosensitizer molecules it has been possible to create tri-functional nano-systems which may be applied to fluorescence imaging, MRI and photodynamic therapy simultaneously [123].

1.4. Phthalocyanine dyes: discovery, structure and applications

The term phthalocyanine (Pc), though certainly more recognizable to chemists, should be familiar to anyone who has dabbled in the art of painting. The pigments phthalocyanine blue and phthalocyanine green are ubiquitous inclusions in oil and water colour paint sets and industrially produced on tremendous scales. The early work regarding the discovery of phthalocyanines took place over a period of around thirty years, from the mid-1900s until the mid-1930s [124, 125], eventuating in their structural elucidation. The first observation of a Pc was made by Braun and Tcherniak in 1907 at a gas company in London during an attempt to synthesize *o*-cyanobenzamide where a blue, insoluble compound was made instead [124, 125]. Two more serendipitous observations of phthalocyanines were made sometime afterwards, in the mid-1920s, first by de Diebach's group, while studying dinitrile reactions, as well as by Dandridge at a Scottish dye factory during the preparation of phthalimide [124]. Dandridge, Drescher and Thomas went on to patent the synthesis of the then structurally unidentified blue pigment in 1928 [124]. Structural determination was finally achieved by Linstead in 1934 [126] and later confirmed by Robertson using X-ray diffraction [127].

Phthalocyanines are planar, macrocyclic, aromatic compounds possessing 18 delocalised π electrons and are related to the tetrapyrrole macrocycles of the porphyrin family (Figure 1.4).

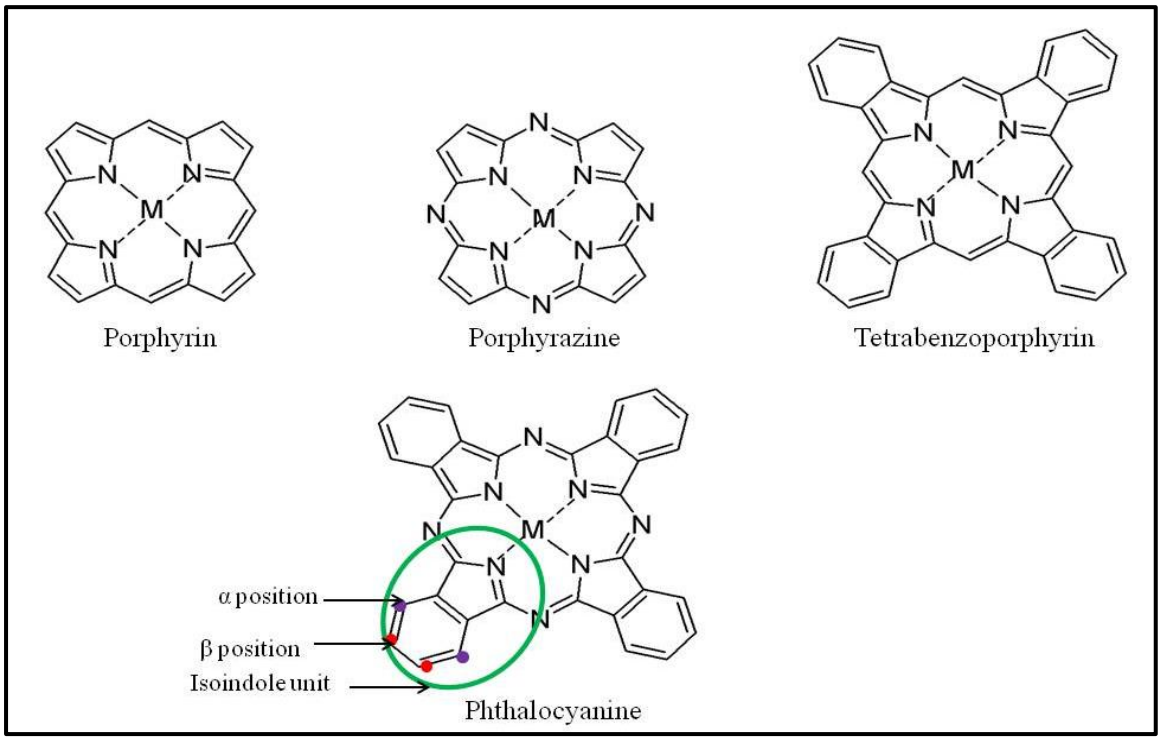

Figure 1.4: Structures of porphyrin, porphyrazine, tetrabenzoporphyrin and phthalocyanine molecules, showing the isoindole unit and α and β positions of the phthalocyanine.

Phthalocyanines consist of four isoindole units which are linked through 4 aza (nitrogen) groups. Their chemical and physical properties may be refined through alterations to their structure. For example, the central cavity may be a free base (H_2) or form complexes with up to 70 different metals. They also possess 16 separate sites for the attachment of a near limitless number of substituent groups, which may bond to the outer benzene rings at peripheral (β) or non-peripheral (α) positions, in addition to axial ligands which may be attached to inserted metals.

Even before their structural elucidation, phthalocyanines were noted for their impressive blue – green colours, their thermal stability and resistance to chemical reactivity under acidic and basic conditions. Originally applied in the dyeing, paper and textile industries as pigments for paints, coatings, ink,

fabric and plastics [125, 128, 129], the remarkable photochemical, photophysical and electronic properties of phthalocyanines have seen their applications expand into several other fields including data storage [130-132], catalysis [133-136], non-linear optics [137], dye sensitized solar cells [138], light emitting devices [139], chemical sensing [140-142] and photodynamic therapy [143, 144].

1.4.1 Phthalocyanine synthesis

The synthesis of phthalocyanines has been well reviewed by McKeown [145]. Phthalocyanines may be produced as demetalled (free base) or metallated products with symmetrically or unsymmetrically arranged substituents. Symmetrical Pcs are manufactured from several precursors (Scheme 1.2) including phthalamides, phthalic acids and anhydrides [146], phthalimides [147], 1-3-diiminoisoindolines [148], *o*-cyanobenzamides [147] and phthalonitriles [149] via cyclotetramerization reactions in the presence of a metal salt. Several of these precursors may occur as intermediates after the initial reactions of others.

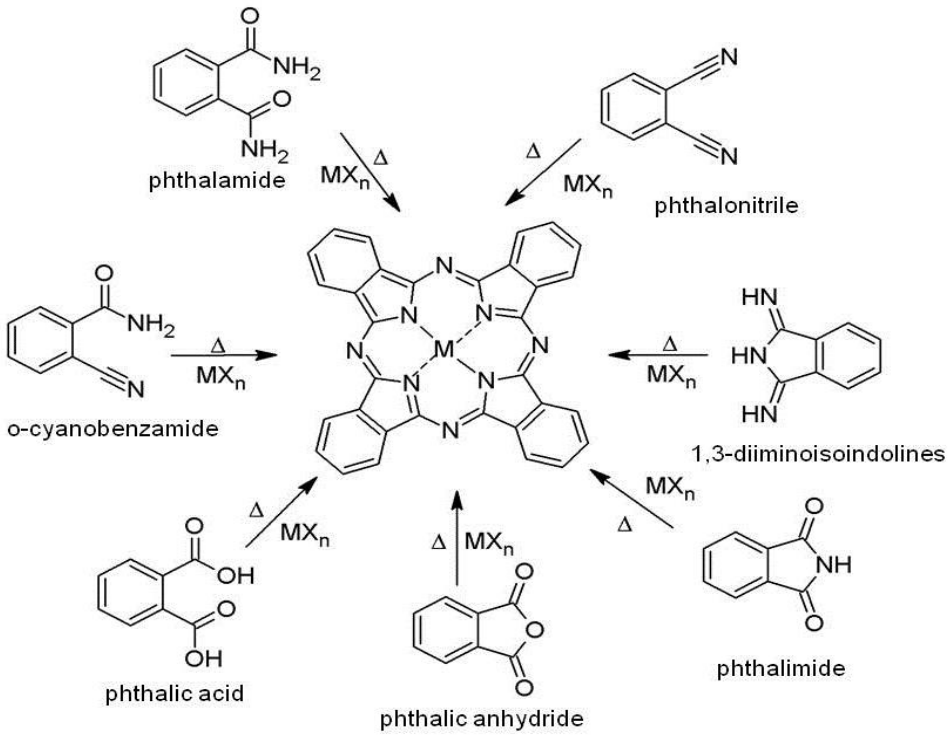

Scheme 1.2: Synthesis of phthalocyanines from several 1,2-disubstituted benzene species. Revised from [145].

Industrially, phthalimides, phthalic acids and phthalic anhydrides are more frequently used owing to their relatively cheap production costs when compared to expensive phthalonitriles which are more popular in small scale synthetic operations and in academic endeavours [145]. Amongst the common starting materials, phthalonitriles possess superior qualities as phthalocyanine precursors. They beget products of acceptably high purity and good yields via reasonably simple reactions [145]. Such reactions are accomplished utilizing several different approaches i.e. phthalonitriles may be added to metals or metal salts and heated to high temperatures as solid state mixtures or dissolved in a suitable high boiling point solvent [150, 151] such as quinolone, they may be combined with an appropriate reducing agent such as hydroquinone [152], or strong bases [152, 153] like 1,8-diazabicyclo[5,4,0]undec-7-ene (DBU), or a basic solvent, for example, N,N-dimethylaminoethanol (DMAE). The use of DBU in alcoholic solvents like pentanol facilitates the synthesis of Pcs using significantly lower reaction temperatures and results in high purity products [153]. Free base Pcs are synthesized using many of the same approaches mentioned above but without the addition of a metal or metal salt. They can also be generated through the cyclization of phthalonitriles with labile metals such as lithium and magnesium, which are easily removed using acid. The presence of labile metals also makes possible the inclusion of new metals in the macrocycle centre via a metal ion exchange. Some metallated Pcs are synthesized from already prepared free base Pcs where added metal ions begin to occupy the Pc centre upon heating. The synthetic procedures applied in the production of unsymmetrical phthalocyanines are beyond the scope of this work and have been well reviewed by Rodriguez-Morgade, de la Torre and Torres [154]. The cyclotetramerization of phthalic dianhydrides with urea as a nitrogen donor, and substituted phthalonitriles with labile metals in alcohol were the synthetic approaches utilized in this work.

1.4.2 Phthalocyanines used in this work

Two known phthalocyanines possessing different solubilities were employed based upon their ability to be mixed or linked to UCNPs in polar and non-polar solvents. An aluminium Pc derivative

possessing 8 peripheral carboxylic groups, as well as a free base Pc containing four thiophenoxy substituents were synthesized (Figure 1.5).

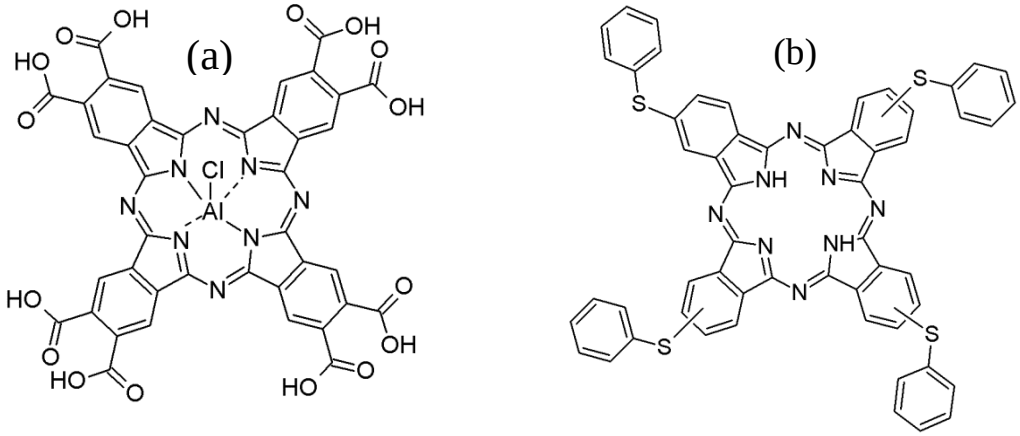

Figure 1.5: Structures of (a) aluminium and (b) free base Pc derivatives synthesized in this work.

The possession of carboxylic acid groups on the metallated Pc facilitates covalent linkage to surface functionalized nanoparticles with amine groups via formation of an amide bond. Octa carboxylic acid functionalized Pcs also possess a high affinity for aqueous media and, spectroscopically, display little evidence of aggregation in high pH aqueous solvents. A large body of research exists for octa carboxylic acid substituted Pcs with the spectroscopic, photophysical and photovoltaic properties of some species having been previously reported [155-157]. They have also been applied in the fabrication of dye conjugated nanomaterials and metal complexes with potential for application in medical diagnostics and cancer treatment [158, 159]. In contrast, tetra thiophenoxy substituted Pcs (H_2Pc) are readily soluble in non-polar solvents such as toluene and chloroform. The inclusion of bulky thiophenoxy groups has been shown to diminish aggregation [160] while the presence of a sulphur atom has been shown to facilitate conjugation to gold nanomaterials [161, 162].

1.4.3 Phthalocyanine absorption and fluorescence properties

1.4.3.1 Absorption spectra

The typical metallo phthalocyanine absorption spectra possesses two distinctive bands in the 300 – 400 nm and 600 – 720 nm regions termed the B, or Soret, and Q bands respectively [163, 164] (Figure 1.6).

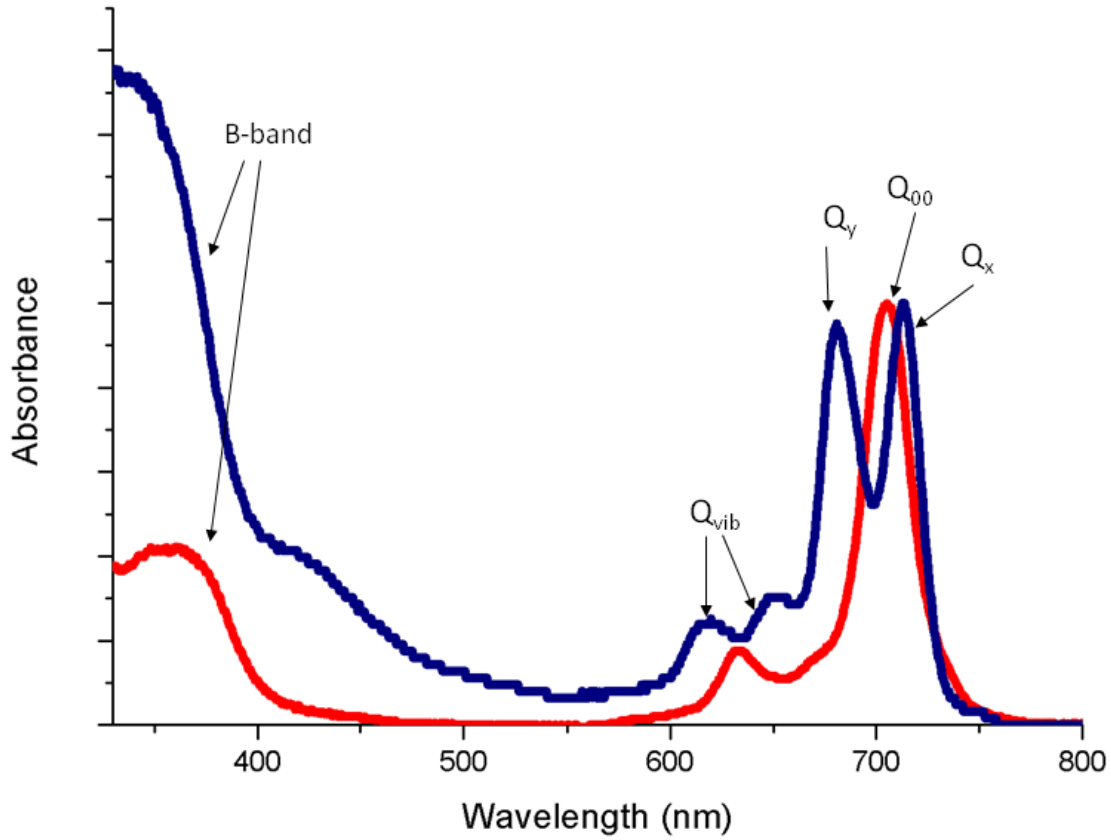

Figure 1.6: Typical absorbance spectra of a metallated (MPc, in red) and unmetallated (H_2Pc, in blue) phthalocyanine.

The provenance of these transitions is described by π to π^*transitions in Gouterman's four orbital model [165]. Therein, the Q band arises from a transition between the highest occupied molecular orbital (HOMO), a_{1u}, and the degenerate lowest unoccupied molecular orbitals (LUMO and LUMO+1), e_g (Figure 1.7). The weaker Q_{vib} bands are thought to arise from a transition involving

excited state vibrational levels (Figure 1.7). The broad B band comprises two bands, B_1 and B_2, which originate from a_{2u} to e_g and b_{2u} (HOMO-1) to e_g level transitions [163-165] (Figure 1.7). The degeneracy of the LUMO and LUMO+1 orbitals can be attributed to the D_{4h} symmetry of the planar, metallated Pc ring. Upon demetallation, two of the four central N atoms are protonated, lowering the symmetry from D_{4h} to D_{2h} [163]. Consequently, the LUMO and LUMO+1 degeneracy is lost, giving rise to two excited states and 2 Q bands (Q_x and Q_y). The shape and position of the Q band are influenced by several factors including Pc ring substituents, metal centres, axial ligands, solubility and solvent characteristics [166]. For example, Q band blue shifts are commonly recorded in polar solvents while red shifts are observed in non-polar media [167]. Extension of the ring's π conjugation can also lead to red shifting while the inclusion of some transition metals may result in large shifts as a result of charge transfer transitions [168].

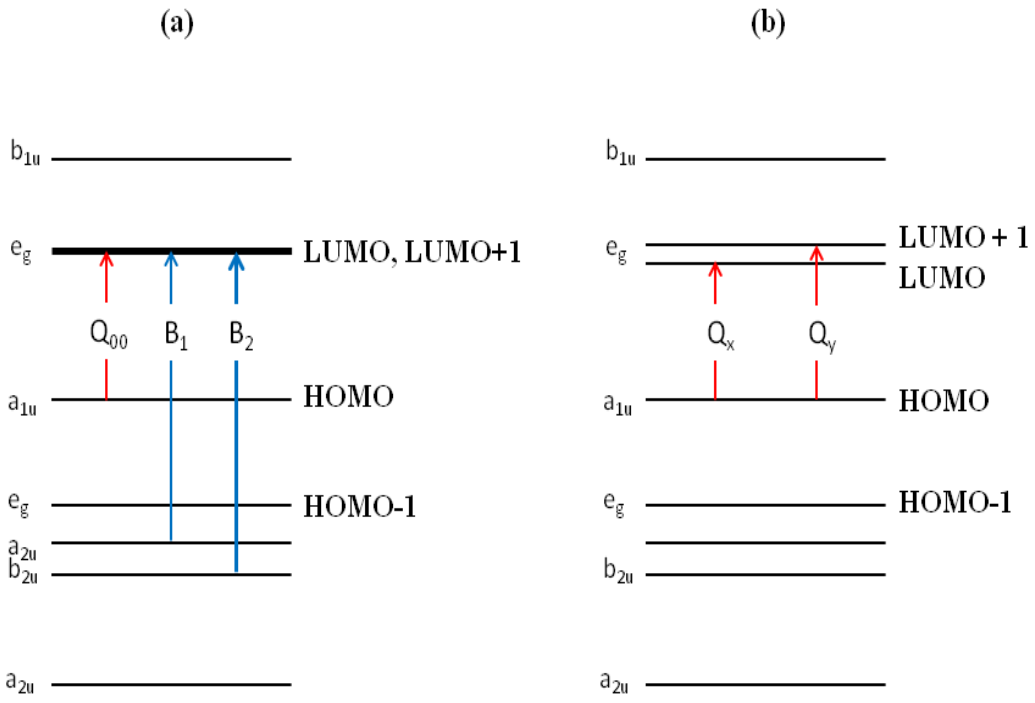

Figure 1.7: Electronic transitions in (a) metallated and (b) unmetallated Pcs, where HOMO = highest occupied molecular orbital and LUMO= lowest unoccupied molecular orbital. Revised from [164].

1.4.3.2 Fluorescence quantum yields and lifetimes

The relevant theory covering the origin of fluorescence spectra as well as that of the quantum yield and lifetime measurements applicable to phthalocyanine molecules has been covered in section 1.2. Naturally, emission peaks are red shifted compared to those in excitation and absorption spectra and normally occur in the 650-750 nm region for Q band excitation. Typical Pc fluorescence spectra adhere to the mirror image rule resulting in emission bands which are mirror images of the corresponding excitation spectra [169]. However, this is often not the case owing to the high propensity for Pcs to aggregate. Aggregation reduces the ability of Pc molecules to fluoresce (discussed in 1.4.5 below) and, therefore, where measurements are performed in solution, fluorescence intensity is highly dependent upon the nature of the solvent. Quantum yield measurements are largely performed using the comparative technique with photophysically well-known Pcs employed as reference compounds, depending on their relative solubility compared to the sample molecule [169]. In Pc molecules, emissions occur as a result of allowed transitions. This implies that the excited state lifetimes of Pcs are relatively short, typically, in the nanosecond region [169]. Again, aggregation has also been known to exert a shortening of fluorescence lifetimes possibly owing to the enhancement of non-radiative energy loss [169]. Quantum yields and lifetimes may also be influenced by the presence of 'heavy' atoms (i.e. those possessing relatively large atomic numbers) [169]. Such atoms enhance spin orbit coupling, leading to an increase in intersystem crossing to the triplet state and consequently shortening lifetimes and reducing quantum yields. Examples of fluorescence quantum yield and lifetime values, as well as absorbance and emission peak maxima, for 2 phthalocyanines which have been attached to UCNPs are shown in Table 1.1. The combining of Pcs with various nanoparticle systems has been undertaken by a large number of studies, many of which have reported changes in the spectroscopic and photophysical properties of Pcs conjugated to or mixed with nanoparticles [170-172]. However, the investigation of changes to Pc spectroscopic and photophysical properties when combined or mixed with upconversion nanoparticles has not been reported. In this work, the spectroscopic and fluorescence properties of Pcs mixed with and conjugated to UCNPs are reported for the first time.

Table 1.1: Spectroscopic and photophysical properties of selected phthalocyanines studied in conjunction with UCNPs.

Phthalocyanine	Q_{abs} (nm)	Q_{em} (nm)	Φ_F	τ_F (ns)	Solvent	Ref.
Zinc phthalocyanine (ZnPc)	669	682	0.32	4.73	DMSO	[173]
Aluminium tetracarboxy phthalocyanine (AlTCPc)	690	698	0.33	2.90	DMSO	[174]

1.4.4 Phthalocyanine aggregation

Phthalocyanine aggregation arises as a result of non-bonding interactions between molecules in close proximity to one another. Such intermolecular forces facilitate intermolecular attraction resulting in the co-planar 'stacking' of two (dimers), three (trimers) or more molecules during the formation of molecular aggregates [175]. The aromaticity and planarity of the phthalocyanine macrocycle contribute to the close approach and attractive interactions between molecules. Such interactions are also inherently dependent on factors influencing solubility [175]. These factors include solvent polarity, temperature, pH and concentration [175]. The formation of molecular aggregates may effectuate alterations in chemical and physical properties in relation to those possessed by the monomeric species. These alterations may manifest themselves in changes which are observable utilizing spectroscopic techniques and include, in the case of Pcs, phenomena such as Q band red shifts, blue shifts, splitting or broadening [175]. The provenance of spectroscopic changes, for Pc dimers, lies in the splitting of excited state energy levels as a result of the relative orientation of the molecular dipole moments and is described by the exciton coupling theory proposed by Kasha (Figure 1.8) [176, 177]. In cases where molecular association occurs linearly, co-facial (H aggregate) or end to end (J aggregate) arrangements may result [175, 177]. For both arrangements, the excited state is split into 2 levels, one with transition dipole moments in phase (parallel) and the other vice versa (anti parallel) [177]. Transitions between the ground state and excited states where transition moments are parallel are quantum mechanically allowed while those between the ground state and anti-parallel excited states are forbidden. In H aggregates, absorption occurs, with the highest probability, between

the ground and highest excited states resulting in a blue shifted absorbance peak when compared to the monomer. For J aggregates, in contrast, absorption is more likely to result in electronic occupation of the lower excited state, which possesses parallel transition moments, resulting in an absorbance peak red shift. Additionally, since de-excitation from the lowest excited level is allowed in J aggregates, such species are known to be highly fluorescent [175]. Experimentally, the observation of J aggregates is particularly rare. In the majority of cases, aggregation is an unwanted phenomenon owing to the spectroscopic and photo-physical deviations of the aggregated system from that of the monomer. The inclusion of bulky substituents attached to the Pc macrocycle [178], particularly in the α-position [160], or axially to the central metal, has been shown to be effective in decreasing aggregation. A decrease in aggregation may also be observed in solution upon the addition of surfactants.

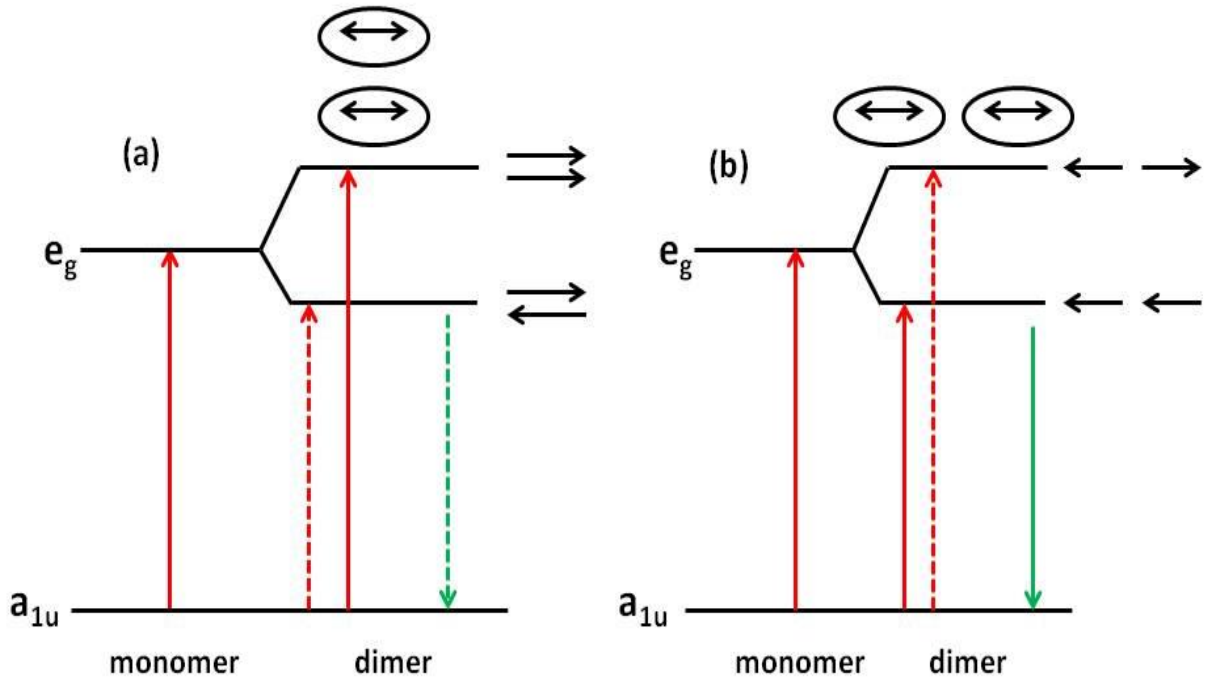

Figure 1.8: Excited state splitting for (a) H aggregates and (b) J aggregates where encircled arrows represent molecules, black arrows represent transition dipole moments and solid and dotted arrows represent allowed and forbidden transitions respectively. Red arrows refer to absorption and green arrows refer to fluorescence. Revised from [175, 177].

1.4.5 Singlet oxygen generation and photodynamic therapy

The term singlet oxygen refers to molecular oxygen which has been promoted to its metastable singlet excited state and is classified as a reactive oxygen species (ROS) [179]. The metastability of the lowest singlet excited state is a result of relaxation to the triplet ground state being spin forbidden. This imparts a relatively long lifetime to molecular singlet oxygen, allowing it to participate in a great number of chemical reactions. In comparison to molecules occupying the ground (triplet) state, singlet oxygen is highly electrophilic and has found use as an oxidizing agent for numerous organic reagents including some sulfides, phosphides, amines, alkenes and a number of cyclic compounds [180]. Evidently, chemical moieties such as these are ubiquitous in biological systems and,consequently, highly reactive singlet oxygen has been shown to be cytotoxic [181].

Singlet oxygen may be generated by means of several processes including photosensitization. In the latter process, a photosensitizing agent occupying its triplet state (having done so as a result of excitation to its first excited state followed by intersystem crossing) relaxes to the ground state, transferring this energy to a molecule of oxygen (Figure 1.9) [179]. Good photosensitizers typically possess a long lived triplet state whose potential energy exceeds the 94 kJ/ mol required to excite ground state molecular oxygen. They include a wide variety of synthetic and naturally occurring compounds, one class of which is the phthalocyanine [179]. The processes of photosensitization may be accomplished via two mechanisms, type I and type II (Scheme 1.3) [179, 182]. The type II mechanism, which has been explained above, effectuates the production of singlet oxygen through energy transfer from the excited photosensitizer (Figure 1.9). Type I involves the reduction (or oxidation) of the photosensitizer by another chemical species present in the system through electron transfer. The oxidised and/ or reduced substrate and photosensitizer molecules may then react with other substrates or ground state molecular oxygen to produce oxygen radicals like the superoxide anion (Scheme 1.3) [179, 182].

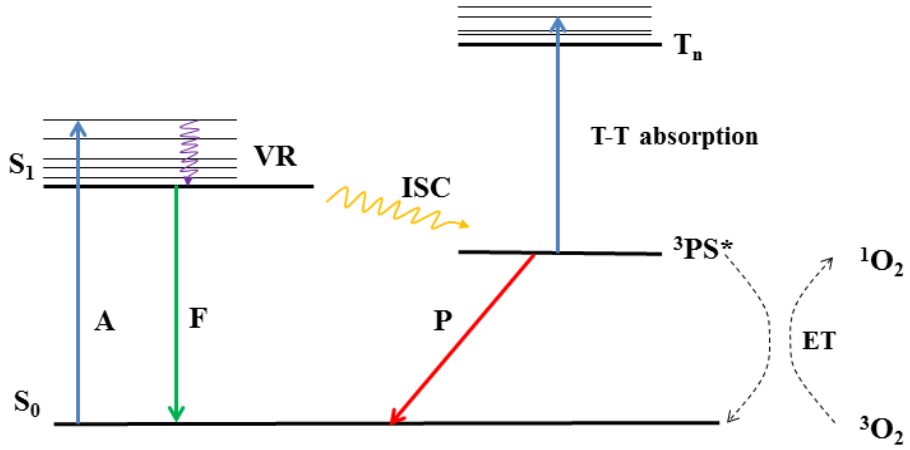

Figure 1.9: Simplified Jablonski diagram highlighting the energy transfer between a photosensitizer, occupying an excited triplet state, and ground triplet state molecular oxygen. $^3PS^*$ = photosensitizer in the first triplet excited state. Other symbols are defined in Figure 1.1.

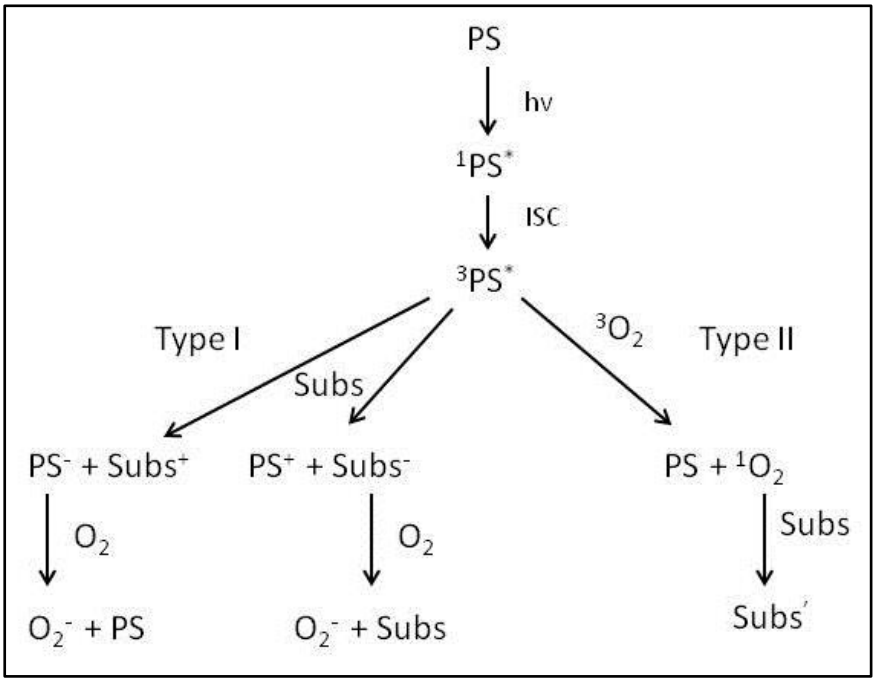

Scheme 1.3: Type I and II mechanisms of photosensitization where ISC = intersystem crossing, PS = photosensitizer and Subs = substrate. Revised from [182].

The singlet oxygen generation efficacy of a photosensitizer is given in the form of the singlet oxygen quantum yield, designated Φ_{Δ}. As in the case of fluorescence quantum yield measurements, experiments undertaken for singlet oxygen quantum yield determination are usually done utilizing a

standard. Experimentally, the photodegradation rate of a singlet oxygen trap such as diphenylisobenzofuran (DPBF) or anthracene-9,10-diyl-bis-methylmalonate (ADMA) is examined by exciting a mixture of a photosensitizer and chemical trap for a series of specific time intervals [183]. This is then compared to the photodegradation rate induced by the standard and a quantum yield is subsequently calculated using Equation 1.3:

$$\Phi_{\Delta} = \Phi_{\Delta}^{\mathrm{Std}} \cdot \frac{\mathrm{RI}_{\mathrm{abs}}^{\mathrm{Std}}}{\mathrm{R}^{\mathrm{Std}}\mathrm{I}_{\mathrm{abs}}} \qquad (1.3)$$

where $\Phi_{\Delta}^{\mathrm{Std}}$ is the singlet oxygen quantum yield of the standard, $\mathrm{I}_{\mathrm{abs}}$ and $\mathrm{I}_{\mathrm{abs}}^{\mathrm{Std}}$ are the rates of light absorbance by the photosensitizer and standard respectively and R and $\mathrm{R}^{\mathrm{Std}}$ are the photodegradation rates of the trap in the presence of the photosensitizer and standard respectively [183]. Other singlet oxygen detection methods involve the examination of singlet oxygen luminescence spectra which typically display a broad peak at 1270 nm upon relaxation to the ground state [183]. This approach may also be used to calculate quantum yields by comparing the integrated area under the singlet oxygen luminescence curves produced by the photosensitizer and a standard. Lifetime measurements may also be used to establish the presence of singlet oxygen as well as to probe environmental effects on the excited state stability [184, 185]. Owing to the fact that no standard exists for upconversion mediated singlet oxygen generation (i.e. at 980 nm), in this work detection was accomplished utilising fluorescence emissions and lifetimes.

The ability of photosensitizers to produce cytotoxic ROS has been exploited, to a great extent, in the medicinal field of photodynamic therapy (PDT), where photosensitizers are introduced into living tissue and produce ROS upon exposure to light [186]. PDT has successfully been implemented in the treatment of several diseases, in particular, some types of cancer [187-194]. In the case of the latter, it has been lauded as a less invasive treatment with significantly fewer side effects in comparison to more conventional chemotherapeutic approaches which necessitate the usage of harsh, non-selective drugs, for example, those containing derivatives of the active ingredient cis-platin [195]. The reduction in side effect occurrence during PDT is attributable to the confinement of photodynamic

action to areas which are selectively irradiated in conjunction with the fact that singlet oxygen molecules possess a relatively small activity radius of around 20 nm [186, 196]. The destruction of tumour cells and tissue eventuates as a result of three processes i.e. intracellular damage from ROS, immune system action initiated by the presence of the photosensitizer/ ROS and damage to the blood vessels supplying diseased tissue [186]. Clinically applicable photosensitizers should possess several key characteristics. Naturally, they should have large singlet oxygen quantum yields, long lived triplet states, good solubility, low dark toxicity and relatively high photostability [197, 198]. They should also absorb strongly in the red to near infrared window (600 – 1000 nm) as wavelengths below or above this region are prevented from penetrating deeply into tissue as a result of absorption by various biomolecules and water respectively [197]. Ideally, photosensitizers, like all chemotherapeutic agents, should also possess a high selectivity towards absorption by tumour cells and tissue. Phthalocyanines, characterized by their good absorption in the red to far red region, as well as their reasonable singlet oxygen quantum yields, have proven to be good candidates for PDT, with several examples currently in clinical trials [199, 200] .

As with all cancer treatments, however, PDT possesses a number of limitations. Many of these revolve around the need for visible light excitation. The ensuing localization of treatment to specific tissue areas or organs is therefore only truly effective in treating cancer in the early stages, i.e. before the onset of metastasis. It also limits applications to deep tissues or large tumours as even red light cannot penetrate more than a few centimetres at the very most. This dilemma has initiated the search for photosensitizers whose strongest absorption occurs in the NIR region, where wavelengths are better able to deeply penetrate tissue. Another solution currently being explored is the usage of photosensitizers in conjunction with NIR absorbing upconversion nanoparticles. Nanoparticles have also been shown to act as effectual drug carriers, increasing the uptake of photosensitizer molecules by tumour cells and tissue in relation to healthy cells.

1.4.6 Phthalocyanines and upconversion nanoparticles

In their capacity to act as probes for *in vivo* fluorescence imaging and sensing, UCNPs may be combined with a variety of other molecules in order to create highly fluorescent, multi-functional nanoprobes and drug carriers. One area, which has stimulated some research interest in the last seven to eight years, is the application of UCNPs to photosensitizers. Here, the nanoparticles are utilized as 'NIR photon harvesters', allowing for the production of cytotoxic singlet oxygen molecules using longer wavelengths through a resonant energy transfer to an attached photosensitizer (Figure 1.10).

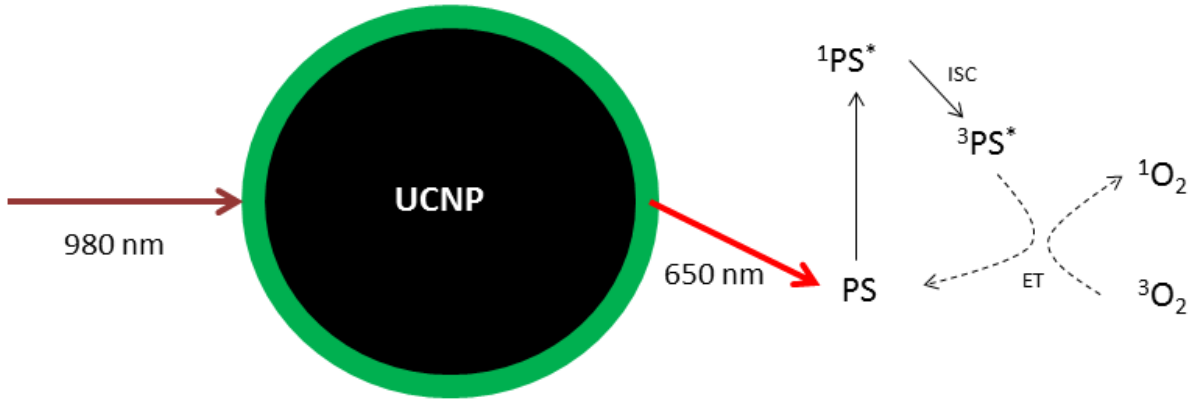

Figure 1.10: Diagram showing UCNP mediated singlet oxygen generation.

The attachment of photosensitizers to UCNPs has been facilitated utilizing both covalent and non-covalent approaches and usually requires modification of the nanoparticle surface. Polyethylenimine, N-succinyl-N'-octyl chitosan and mesoporous silica are commonly used to alter nanoparticle surfaces. A wide variety of photosensitizer molecules have been employed in conjunction with UCNPs including: a runthenium (II) complex [201], rose Bengal [202], tetraphenyl porphyrin [203, 204], merocyanine 540 [205, 206], chlorin e6 [207-209], hematoporphyrin [123], pyropheophorbide [210], methylene blue [211] as well as three different phthalocyanines (Figure 1.11). The three phthalocyanines which have been utilized in studies so far are: aluminium tetra carboxy phthalocyanine (AlTCPc), axially substituted dihydroxy silicon phthalocyanine ($(OH)_2$SiPc) and

unsubstituted zinc phthalocyanine (ZnPc), with ZnPc being the most studied (Figure 1.11). To the best of our knowledge, all studies, published in English, in which phthalocyanines have been attached to UCNPs are listed in Table 1.2. $NaYF_4$:Yb/Er (rarely Tm^{3+}) and/ or $NaGdF_4$:Yb/Er nanoparticles have been utilized in all studies concerning phthalocyanine – UCNP combinations, without exception. In some instances the $NaYGdF_4$ unit is incorporated into a core shell structure with other inorganic crystal species. Still other studies have utilized additional dopants (i.e. manganese). These studies have also been reviewed in more detail elsewhere [212]. For the purposes of this work, covalent conjugation, as well as simple mixing, approaches were utilized in order to observe any spectroscopic changes resulting from the addition of UCNPs to phthalocyanines. Conjugation was facilitated by the addition of an APTES functionalized silica shell to the nanoparticle surface (Figure 1.12). Here we attempt to examine any possible changes in Pc absorbance, fluorescence lifetime and fluorescence quantum yield values arising from the combination of 2 Pcs (AlOCPc and H_2Pc) with different solubility properties to Tm^{3+} and Er^{3+} activated $NaYGdF_4$ upconversion nanoparticles. Covalent grafting to UCNPs using a tetracarboxy AlPc derivative has been undertaken elsewhere [213]. The octacarboxy AlPc and H_2Pc molecules used in this work have not been studied in conjunction with UCNPs before.

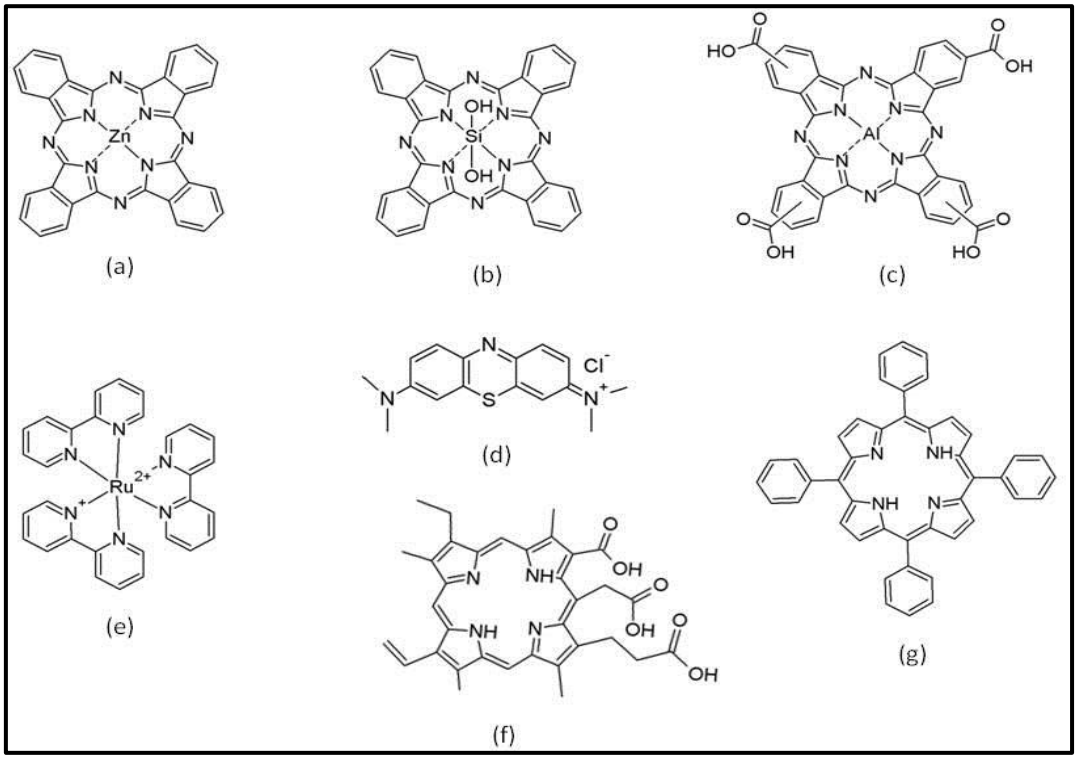

Figure 1.11: Structures of selected photosensitizers combined with UCNPs: (a) zinc phthalocyanine, (b) dihydroxy silicon phthalocyanine, (c) aluminium tetracarboxy phthalocyanine, (d) methylene blue, (e) tris(bipyridine) ruthenium (II), (f) Chlorin e6 and (g) tetraphenyl porphyrin.

Table 1.2: List of phthalocyanines attached to different UCNPs as well as nanoparticle surface modification and the methods used to attach the Pc to the modified surface. Where PEI = polyethylenimine, SOC = N-succinyl-N'-octyl chitosan, PEG = polyethylene glycol and APTES = 3-aminopropyltriethoxysilane.

Phthalocyanine	**Nanoparticle**	**Surface modification**	**Attachment method**	**Reference**
ZnPc	$NaYF_4$:Yb/Er	PEI	physical adsorption	[214]
ZnPc	$NaYF_4$:Yb/Er	mesoporous silica	silica encapsulation	[215]
ZnPc	$NaYF_4$:Yb/Er	mesoporous silica	silica encapsulation	[216]
ZnPc	$NaYF_4$:Yb/Er	SOC	SOC encapsulation	[217]
AlTCPc	$NaGdF_4$:Yb/Er@$NaGdF_4$	silica	covalent grafting to silica using APTES linker	[213]
ZnPc	$NaYF_4$:Yb/Er	PEI	physical adsorption	[218]
ZnPc	$NaYF_4$:Yb/Er/Mn	α- cyclodextrin	physical adsorption	[208]
ZnPc	$NaYF_4$:Yb/Er	mesoporous silica	silica encapsulation	[205]
ZnPc	$NaYF_4$:Yb/Er	SOC	SOC encapsulation	[219]
ZnPc	$NaYF_4$:Yb/Er/Tm	poly(allylamine)	Pc and NP adsorbed onto PEGylated graphene sheet	[220]
$(OH)_2SiPc$	$NaGdF_4$:Yb/Er@CaF_2	mesoporous silica	covalent grafting to silica using APTES linker	[123]

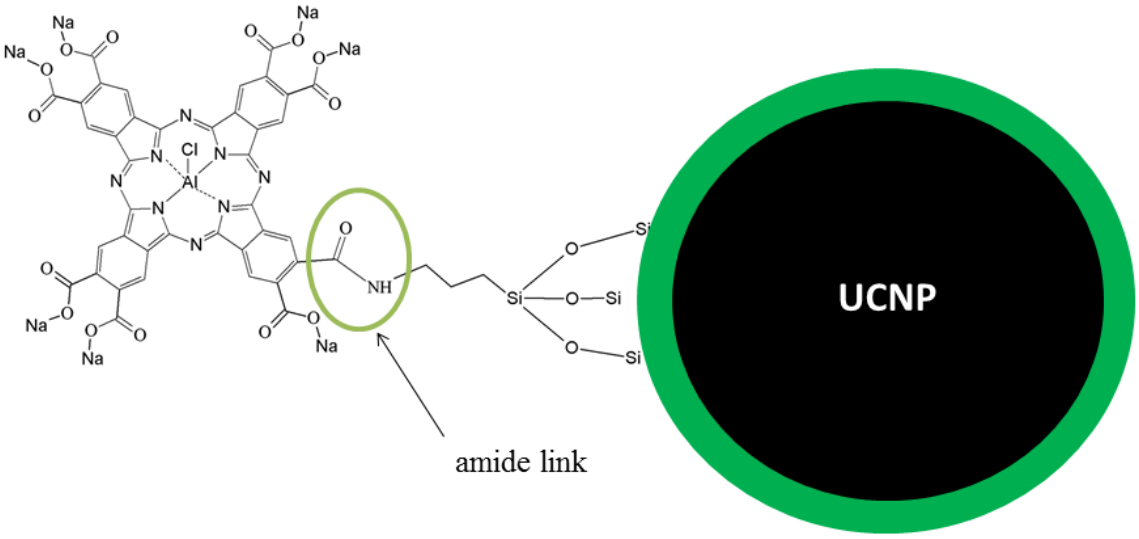

Figure 1.12: AlOCPc-UCNP@Si conjugate showing the amide link.

1.5 Summary of aims

The aims of this thesis may be summarised as follows:

1. The synthesis and characterization of spherical and star shaped, Gd^{3+} doped $NaYGdF_4$:Yb/Er (Tm) UCNPs. The synthesis and characterization of silica coated, spherical $NaYGdF_4$:Yb/ Er upconversion nanoparticles.

2. Investigation of the UV-visible absorption and fluorescence properties of a tetrathiophenoxy H_2Pc mixed with UCNPs in toluene and an octacarboxy AlPc covalently linked to UCNPs in DMSO.

Chapter 2

Experimental

2.1 Materials

For synthesis and characterization: yttrium nitrate hexahydrate, gadolium chloride anhydrous, ytterbium chloride hexahydrate, erbium chloride hexahydrate, thulium chloride anhydrous, ammonium fluoride (NH_4F), 1-octadecene, oleic acid, Igepal CO-520, tetraethoxysilane (TEOS), 3aminopropyltriethoxysilane (APTES), N-(3-dimethylaminopropyl)-N-ethylcarbodiimide (EDC), N-hydroxysuccinimide (NHS), benzene-1,2,4,5-tetracarboxylic dianhydride (pyromellitic dianhydride), urea, lithium, 1,8-diazabicyclo[5.4.0]undec-7-ene (DBU) and aluminium chloride were purchased from Sigma-Aldrich. NaOH pellets were purchased from SAARChem. Neutral alumina, for column chromatography, was purchased from Merck.

For spectroscopic and fluorescence experiments: unsubstituted zinc phthalocyanine, sodium azide and 2,2-diphenyl-1-picrylhydrazyl (DPPH) were purchased from Sigma-Aldrich.

Solvents: Ethanol, methanol, pentanol, cyclohexane, acetone, dimethyl formamide (DMF), sulphuric acid, hydrochloric acid and toluene were purchased from SAARChem. Uvasol®, dimethyl sulfoxide (DMSO) and toluene were purchased from Merck.

2.2 Equipment and Instrumental Setups

1. Transmission electron microscope (TEM) images were obtained using a Zeis Libra at 120 kV accelerating voltage.

2. Energy dispersion x-ray spectroscopy (EDX) was performed utilizing a TESCAN Vega TS 5136LM scanning electron microscope equipped with an INCA PENTA FET (EDX) from Oxford Instruments.

3. X-ray diffraction was undertaken using a Bruker D8 discover equipped with a LynxEye detector and Cu-Kα radiation source (1.5403 Å, nickel filter). Samples were analysed upon a silicon wafer slide and diffraction data were collected at 2θ values between 10^{o} – 100^{o} using a locked coupled scan of 9381 steps of 0.00959^{o} at a rate of 0.4 s per step and a slit width of 6 mm. Data were analysed using evaluation curve fitting software, EVA (Bruker), and Rietveld refinements were performed using Topas version 4.2 software (Bruker).

4. Fourier transform infrared spectroscopy (FT-IR) was performed using a Perkin Elmer Spectrum 100 ATR FT-IR spectrometer.

5. A Shimadzu UV-2550 spectrophotometer was used to record UV-visible spectra. Samples were analysed in solution utilizing a quartz cuvette with a path length of 1 cm.

6. Fluorescence spectra were recorded on a Varian Eclipse spectrofluorimeter. Samples were analysed in solution utilizing a quartz cuvette with a path length of 1 cm.

7. Matrix assisted laser desorption ionisation (MALDI) mass spectra were recorded utilizing a Bruker AutoFlex III Smartbeam TOF/TOF mass spectrometer. Aluminium octacarboxy phthalocyanine spectra were performed in negative ion mode while those for the unsubstituted tetra thiophenoxy phthalocyanine were obtained using positive ion mode. In both cases, spectra were recorded over a mass to charge ratio of 400 to 3000 amu. All spectra were obtained utilizing an α-cyano-4-hydroxycinnamic acid matrix. Internal calibration was done using a polyethylene glycol standard.

8. Electron paramagnetic resonance (EPR) spectra were obtained utilizing a Bruker X-band EMX series EPR spectrometer equipped with an ER 4119HS-LC resonator at a microwave frequency of 9.84 GHz. Data were obtained using a 6698.208 G sweep width with a centre at 3299.104 G. The modulation frequency and amplitude were set at 100 kHz and 20.00 G respectively. The receiver gain was set at 1.00×10^4 and signals were averaged over 10 scans.

9. Thermogravimetric analysis was performed using a Shimadzu DTG-60A simultaneous differential thermal analysis – thermogravimetric analysis system. Data were collected from 50^oC to 500^oC in an aluminium pan with a nitrogen flow rate of 120 $cm^3 . min^{-1}$.

10. Phthalocyanine (and UCNP down-conversion) lifetime measurements were undertaken using the Fluotime 200 time correlated single photon counting setup (Picoquant, GmbH) with a PDL 800-B 672 nm diode laser (Picoquant, GmbH) with a 20 MHz repetition rate and 44 ps pulse width. Emissions were detected under the magic angle, using a PMA-C-192-N-M photomultiplier tube (Picoquant, GmbH) and a PicoHarp TCSPC card (Picoquant, GmbH). Emission wavelengths were selectively detected using a monochromator spectral width of 8 nm. Instrument response functions were obtained using Ludox (DuPont). All sample lifetimes were recorded at their maximum emission peaks. Lifetimes were calculated using a deconvolution fitting model and errors were determined by support plane error analysis.

11. Upconversion and singlet oxygen steady state and lifetime measurements were recorded using a Fluotime 300 time correlated single photon counting setup (Picoquant, GmbH) (Figure 2.1). Upconversion emissions were induced using 972 nm excitation from a LDH-D-C-980 diode laser (Picoquant, GmbH). Steady state emission was obtained under continuous wave excitation while time resolved measurements were performed using a an 80 MHz repetition frequency with a maximum pulse width of 500 ps. Emissions were detected under the magic angle utilizing a PMA-C 192-M photomultiplier tube (Picoquant, GmbH). Singlet oxygen steady state and lifetime measurements were undertaken using 672 nm excitation from a PDL 800-B diode laser at an 80 MHz repetition rate. Detection was performed under the magic

angle using an H10330A-45 NIR photomultiplier tube (Hamamatsu). Photon counting was done using an integrated TimeHarp 260-N TCSPC card (Picoquant, GmbH). Emission wavelengths were selectively detected using an Omni-λ300 grating monochromator at 1200 lines/ mm with a spectral width of 4 mm.

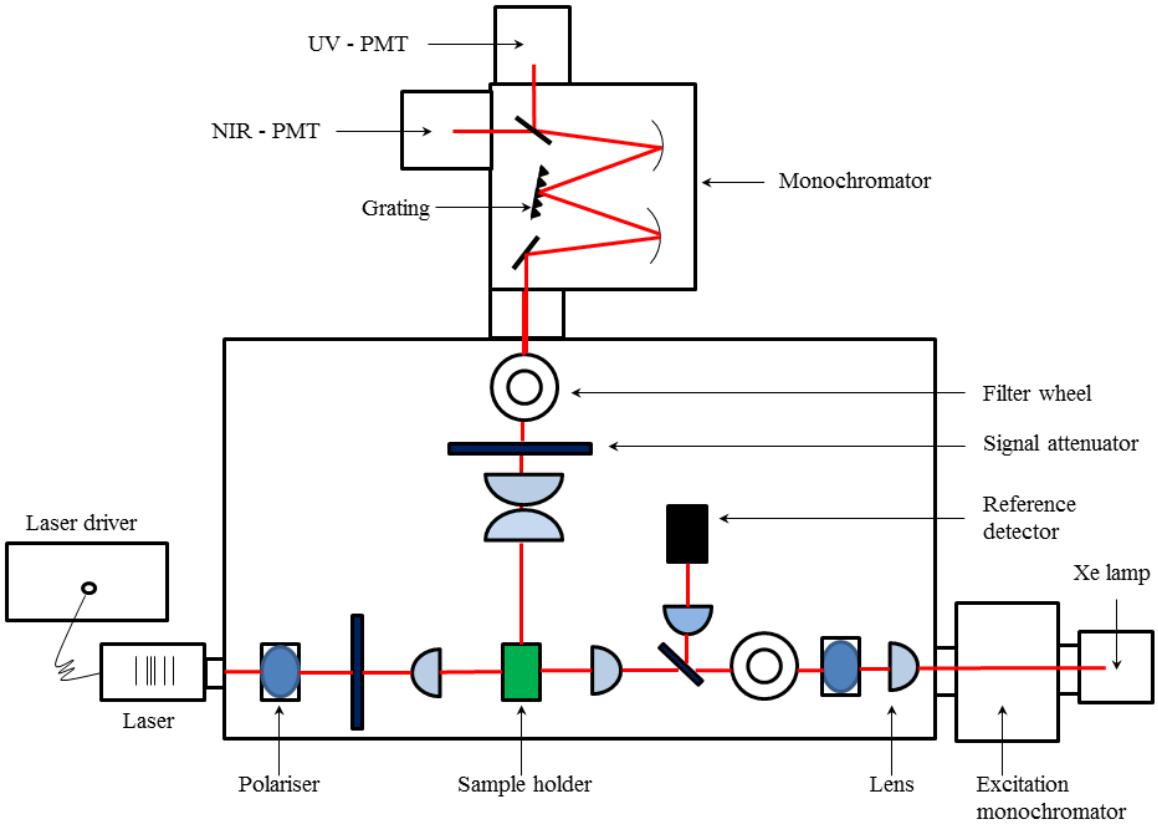

Figure 2.1: Diagram showing the layout of the Fluotime 300 and its internal components.

2.3 Methods and synthesis

2.3.1 Fluorescence quantum yields

Fluorescence quantum yields were calculated using Equation 1.1. Unsubstituted ZnPc was used as a standard in both DMSO and toluene where it possessed Φ_F values of 0.2 and 0.07 respectively [221]. The standard and sample absorbencies at the vibronic band were kept the same and excitation was

done using the wavelength of the cross over point between the vibronic bands of the sample and standard absorbance spectra.

2.3.2 Fluorescence quenching of UCNP downconversion emission using DPPH radical.

Quenching of UCNP downconversion emissions was undertaken by incrementally adding drops of DPPH solution to a concentrated solution of $NaYF_4$:Yb/ Ho UCNPs in cyclohexane and the emission spectrum was recorded after each increment. A DPPH solution was obtained by dissolving a few milligrams of DPPH powder in 2-3 ml of cyclohexane.

2.3.3 $NaYGdF_4$:Yb/ Er (Tm) upconversion nanoparticles (UCNP)

Upconversion nanoparticles were synthesized using a methanol assisted thermal decomposition approach [85]. $LnCl_3$ precursors (0.8 mmol) were dissolved in 4 ml of methanol and added to a 100 ml flask containing 6 ml of oleic acid and 14 ml of 1-octadecene. The solution was heated to 160^{o}C for 30 minutes after which it was allowed to cool to room temperature. NH_4F (3.2 mmol) and NaOH (2 mmol) in 10 ml of methanol were then added. The solution was stirred for 30 minutes after which it was heated to 70^{o}C until all the methanol had evaporated. The solution was heated to 300^{o}C (315^{o}C) under argon for 1.5 hours. The UCNPs were precipitated using ethanol and collected by centrifugation. They were then washed with methanol and ethanol several times. The relative amounts of Ln ions used differed for several products. Erbium (0.016 mmols), ytterbium (0.14 mmols when used with erbium and 0.16 mmols when used with thulium) and thulium (1.6 μmol) molar concentrations were maintained for all syntheses; however, gadolinium (0.04 mmol – 0.24 mmol) and yttrium (0.6 mmols – 0.4 mmol) concentrations were purposely varied. Yield: 70–90 mg.

2.3.4 $NaYGdF_4$:Yb/Er silica coated upconversion nanoparticles (UCNP@Si)

Synthesis of silica coated UCNPs was undertaken using a modified literature method [222]. Oleic acid stabilized UCNPs (79 mg) (synthesized in 2.3.1) were dispersed in 67.5 ml of cyclohexane. Igepal CO-520 surfactant (1.125 ml, 2.5 mmol) was added and the solution was stirred for 10 minutes. While stirring, 25% ammonia (0.9 ml, 12.06 mmol) and additional Igepal CO-520 (4.5 ml, 10.2 mmol) were added. The solution was then agitated using sonication for 1.5 hours after which it was stirred for 10 minutes. Lastly, TEOS (0.45 ml, 2.02 mmol) was added and the solution was left to stir for four days. Yield: 30–35 mg.

2.3.5 $NaYGdF_4$:Yb/Er silica coated, amino functionalized upconversion nanoparticles (UCNP@Si@APTES)

APTES functionalization of UCNPs was performed using a modified method found in literature [223]. UCNP@Si (30 mg) were washed several times with dry ethanol and toluene, dried, and added to a mixture of DMF (36 ml) and toluene (24 ml). APTES (1 ml) was added dropwise under argon and the solution was left to stir for 24 hours. The functionalized particles were collected by centrifugation and washed several times with toluene. Yield: 25-28 mg.

2.3.6 $NaYGdF_4$:Yb/Er@si@APTES-(Cl)AlOCPc conjugate (UCNP@Si@APTES - (Cl)AlOCPc)

(Cl)AlOCPc (15 mg, 0.014 mmol) was added to PBS buffer solution pH 7.4 (15 ml). EDC (0.35 g, 1.8 mmols) and NHS (0.172 g, 1.5 mmol) were added to activate the carboxylic groups of the Pc. The reaction mixture was left to stir for 3 hours under argon. UCNP@Si@APTES (5 mg) were suspended in PBS buffer solution pH 7.4 (15 ml) and added to the Pc solution. The mixture was allowed to stir for 15 hours under argon. The obtained product was precipitated by adding ethanol and collected by

centrifugation. The conjugate particles were washed once with NaOH, to remove unconjugated Pc. Yield: 3.5-4.5 mg.

2.3.7 Chlorinated aluminium octacarboxy and unsubstituted tetrathiophenoxy phthalocyanines ((Cl)AlOCPc and H_2Pc respectively).

The unmetallated tetrathiophenoxy phthalocyanine (H_2Pc) was synthesized and purified according to methods found in the literature [224]. Characterization was performed using FT-IR, mass spectrometry and UV-vis spectroscopy. FT-IR (cm^{-1}): 3388 (N-H υ), 3284 (carboxylic O-H υ), 1704 (carboxylic C=O υ), 1629 (aromatic C=C υ), 1031 (C-H δ), 1336 (aromatic N-C υ), 1278 (carboxylic C-O υ), 1203 (carboxylic C-O υ). UV-vis (toluene) Q band λ_{max}: 681 nm, 713 nm. MALDI-TOF MS: calculated for $C_{56}H_{34}N_8S_4$ 947.18 amu, found 950 amu [M+3H].

Chloro axially ligated aluminium octa carboxy phthalocyanine ((Cl)AlOCPc) was synthesized according to literature methods [225]. Purification was done using column chromatography on several neutral alumina columns (8 cm long by 2.6 cm wide) with 3 % NaOH as the eluent at a flow rate of 0.2 ml per second. Resulting product was found to be the sodium salt of (Cl)AlOCPc. 3388 (N-H υ), 3284 (carboxylic O-H υ), 1704 (carboxylic C=O υ), 1629 (aromatic C=C υ), 1031 (C-H δ), 1336 (aromatic N-C υ), 1278 (carboxylic C-O υ), 1203 (carboxylic C-O υ). UV-vis (DMSO) Q band λ_{max}: 705 nm. MALDI-TOF MS: calculated for $C_{40}H_8N_8AlClNa_8O_{16}$ 1102.9 amu, found 1067.1 amu [M-Cl].

Chapter 3

Synthesis and characterization of upconversion nanoparticles

3.1 Synthesis of upconversion nanoparticles

All UCNPs were synthesized utilizing a methanol assisted thermal decomposition approach in the presence of an oleic acid stabilizer [85]. The use of rare earth chloride and nitrate salts, NaOH and NH_4F precursors in place of more commonly used rare earth and sodium trifluoroacetates was undertaken owing to their relatively cheaper costs, lower air sensitivity and, in particular, their lower toxicity. All reaction stages, with the exception of the final heating step, at 300^oC, were performed under atmospheric conditions and this did not appear to influence the yields or consistency of the nanoparticles. The type of lanthanide precursor used, however, resulted in notable changes. Initially, all of the lanthanide precursors utilized were hydrated chlorides with the exception of the yttrium salt, where only the hydrated nitrate was available from the suppliers. The resulting nanoparticles were very dark brown in colour and were produced in fairly good yields. Later attempts to replace the yttrium nitrate with a chloride consistently resulted in lighter coloured particles with substantially lower yields under identical reaction conditions. As a result, all synthetic attempts were conducted utilizing the yttrium nitrate precursor. Although, to our knowledge, the merits of using nitrates over chlorides or vice versa have never been examined, we speculate that the presence of the nitrate precursor, in particular yttrium nitrate as yttrium constitutes the bulk of the rare earth atoms accommodated in the nanocrystals, may, possibly, result in higher yields since these species are generally more soluble than the chlorides. The involvement of the nitrate ion, or the rare earth nitrates themselves, in some sort of oxidation reaction with the alkene groups of the stabilizer or solvent [226, 227] is also possible and may give rise to the observed colour change.

The use of Gd^{3+} doping was employed in order to control nanoparticle size and shape as well as to impart additional functionality through gadolinium's interesting paramagnetic properties [85]. Gd^{3+} ions were doped in at 5, 15, 25 and 30 mol % for $NaYF_4$:Yb nanoparticles containing either Tm^{3+} or Er^{3+} activators, though one attempt utilized a Ho^{3+} activator. The inclusion of different activator ions is not thought to induce any morphological changes in the particles owing to their low dopant concentrations and similar ionic radii. Doping of Gd^{3+} ions did not exceed a maximum of 30 mol % owing to the detrimental effects of doping at higher concentrations on fluorescence having been

recorded elsewhere [85]. Gd^{3+} doping did not, however, appear to influence nanoparticle size and shape to the same extent as reaction temperature and the rate of reaction heating. The control of the maximum temperature at 300^{o}C was found to be a crucial parameter in controlling the morphological characteristics of the nanoparticles. Several sets of nanoparticles were synthesized more than once under similar conditions in order to ascertain whether or not results were repeatable.

3.2 Transmission electron microscopy (TEM)

Despite doping with different Gd^{3+} concentrations (15 – 30 mol %), the vast majority of nanoparticles produced from thermal decomposition at 300^{o}C for 1.5 hours were between 15 and 40 nm in size and roughly spherical in shape with some particles appearing to be vaguely hexagonal (Figure 3.1). In most cases, the obtained nanoparticles displayed fairly narrow size distributions with only one shape type and all particles were shown to occur in the β phase. These same morphological characteristics were also observed for a control set of $NaYF_4$:Yb/ Er nanoparticles with no Gd^{3+}. Rarely, and under similar reaction conditions, spherical particles were observed alongside larger hexagonal nanoplates. At concentrations of 30 mol % only spherical nanoparticles were seen and, in one repeat synthesis of $NaYGdF_4$:Yb/Er, a large proportion of particles smaller than 15 nm were obtained. This result somewhat supports observations made in previous studies on Gd^{3+} doping wherein noticeable particle size decreases were observed at doping concentrations of 30 mol % or more [85].

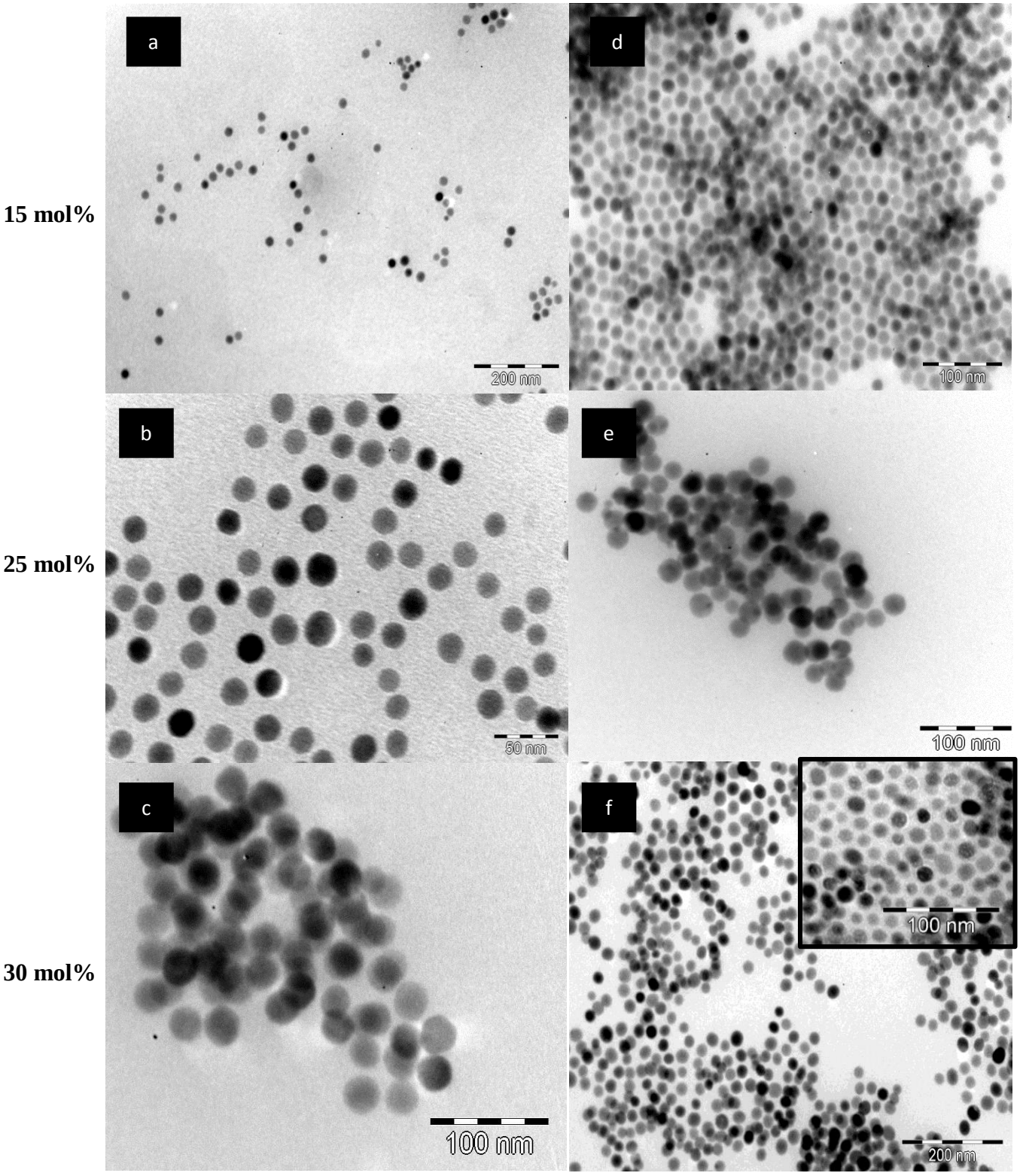

Figure 3.1: TEM images of $NaYGdF_4$:Yb/Tm UCNPs with Gd concentrations of a) 15 mol %, b) 25 mol % and c) 30 mol % and $NaYGdF_4$:Yb/Er UCNPs with Gd concentrations of d) 15 mol %, e) 25 mol % and f) 30 mol %. Inset in (f) shows TEM image for the small particle where the majority of particles are less than 15 nm.

Doping at 5 mol % was also undertaken for both Tm^{3+} and Er^{3+} activated particles; however, both produced unexpected results for two separate reasons. In the case of the Er^{3+} activated set, no viable particles were obtained following an unexplainable reaction failure. For the $NaYGdF_4$:Yb/ Tm synthesis, on the other hand, an accidental rise in temperature from 300 to 310-315 ^{o}C resulted in the formation of striking, large star-of-David shaped nanoplates (Figure 3.2 a and b). Maintenance of the reaction temperature at 300^{o}C, for all syntheses, was done manually by monitoring the reaction temperature using a digital thermometer and simultaneously adjusting it by means of a voltage regulator attached to the furnace. In the case of the star shaped plates, a lapse in supervision lead to a temperature increase which was corrected after 15 to 20 minutes. In a previous synthesis utilizing a Ho^{3+} activator, star shaped particles had been produced following similar temperature control problems (Figure 3.2 d).

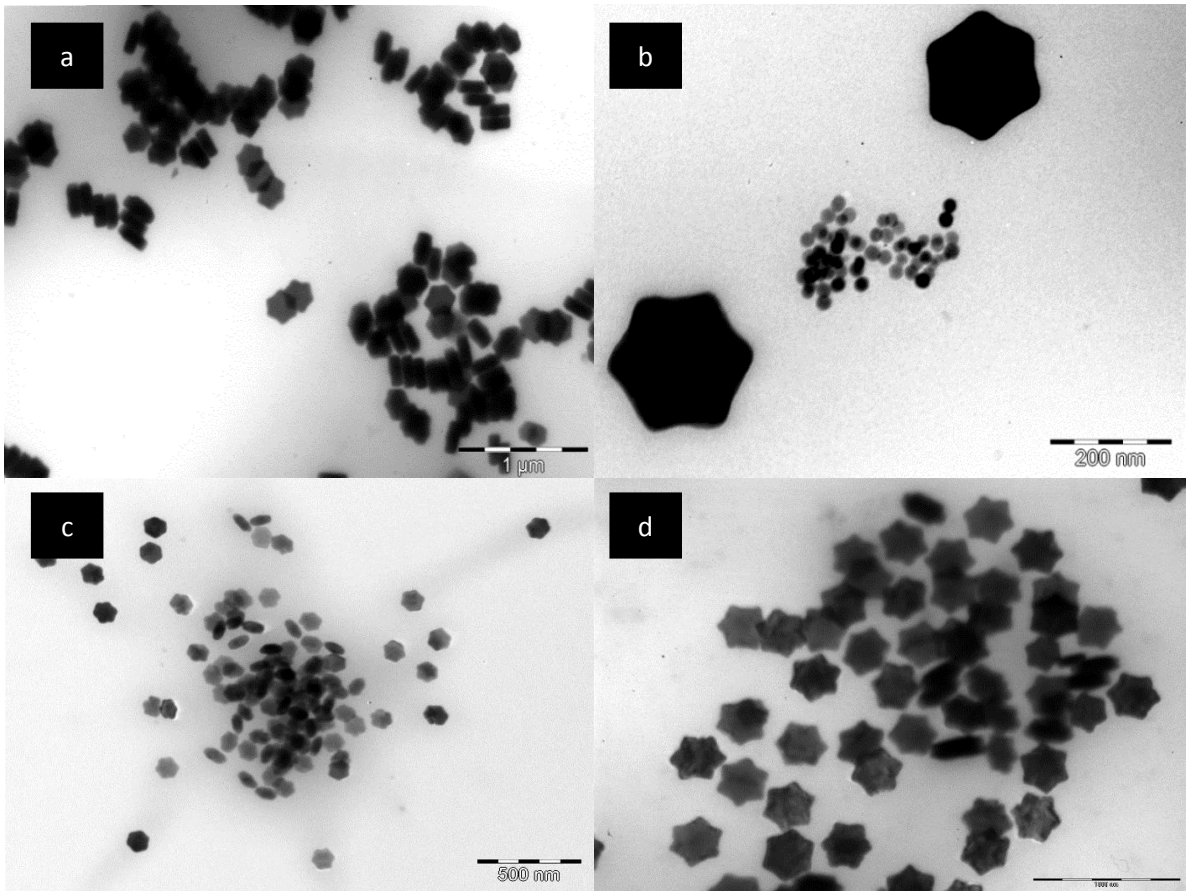

Figure 3.2: TEM images of star shaped nanoplates synthesized at slightly elevated temperatures: a) and b) $NaYGdF_4$:Yb/ Tm with a Gd concentration of 5 mol %, c) $NaYGdF_4$:Yb/Er with a Gd concentration of 5 mol %, d) $NaYF_4$:Yb/Ho nanoparticles.

In order to ascertain whether these results were repeatable, another reaction was undertaken using an Er^{3+} activator with a Gd^{3+} concentration of 5 mol %. This time, the reaction mixture was purposefully heated to 315^{o}C for 20 minutes after which the temperature was reduced to 300^{o}C for the remainder of the reaction. As expected, the particles obtained were star shaped plates with an average length of 100 nm (Figure 3.2 c). These were considerably smaller than those obtained for previous syntheses (250 – 350 nm), suggesting the need for additional experimentation in order to determine the precise temperature and time parameters required to produce star shaped particles of a specific size. The formation of β phase spherical particles may be attributed to the high temperature reaction conditions required for α to β phase transition as well as the presence of oleic acid (OA) which is known to favour formation of β phase particles [228]. The 6:15 ml ratio of oleic acid to 1-octadecene has also been shown to result in spherical β phase crystals [228]. Theoretically, and particularly in the case of small particles, isotropic spherical shapes are known to be thermodynamically favoured as a result of lower surface energies [229]. The growth of larger, anisotropic structures (i.e. rods or plates) is thought to result from Ostwald ripening at higher temperatures, where the formation of larger particles from the dissolution and re-deposition of smaller particle monomers reduces the overall number of atoms occupying high energy positions at particle surfaces and is thus thermodynamically favoured [230]. However, we suspect that in this case, growth of the star shaped nanoplates may have been aided to some extent by the agglomeration of smaller spherical particles (Figure 3.2 b). The formation of nanoplates over nanorods or prisms may be attributed to several factors including high OA to NaOH and NaOH to Ln^{3+} ion concentration ratios as well as relatively low concentrations of F^{-} ions [86, 231, 232]. Higher OA concentrations facilitate greater complexation to surface Ln^{3+} atoms at the expense of F^{-} ions and consequently limit crystal growth [228]. The preferential oleic acid stabilization of the 0001 crystal plane (Figure 3.3) results in growth of the planes perpendicular to the hexagonal crystal c-axis, ultimately producing plate like structures [228]. For our syntheses, OA/NaOH, F^{-}/ Ln^{3+} and NaOH/Ln^{3+} molar ratios were 9.45:1, 4:1 and 2.5:1 respectively. All three occupy ranges which have been shown to promote the growth of large plate structures in previous studies [86, 231, 232]. In addition, the formation of star shaped particles has been reported in at least one other study [86]. Mai et al, synthesized star shaped hexagonal nanoplates via thermal

decomposition of trifluoroacetate precursors. Using HRTEM to examine lattice fringes, they attributed the particle shape to the faster growth rate of the 110 facet at the 6 crystal points in relation to that of the 100 facet at the straight edges. This was observed for an 8 – 12 minute reaction at 330^{o}C while reaction times exceeding 15 minutes were found to produce only hexagonal nanoplates with straight edges.

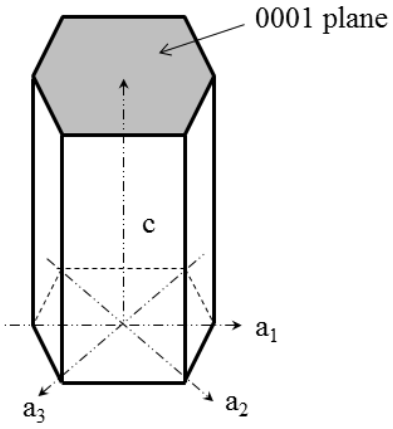

Figure 3.3: Hexagonal crystal showing a and c axes. The highlighted area represents the 0001 plane.

Another feature observed in two sets of spherical particles was the presence of pores (Figure 3.4). Shan *et al*. have attributed the presence of these hollow structures to the Kirkendall effect [233] which involves the movement of a boundary layer between two species, A and B, as a result of one species possessing a higher diffusion rate [234]. This concept is well explained by Kakani [234] who uses the analogy of diffusion between two gases. The analogy examines a situation where two gas chambers at the same pressure, one chamber containing hydrogen and the other argon, are separated by a tube containing a frictionless piston. The gases are then allowed to diffuse through a small hole in the piston. Hydrogen, being lighter than argon, will move faster (down a concentration gradient) into the argon chamber. This will create an increase in pressure and cause the piston to move in the same direction as argon. In their model, Shan et al., have attributed the production of vacancies observed in $NaYF_4$: Yb/ Er spherical crystals to the transition between the cubic and hexagonal phases at high reaction temperatures. In their study, the spherical particles have a central core encircled by a hollow void which is in turn surrounded by a solid shell. At first, the particles synthesised for this work did

not appear to possess the aforementioned structure; however, on closer examination, several particles were found displaying the exact structural description (Figure 3.4 b inset). Shan et al., describe the process of the hollow formation as involving three stages [233]. Firstly, the α phase particle is formed at lower temperatures [233]. Once high enough temperatures are reached to favour the phase transition the particle dissolves and re-grows to form a β phase crystal. Part of the phase transition and growth process involves the fast diffusion of NaF from the surrounding solution, where it is present in higher concentrations, towards the heavy Ln^{3+} containing $NaYF_4$ particle centre [233]. The boundary between the incoming NaF and the existing crystal melt becomes the particle shell which begins to move outward, resulting in the formation of hollows or vacancies [233]. We suspect that the small pores displayed by particles in Figure 3.4 may represent hollow formation in the early stages of diffusion. It is also likely that the diffusion process may occur on somewhat different energy and time scales owing to the fact that an alternative synthetic approach with lower reaction temperatures was used in this work. The exact nature of the parameters needed to repeatedly achieve core-hollow-shell structures using our synthetic approach is unknown and requires additional experimentation with several reaction related variables such as the relative amount of precursors, reaction temperature and reaction time.

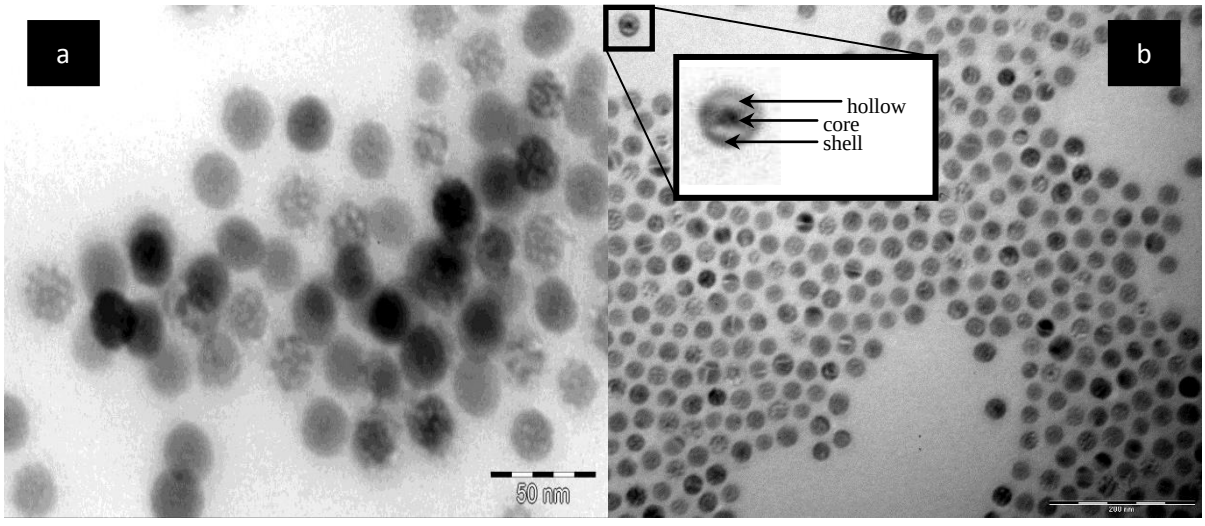

Figure 3.4: TEM images of a) $NaYGdF_4$:Yb/Er with 30 mol% Gd^{3+} and b) Gd^{3+} free $NaYF_4$:Yb/Er nanoparticles displaying pores. Insert: particle displaying core-hollow-shell features.

3.3 Powder X-ray diffraction (PXRD)

Powder X-Ray diffraction patterns were obtained for $NaYGdF_4$:Yb/ Er and $NaYGdF_4$: Yb/Tm nanoparticles with both sphere (30 mol % Gd^{3+}) and star (5 mol % Gd^{3+}) shapes (Figure 3.5 a and b). All diffraction patterns were well matched to β phase crystal systems. In the case of the $NaYGdF_4$:Yb/ Er spheres sample, several sample batches, synthesized under identical reaction conditions, were added together in order to increase the amount of sample available for later applications for conjugation with a phthalocyanine molecule. One of the mixed batches possessed a smaller average particle size (Figure 3.1f insert) and as a result, the size distribution for the sample used for PXRD was slightly larger than for other samples. The broad peak at around $2\theta = 19^{o}$ indicates the presence of surface lanthanide oleates [235]. Whilst these compounds were not used as precursors, we presume that they must have formed in situ, as all reagents necessary for their formation were present in the reaction mixture. Typically, lanthanide oleates or $Ln^{3+}(C_{17}H_{33}\text{-}COO^{-})_3$ form from a reaction between lanthanide chlorides and sodium oleate, which itself is generated by combining oleic acid and NaOH [235]. The broad peak at $2\theta = 19^{o}$ is thought to arise from a lamellar arrangement of lanthanide oleate molecules where the non-polar tails occupy an all trans conformation while the polar head groups are disordered [235].

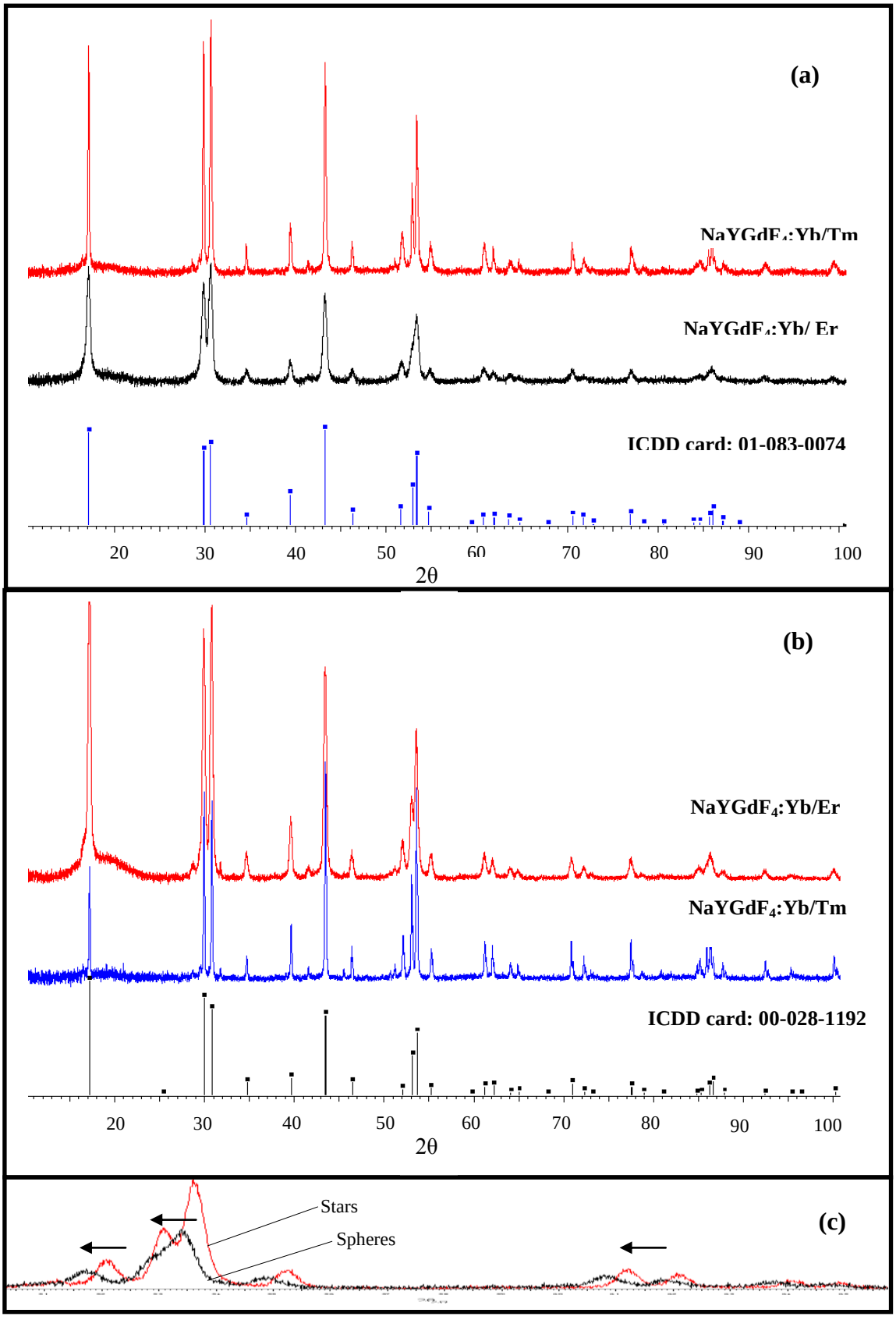

Figure 3.5: PXRD patterns for (a) sphere shaped particles, (b) star shaped particles, (c) $NaYGdF_4$:Yb/Er particles showing a shift to lower angles for the spheres.

The average crystallite sizes of the 4 samples were calculated using the Scherrer equation (Equation 3.1):

$$d(\text{Å}) = \frac{k\lambda}{\beta\cos\theta} \qquad \text{Equation 3.1}$$

where *k* is a proportionality constant with a range of values depending upon the crystallite shape and size distribution (typically a spherical particle is assumed with k = 0.9), λ is the wavelength for the X-ray source (1.5405 Å for a Cu source), β is the line broadening at full width at half maximum of the selected diffraction peak(s) in radians and θ is the Bragg angle. The peak selected for model fitting using the Scherrer method was the 201 reflection at 2θ = 43.5 ^{o}.

Table 3.1: Crystallite sizes and fitting parameters of sphere and star shaped UCNP samples. Width and length refer to the distance along the a axes and c axis respectively (Figure 3.3).

Sample	Size (nm)	RWP (%)	TEM size ranges (nm)
$NaYGdF_4$:Yb/ Er – spheres	27	7.7	10 - 27
$NaYGdF_4$:Yb/ Tm – spheres	51	10.2	25 - 35
$NaYGdF_4$:Yb/ Er – stars	28	19.9	40 - 50 (length) 105 - 115 (width)
$NaYGdF_4$:Yb/ Tm – stars	70	11.4	90 - 100 (length) 230 - 250 (width)

The relatively small size distribution and monocrystalline nature of the samples allowed for a reasonable application of the Scherrer method and despite fairly large RWP, weighted profile residuals, the calculated sizes were, for the most part, similar to those obtained using TEM (Table 3.1). Although the Scherrer method should only be used for particles possessing a roughly spherical shape, as the particle diameter remains constant regardless of the diffraction angle, [236] for the anisotropic star shaped particles, the calculated sizes were closer in value to the crystallite length (or

thickness) along the c axis. This makes sense when considering that crystallite sizes obtained using diffraction generally represent the thickness along the direction of diffraction [236]. In this case, sizes represent the crystallite thickness measured using reflections off the 201 plane which lies at an oblique angle through the unit cell. Our attempt to fit diffraction data from star shaped plates to an essentially spherical model is likely to have resulted in higher RWP values for these samples than for the spherical ones. The size obtained for the $NaYGdF_4$:Yb/Tm sphere sample, however, was larger than the average size observed using TEM. Since the Scherrer method relies on peak broadening which is attributed to crystallite size alone [236], completely accurate values are often unattainable, even with instrument broadening corrections, owing to peak broadening produced by additional phenomena such as microstrain effects [236]. It was also noticed, upon closer examination of the TEM data, that the Tm^{3+} doped sphere sample possessed a small number of larger star shaped particles which could have influenced the calculated mean size. These particles were found to be Er^{3+} doped contaminants from a separate sample and this is discussed below in Section 3.5.

The spherical particles were also observed to possess diffraction peaks which were shifted to lower angles when compared to those of the star shaped plates (Figure 3.5 c). This may be attributed to larger d spacing associated with an increase in the unit cell lattice parameters upon the increase in Gd^{3+} concentration (30 mol % for the sphere particles versus 5 mol % for the star particles) as Gd^{3+} possesses a larger ionic radius than Y^{3+} [85]. In order to demonstrate the lattice parameter increase for our samples, as well as to determine crystallite sizes using a whole powder fitting method, Rietveld refinement was performed on the lattice parameters and Lorentzian crystallite sizes using the Er^{3+} activated sphere and star shaped samples. Refinement using the Rietveld method typically requires prior knowledge of the sample's crystal structure as well as the atomic positions therein. For the $NaYF_4$ system, there has been much debate concerning the exact nature of the hexagonal phase unit cell with regard to whether the system possesses a space group of $P\bar{6}$ or $P6_3/m$. $P\bar{6}$ has 5 atomic sites, where Ln^{3+} cations occupy 9 fold co-ordination sites 1a, on the unit cell corners, and half of 1f, in the centre [237]. The other half of the 1f sites are occupied by Na^+ which also occupies two 2h sites in the centre in a 1:1 ratio with vacancies [237] . The F^- anions are co-ordinated to the cations at two sites,

3k and 3j [237]. In contrast, the $P6_3/m$ space group is simpler and possesses only three sites: 2b, on the unit cell corners, which is occupied by Na^+, 2c, in the centre, which is randomly occupied by Ln^{3+} and Na^+ and 6h, the co-ordination site of the F^- anions [238]. Some studies suggest that $P\bar{6}$ is the correct space group [237, 239]; however, other sources have stated that $NaYF_4$ is isostructurally related to the mineral gargarinite, $NaCaLaF_6$, which possesses the $P6_3/m$ space group [238]. The ICDD reference patterns for $NaYF_4$ (Figure 3.5 b) and $NaCaLaF_6$ (Figure 3.5 a) with $P6_3/m$ space groups are very similar. The gargarinite structure was found to be a better match for the spherical particles. Some studies have also highlighted the deviation in stoichiometry from 1:1:4 for $NaYF_4$. One such study was published in 2004 by Kramer, Gudel and co-workers [238]. Using Rietveld refinement, they reported a possible non-stoichiometric formula of $Na_{3x}Y_{2-x}F_6$ for hexagonal phase sodium yttrium fluoride with a $P6_3/m$ space group [238]. The non-stoichiometry was attributed to a significant number of vacancies for the 2b site [238]. For this work, the structural model and atomic positions proposed by Kramer et al., with $P6_3/m$ space group symmetry, produced the best refinement fit. For the star shaped particles, lattice parameters of a = 5.978 and c= 3.514 were obtained while for the spherical particles values of a = 5.993 and c = 3.530 were yielded. As expected, the spherical particles showed an increase in lattice parameter values owing to the higher concentration of Gd^{3+}. The Lorentzian crystal sizes were found to be around 25 nm for the spheres, similar to the values obtained using the Scherrer equation, and 38 nm for the star shaped particles. Despite fitting the whole pattern, the star shaped particles did not produce a value much different from that obtained using the Scherrer method and, again, this may be a result of the distortion in particle size values obtained when working with anisotropic crystals. The values reported here for the refinement represent the best fit that could be obtained with our powder diffraction data; however, these fittings were by no means excellent, especially for the lower angle region. We attribute this to the amount of sample which was used for the PXRD experiments, as a constant sample thickness could not be obtained.

3.4 Scanning electron microscopy - energy dispersive X-ray spectroscopy (SEM-EDX)

The SEM-EDX spectra for the two spherical and two star shaped UCNPs are shown in Figure 3.6. As expected, all host lattice and dopant elements were observed with the exception of Tm. We presume that the instrument was unable to detect a Tm signal owing to the low dopant concentration of Tm used (0.2 mol %). In addition, C, O and Cl signals were detected, indicating the presence of the capping agent and $LnCl_3$ precursor residues respectively. The spherical particles were also shown to produce peaks with slightly higher intensities in comparison to the star shaped ones. This is most likely a result of the higher surface area to volume ratio possessed by smaller particles which causes a larger proportion of the total number of atoms to occupy positions on the particle surface where they are more easily detected. Using SEM-EDX, it was also possible to estimate the atomic composition of the nanoparticles. The percentages of the constituent atoms for the four nanoparticle samples are shown in Table 3.2. It is important to note that the sample preparation used for this technique severely reduces the reliability of this data and that these atomic compositional values should only be used for interpretation of the relative amounts of constituent atoms at best. Accurate elemental analysis using EDX related techniques requires that the sample possess a uniform thickness and thus, in this case, where powder samples were attached to sample holders by means of adhesive tape, we cannot presume that the compositional data is entirely accurate. However, the relative amounts of constituent elements appear to represent the expected trends based on the original concentrations used. For example, in the $NaYGdF_4$:Yb/Er samples, the molar amounts of F^-, Na^+ and Ln^{3+} used during synthesis were 0.0032 mols, 0.002 mols and 0.0008 mols respectively. Of the 0.0008 mols of lanthanide ions, the mol % concentrations of Y, Gd, Yb and Er were 50 %, 30 %, 18 % and 2 % respectively. Thus, we would expect the trend in relative amounts to be F>Na>Y>Gd>Yb>Er and this is precisely what we observe in the EDX compositional data. Most interestingly, the Na:F ratio for all the samples appears to be closer to 1:6 than 1:4, suggesting that the actual compositional formula for our samples is $NaYF_6$. This supports the results observed for Rietveld refinement, where the diffraction data was best fit to a non-stoichiometric $Na_{3x}Ln_{2-x}F_6$ structure. However, in order to unequivocally confirm these speculations, additional analyses using other techniques like electron energy loss spectroscopy or inductively coupled plasma optical emission spectroscopy (ICP-OES),

where accurate compositional data can be obtained, should be undertaken. Subsequent to this, we shall continue to refer to the UCNP samples using the $NaYF_4$ formula.

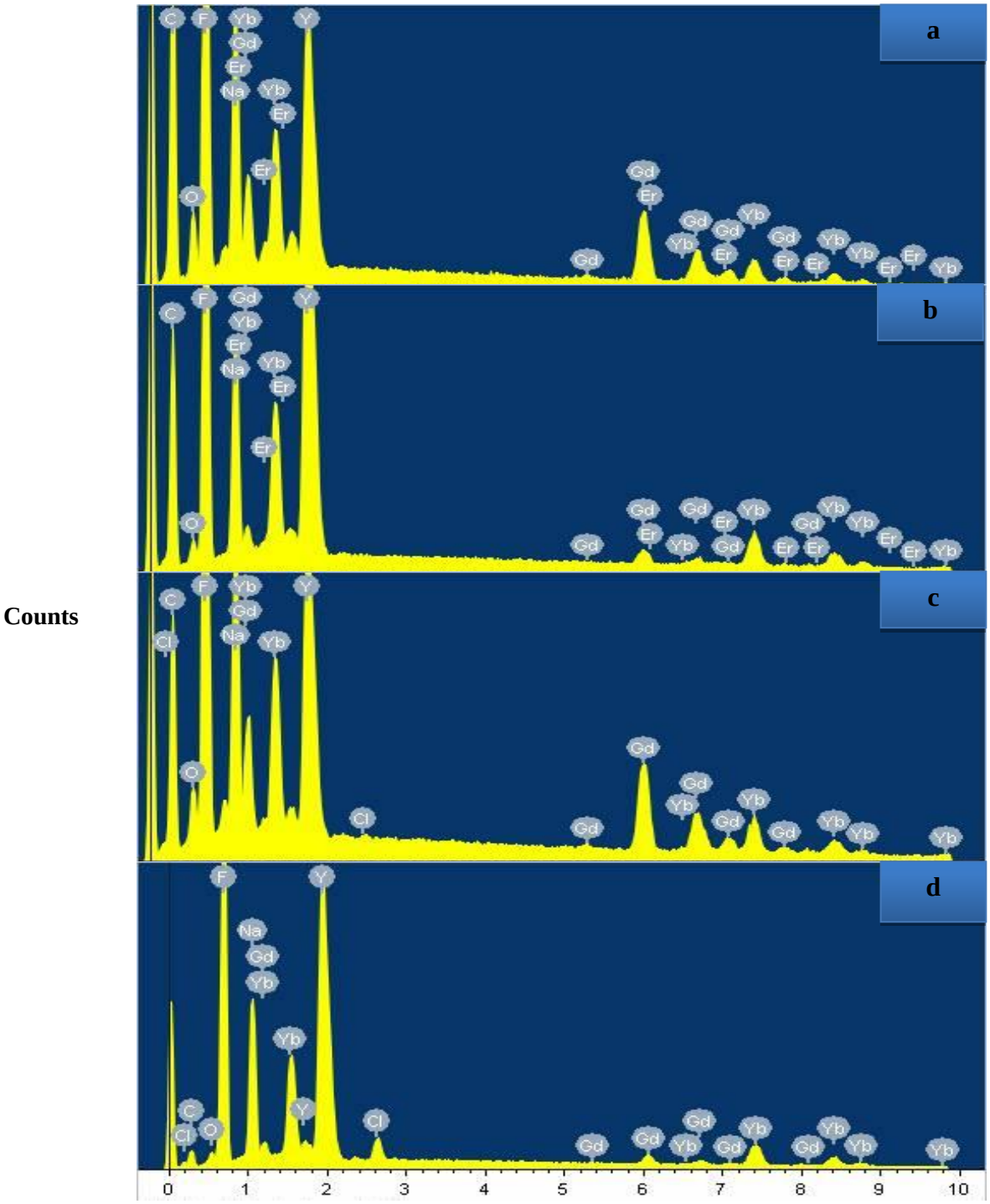

Figure 3.6: SEM-EDX spectra of $NaYGdF_4$:Yb/ Er UCNP spheres (a) and stars (b) and $NaYGdF_4$:Yb/Tm UCNP spheres (a) and stars (b).

Table 3.2: Atomic composition of sphere and star shaped UCNPs using EDX data.

Elements	Atomic %			
	$NaYGdF_4$:Yb/Er		$NaYGdF_4$:Yb/Tm	
	Spheres	Stars	Spheres	Stars
C	52	51	41	14
O	5	2.1	3.5	2.17
F	31	34	42.14	60
Na	5	5	6	10
Y	3	5.43	3.66	9.41
Gd	1.62	0.38	1.89	0.58
Er	0.12	0.09	0	0
Yb	0.84	1.29	1.06	2.15
Cl	0	0	0.06	1.05

3.5 Electron paramagnetic resonance (EPR)

EPR spectra of several Gd^{3+} doped UCNP samples where obtained in order to ascertain whether or not they displayed any paramagnetic characteristics. The EPR spectrum of a $NaYGdF_4$:Yb/Er sample containing 15 mol % Gd^{3+} is shown in Figure 3.7. All Gd^{3+} containing samples displayed similar results. As expected, Gd^{3+} doped samples displayed a broad peak with a g-value in the region of 2.01, similar to the value for a free e^-, as the spin orbit coupling contribution is particularly low owing to the Gd^{3+} ion's possession of a half filled 4f subshell [240]. These results support those observed for the same system in other studies [241]. The EPR spectral features of Gd^{3+} doped $NaYF_4$ have been well summarised in a study by Komban et al. [241] The broad peak originates from a transition between two magnetically induced energy levels arising from the Zeeman effect [240, 241]. Since Gd^{3+} possesses seven unpaired electrons, these are able to interact magnetically with each other. This should result in a type of super hyperfine interaction, termed zero field splitting as it occurs without the presence of an external magnetic field [240, 241]. However, this additional peak detail for the g=2.01 peak was not observed and likely requires higher frequency or colder temperature analysis [240]. The broadness of the observed peak has also been attributed to large Gd^{3+} concentrations where spin spin interactions between adjacent Gd^{3+} ions are likely to occur with higher probability [241]. In addition to the broad Gd^{3+} peak, 2 other peaks are displayed in Figure 3.7. These were shown to be

products of the nmr tube sample holder and a paramagnetic marker inside a capillary tube within the strong field resonator. The presence of more than one peak for Gd^{3+} ions can be used to infer their occupation of more than one crystal site within the host lattice [241]. Since our data displays only one major peak, we assume that the vast of majority of Gd^{3+} ions occupy only one site (presumably the 2a site for the $P6_3/m$ space group). Small line fluctuations at around 600 and 4800 G may be indicative of additional Gd^{3+} lattice positions; however, they may also be instrumental artefacts.

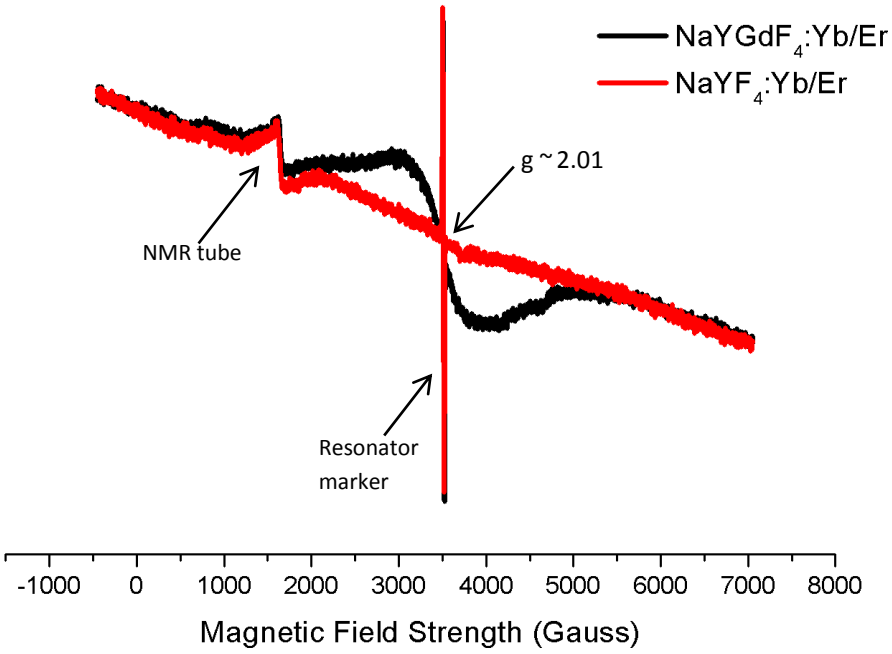

Figure 3.7: EPR spectra of UCNPs containing 0 and 15 mol % Gd^{3+}. Spectra were obtained at a frequency of 9.843 GHz.

3.6 Thermo-gravimetric analysis (TGA)

TGA analyses were carried out on $NaYGdF_4$:Yb/Er sphere and star shaped nanoparticles. Both samples displayed relatively high thermal stability, even at 500 ^oC, where no more than a 30 % mass reduction was observed. Figure 3.8 shows that both samples experienced a small mass loss (< 2.5%) between 50^o and 280^o. This might be attributed to dehydration and/ or loss of adsorbed organic

solvent molecules as the samples were simply oven dried at 60 ^{o}C and not under high vacuum. The spherical particles displayed a large mass reduction from around 400^{o}C in what appears to be a one step process. The star shaped particles, in contrast, showed a more marked mass decrease with a first mass loss step occurring from around 275^{o}C and, perhaps, a second from 430^{o}C. We expected these mass losses to have resulted from the decomposition of oleic acid; however, other studies concerning oleic acid stabilized nanoparticles display sharp mass losses which begin at around 200^{o} [242]. Since our samples underwent several washing steps in order to remove free oleic acid and 1-octadecene, to yield dry powders, it is possible that the remaining, well attached, oleic acid molecules are more thermally stable and begin to decompose at slightly higher temperatures. The TGA curves may also represent the decomposition of surface attached rare earth oleates [235].

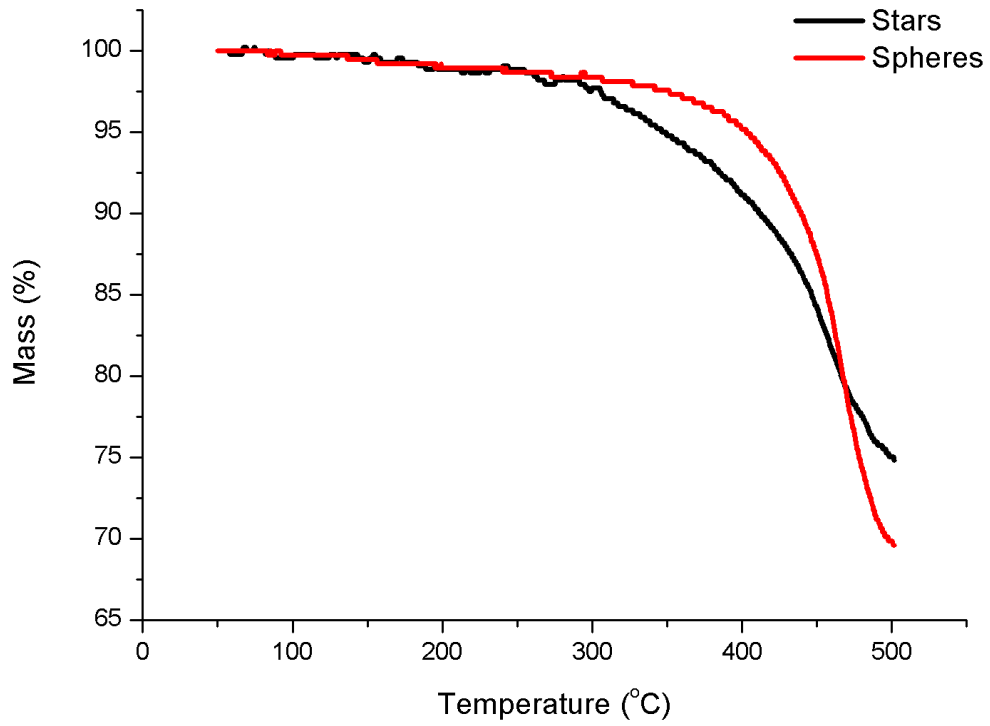

Figure 3.8: TGA curves of $NaYGdF_4$:Yb/Er UCNP spheres and stars showing percentage mass loss with an increase in temperature.

3.7 Steady state and time resolved fluorescence spectroscopy

Steady state fluorescence spectroscopy was performed on the $NaYGdF_4$:Yb/Er(Tm) sphere and star shaped samples utilizing 972 nm continuous wave laser excitation. UCNP samples (10.4 mg) were dissolved in 3 – 4 ml of toluene. The Er^{3+} activated UCNPs produced emissions at around 840 nm, 660 nm, 550 nm and 530 nm as well as a very weak emission at around 410 nm (Figure 3.9). These emissions may be attributed to the $^4S_{3/2}$ - $^4I_{13/2}$, $^4F_{9/2}$ - $^4I_{15/2}$, $^4S_{3/2}$ – $^4I_{15/2}$, $^2H_{11/2}$ – $^4I_{15/2}$ and $^2H_{9/2}$ - $^4I_{15/2}$ transitions respectively (Figure 1.3) [68]. Contrastingly, the Tm^{3+} doped samples displayed emissions at around 800 nm, 650 nm, 475 nm, 450 nm as well as a very low intensity emission at 360 nm (Figure 3.10). In this case, emissions occur as a result of the $^3H_4$ – $^3H_6$, $^3F_2$,$^3F_3$ – $^3H_6$, $^1G_4$ - $^3H_6$, $^1D_2$ – $^3F_4$ and $^1D_2$ – $^3H_6$ transitions respectively (Figure 1.3) [68]. In addition to the expected emission peaks seen for the Tm^{3+} ion in the sphere shaped sample, a peak in the green region, at around 548, as well as a small peak at 410 nm were also observed (Figure 3.9). As Tm^{3+} is not known to produce emissions at 548 nm we could only conclude that this peak must have arisen as a result of contamination with Er^{3+}. If the contamination had arisen as a result of trace amounts of Er^{3+} from, for example, contaminated solvents or glassware one would expect the emission intensities for the foreign peaks to be much lower than those in Figure 3.10. Thus, we presumed that additional emission peaks arose as a result of contamination with whole Er^{3+} doped nanoparticles and, indeed, upon re-evaluation of the Tm^{3+} doped spherical sample's TEM grids we observed several star shaped nanoparticles of around 100 nm in length. The Tm^{3+} doped spherical particles and the Er^{3+} doped star shaped particles were synthesized and washed simultaneously and it is likely that, at some point, some of the solution containing the Er^{3+} doped star particles was accidently added to the solution containing the Tm doped spheres. Interestingly, no Er^{3+} contamination was detected by EDX.

It is well known that larger UCNPs, with smaller surface area to volume ratios, suffer less from environmental quenching effects as a result of there being a smaller proportion of dopant atoms at the surface [243]. Thus, we anticipated that the larger star shaped particles would display more intense fluorescence. This was observed in the Tm^{3+} doped samples, where the star shaped UCNPs were significantly larger than the spherical ones. However, both Er^{3+} doped UCNPs displayed very similar

emission intensities. In addition, both sets of spherically shaped particles displayed higher intensity emissions in the UV region, indicating that the intermediate states facilitating the population of the higher energy levels must be experiencing lower rates of relaxation from quenching and/ or phonon loss. It is possible that the smaller size difference between the Er^{3+} doped stars and spheres, in comparison to the Tm^{3+} doped ones, results in the emission intensities for the two samples being very similar. The effect of the crystal lattice arrangements and energies on the upconversion emission intensity has been highlighted elsewhere and we suspect that this may have an influential role in the fluorescence of our samples [244]. One effect of doping with Gd^{3+}, already mentioned above, is an increase in the hexagonal nature of the nanocrystals and an associated reduction in symmetry [85]. It is possible that this reduction in crystal symmetry favours the transitions between intermediate states of the dopant ions, facilitating an increase in higher energy state populations and, consequently higher UV emission intensities. We have also shown that the lattice parameters of the unit cell increased upon doping with higher Gd^{3+} concentrations. This should result in an increase in inter atomic distances and reduce higher energy level population loss via cross relaxation processes [244].

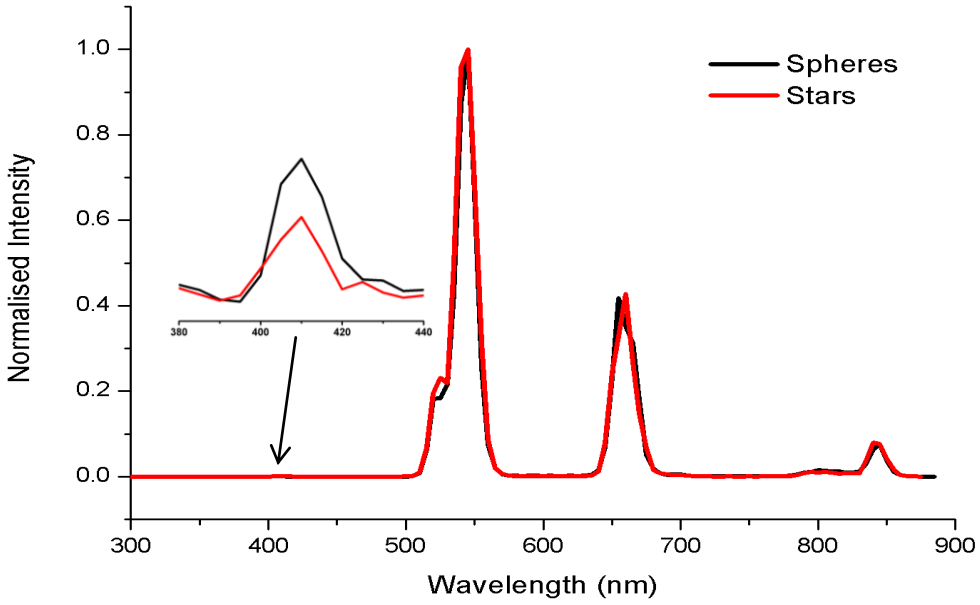

Figure 3.9: Upconversion emission spectra of $NaYGdF_4$:Yb/Er sphere and star shaped UCNPs in toluene. Insert showing weak intensity emission peak at 410 nm. λ_{ex} = 972 nm.

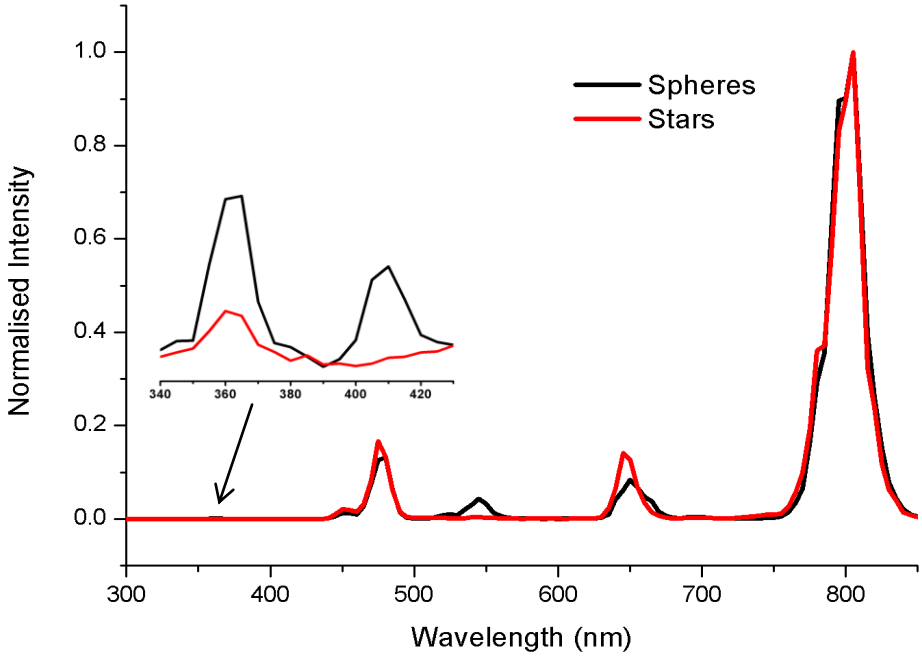

Figure 3.10: Upconversion emission spectra of $NaYGdF_4$:Yb/Tm sphere and star shaped UCNPs in toluene. Insert showing weak intensity emission peak at 360 nm. λ_{ex} = 972 nm.

Time resolved fluorescence measurements were also obtained for the green, red and NIR emissions of the Er^{3+} activated particles as well as the blue, red and NIR emissions of the Tm^{3+} activated particles. Owing to the fact that, in upconversion fluorescence, population of the energy levels from which fluorescence emissions arise is facilitated by the initial population of intermediate states, the acquisition and interpretation of time resolved data can be fairly complex. Generally, an entire time resolved fluorescence spectrum possesses both a rise and a decay component which refer to the time needed to populate and depopulate excited states respectively. In the literature, the interpretation of these components varies. One study, where a kinetic model was fitted to the entire curve, reported two lifetimes which were taken to represent the decay and rise times [245]. They argued that, since the long lived intermediate states represent the limiting step in the time mediated population of the higher excited states, the true decay time of the emitting states is better represented by the rise time [245]. However, other studies have reported the decay times of the emitting levels using mono exponential fits of the decay portion of the time resolved curve only [246] while still other studies have suggested that the application of exponential fitting models is inappropriate altogether [247]. In this work, time resolved emissions were obtained using high repetition rate, burst mode lasing where multiple laser

pulses result in the emission of one photon. The use of burst mode results in the obstruction of rise time measurements owing to the fact that the rise curve now represents the burst pulses. Therefore, for this work, tail fittings were performed only on the decay curve portion of the time resolved spectrum. Lifetimes were calculated using a multi exponential tail fit equation (Equation 3.2) [248]:

$$I_{(t)} = \sum_{i=1}^{n} A_i e^{\frac{-t}{\tau_i}} \qquad \text{Equation 3.2.}$$

where n represents the number of exponential components and A_i and τ_i represent the amplitude and decay time of the i^{th} exponential component. A single exponential component was found to best fit the data, with fitting χ^2 values equal to around 1, and all decays could be quantitatively expressed with one lifetime value (Table 3.3). The statistical fitting errors for the calculated lifetime values where obtained using support plane error analysis and the number of bursts, collection time and bin width parameters were adjusted for each emission in order to yield the smallest fitting errors. In general, we found that increased bin widths and collection times were needed in order to obtain reasonable values for the longer decays. The decay curves and lifetime measurements of the four UCNP samples are shown in Figure 3.11 and Table 3.3, respectively. The Er^{3+} activated samples displayed considerably shorter lifetimes than those of the Tm^{3+} activated samples. One possible reason for this is the difference in dopant concentration. As Er^{3+} is included in the host crystal lattice at 2 mol %, ten times higher than the 0.2 mol % of Tm^{3+}, it is more likely to undergo lifetime reduction as a result of increased cross relaxation. The lifetimes for the Er^{3+} doped sphere and star shaped particles showed similar trends, with the green and NIR emissions displaying similar values while the red emission lifetimes were longer. The similarity in green and NIR lifetimes is easily accounted for, as both emissions arise from the $^4S_{3/2}$ state (Figure 1.3) [68]. The longer decay time for the red emission may relate to the $^4F_{9/2}$ state possessing a greater inherent stability and the fact that it is not involved in a major phonon loss pathway (Figure 1.3) [68]. Interestingly, the green and red emissions for the star shaped UCNPs showed a respective decrease and increase in lifetimes when compared to the sphere shaped particles. This was unexpected, as larger particles, with smaller surface area to volume ratios, are known to possess longer lifetimes [243, 244]. Again, this may be a result of crystal lattice

changes, as a result of differing Gd^{3+} concentrations, playing as big a role in emission dynamics as particle size. It is possible that the smaller lattice parameters and corresponding shorter inter atomic distances in the star shaped particles effectuate an increase in phonon lattice energy [244] resulting in a decrease in the $^4S_{3/2}$ lifetime. The $^4F_{9/2}$ lifetime, which is influenced less by phonon loss, in contrast, may benefit from the larger particle size and consequently increase. The lifetimes observed for the Tm^{3+} activated UCNPs mirror the results obtained for steady state fluorescence in that, as expected, the significantly larger star shaped particles display longer lifetimes. Again, the lower energy $^3H_4$ state probably benefits from a larger inherent stability and, like the $^4F_{9/2}$ state in Er^{3+}, is not involved in a major phonon loss pathway [68], resulting in its possession of longer lifetime values.

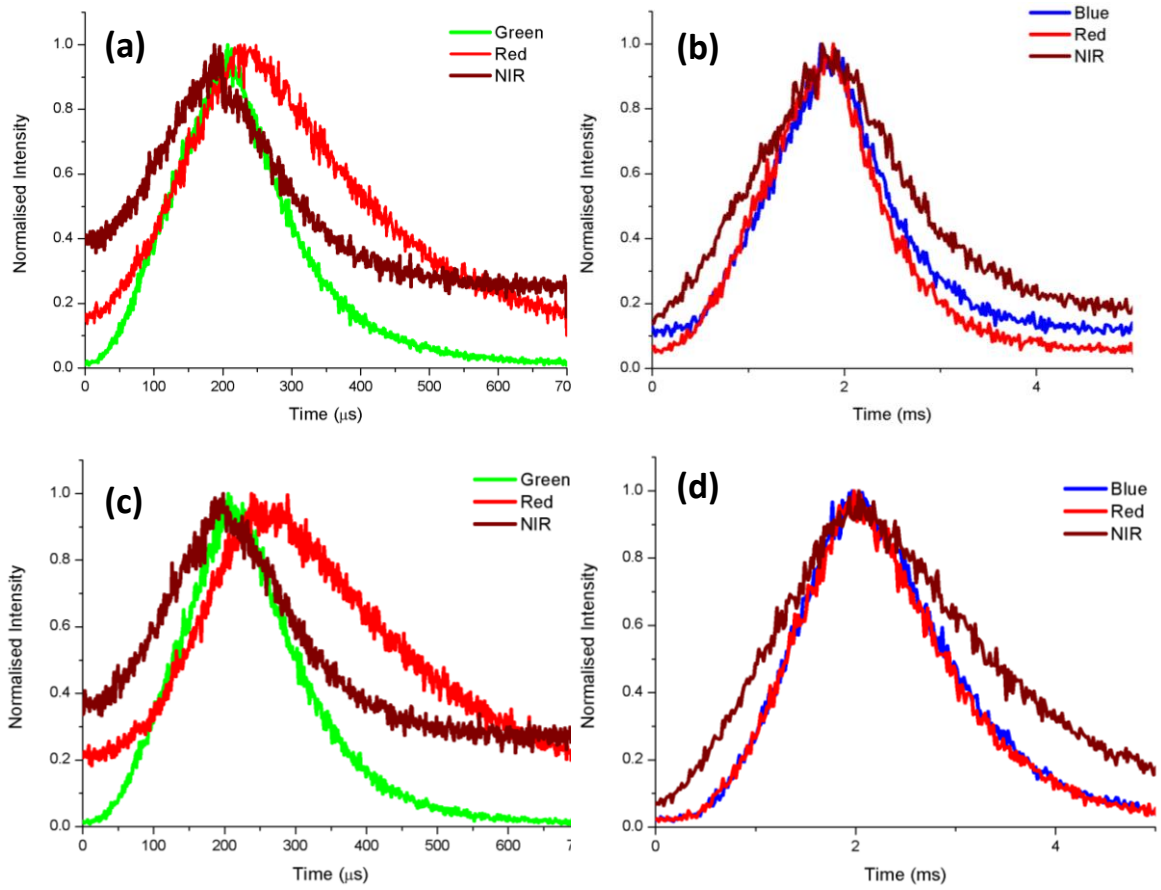

Figure 3.11: Time resolved upconversion emission spectra of green (blue), red and nir emissions for a) $NaYGdF_4$:Yb/Er spheres b) $NaYGdF_4$:Yb/Tm spheres, c) $NaYGdF_4$:Yb/Er stars and d) $NaYGdF_4$:Yb/Tm stars. λ_{ex} = 972 nm.

Table 3.3: Fluorescence lifetimes of the upconversion fluorescence emissions for sphere and star shaped UCNPs

	Emissions	τ_F (ms)	Errors (ms)	χ^2
$NaYGdF_4$:Yb/Er Spheres	Green	0.093	± 0.001	1.005
	Red	0.183	+ 0.015 - 0.013	1.100
	NIR	0.099	± 0.003	0.987
$NaYGdF_4$:Yb/Er Stars	Green	0.082	± 0.002	1.015
	Red	0.263	+ 0.019 - 0.016	1.095
	NIR	0.094	± 0.003	1.081
$NaYGdF_4$:Yb/Tm Spheres	Blue	0.579	+ 0.016 - 0.015	0.975
	Red	0.527	± 0.013	1.145
	NIR	0.800	± 0.028	0.966
$NaYGdF_4$:Yb/Tm Stars	Blue	0.748	+ 0.014 - 0.013	0.985
	Red	0.706	± 0.018	1.086
	NIR	1.210	± 0.030	0.974

3.8 Steady state downconversion fluorescence

In addition to the UC emissions produced using 972 nm excitation, conventional, or downconversion, fluorescence was also observed for three UCNP samples: the $NaYGdF_4$: Yb/ Er spheres with a 15 mol % Gd^{3+} concentration (Figure 3.1d) as well as the Gd^{3+} free $NaYF_4$:Yb/Er (Figure 3.4b) and $NaYF_4$:Yb/Ho (Figure 3.2d) samples. All three samples produced a broad fluorescence emission peak with a maximum at around 560 nm upon 480 nm excitation. This phenomenon has been reported in at least one study, where it was attributed to a ligand to metal charge transfer process induced by the presence of oleic acid ligands on the nanoparticle surface [106]. In order to ascertain the provenance of the emission, the oleic acid, on its own, was examined for fluorescence activity. The oleic acid alone, when dissolved in cyclohexane, did not appear to produce any significant fluorescent emissions. This supports the findings in [106] and indicates that the charge transfer mechanism most probably arises as a result of an interaction, or co-ordination, between the oleic acid and the metals at the nanoparticles surface. The study in [106] also highlighted the association between efficient ligand

to metal charge transfer and the absence of the oleic acid alkene group where the alkene group was thought to hinder the electron donating ability of the oleic acid. In support of this theory, the study found no alkene group carbon NMR signals for the UCNP samples. The absence of the alkene group was attributed to the high temperatures used for thermal decomposition; however, no mechanism was suggested. In contrast to this theory, however, infrared spectroscopy of our samples displayed the characteristic =C-H bend and C=C stretch of an alkene group at 724 cm^{-1} and 1644 cm^{-1} respectively. In this work, the possible application of UCNPs in the fluorescence sensing of radicals was examined using their downconversion emissions. The broad charge transfer emission band was found to be quenched upon the addition of a DPPH radical (Figure 3.12) solution (2.5 x 10^{-3} M) which was added drop wise (0.05 ml per drop) into a solution of $NaYF_4$:Yb/Ho UCNPs. Both DPPH and UCNPs were dissolved in cyclohexane. It is possible that the addition of the DPPH radical resulted in the degradation of the oleic acid via cleavage of the alkene double bond or reduction of carbon atoms close to the alkene group, consequently diminishing the electron donating ability of the oleic acid ligand within the charge transfer mechanism. Interestingly, the re-examination of the downconversion abilities of our UCNPs after several months did not yield any charge transfer bands. This may have resulted from two possible influences. Firstly, the thermal decomposition approach used to synthesize the nanoparticles was found to yield particles which were sticky and difficult to handle. In an attempt to address this, the particles were thoroughly cleaned by dispersing the nanoparticles in cyclohexane and re-precipitating them with ethanol several times. This rigorous washing approach was employed for the majority of the UCNP samples and could possibly have resulted in the removal of a large portion of the surface ligands. In the case of two samples ($NaYF_4$:Yb/Er and $NaYF_4$:Yb/Ho) however, no washing was undertaken and yet, after several months of storage, the particles were unable to produce any downconversion emissions. Since unsaturated fatty acids are commonly known to exhibit degradation via oxidative rancidification on long term storage, it is possible that oxidation of the alkene group resulted in fluorescence quenching [249].

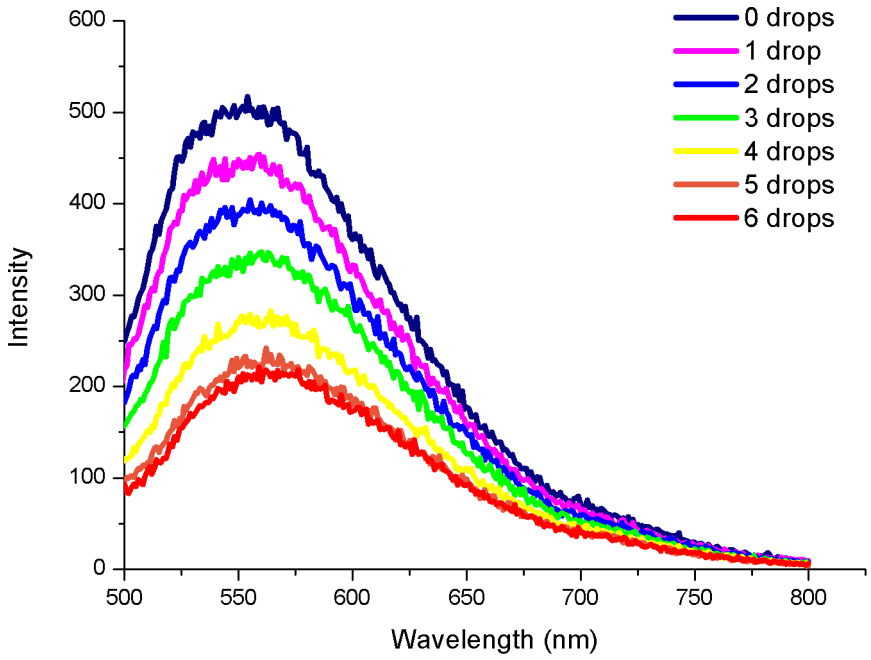

Figure 3.12: Quenching of UCNP downconversion fluorescence emission with the addition of 0 – 6 drops (0.05 ml per drop) of a DPPH radical solution (2.5 x 10^{-3} M) in cyclohexane.

3.9 Synthesis and characterization of silica coated UCNPs

In order to facilitate covalent attachment to an AlOCPc, the UCNPs were coated with silica and further functionalised with aminopropyltriethoxy silane (APTES). The silica coated and APTES functionalized particles are represented as $NaYGdF_4$:Yb/Er@Si and $NaYGdF_4$:Yb/Er@Si@APTES, respectively. The particles selected for silica coating and further conjugation to an (Cl)AlOCPc were the $NaYGdF_4$:Yb/Er sphere shaped particles. Since the yield of silica coated UCNPs per synthesis was relatively low, around 27 mg, several sets of these particles were produced in order to ensure that suitable amounts were available for conjugation and all sets possessed similar TEM, IR and fluorescence characteristics. All of the silica coated nanoparticles produced contained a Gd^{3+} concentration of 30 mol % with the exception of the one set of UCNPs which was used to do the initial conjugation reaction. That particular set possessed a Gd^{3+} concentration of 15 mol %. As will be discussed in chapter 5, the synthesis of the conjugate did not yield reproducible results; however,

the analytical data obtained for the very first set of conjugate particles produced was particularly interesting. As such, the TEM and IR results discussed here are those obtained for that first set of UCNPs as these are also relevant to the discussion on the conjugate. Unfortunately, the small yield of the initial conjugate sample did not allow for further upconversion fluorescence measurements and the upconversion fluorescence data could only be obtained for the samples containing 30 mol % Gd^{3+}. They are discussed here only to highlight general changes in the emissions of UCNPs when coated with silica. Although the amount of Gd^{3+} contained within these sets of samples is different we do not expect this to have resulted in any noticeable changes in the fluorescence properties of the conjugated AlOCPc as both sets of particles possess the same shape and crystal phase, very similar size distributions as well as identical surface functionalization.

Silica coated UCNPs were synthesized by means of a reverse microemulsion method (Scheme 3.1). Very simply, added surfactant molecules behave as nano sized 'reaction chambers' by enclosing small concentrations of water and ammonia around the oleic acid stabilized UCNPs in a reverse phase micelle [2]. The silica shell is created as tetraethoxysilane (TEOS) becomes concentrated within the micelle and ammonia facilitates the creation of the surface OH groups [2]. The inclusion of nanoparticles within the micelle is reported to involve the initial replacement of surface ligands by surfactant molecules and TEOS [250]. The silica coated nanoparticles can then be further functionalized with APTES.

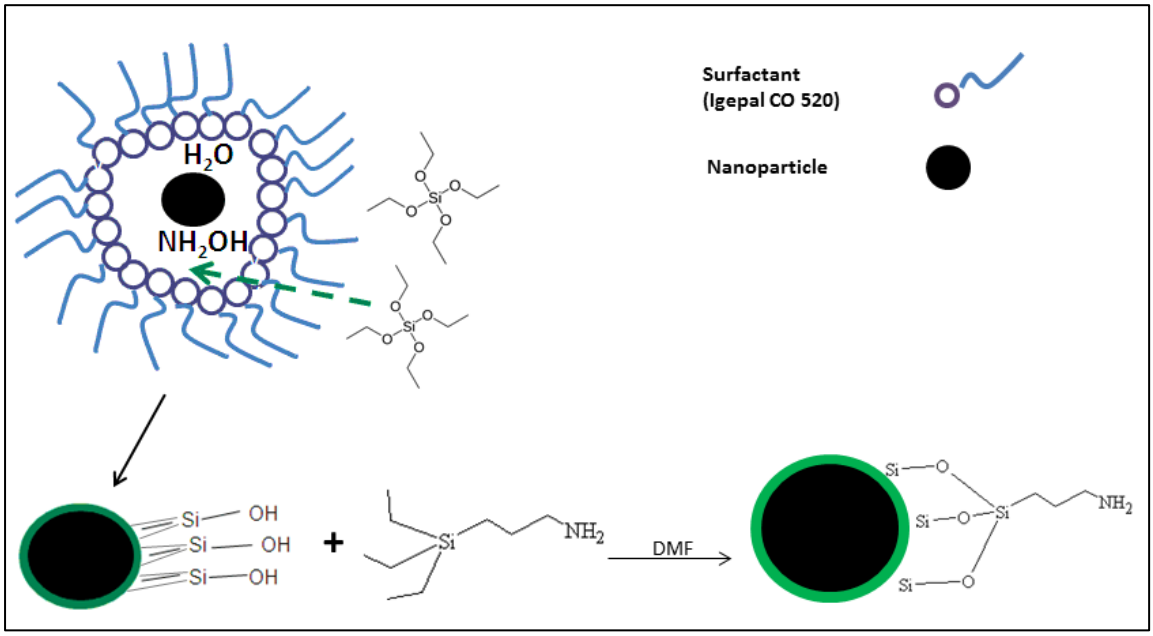

Scheme 3.1: Simplified representation of the reverse microemulsion synthesis and APTES functionalization of $NaYGdF_4$:Yb/Er@Si UCNPs.

The white rings surrounding the UCNPs are clearly visible on the TEM micrograph in Figure 3.13, indicating that the UCNPs were successfully coated with silica. From the TEM image, the average thickness of the silica shell was estimated to be around 10 nm. Also shown in the TEM image are small white silicon nanoparticles which are an expected, yet unwanted, by-product of reverse microemulsion. Vigorous washing assisted in the removal of most of the silica nanoparticles; however, it is virtually impossible to remove them entirely.

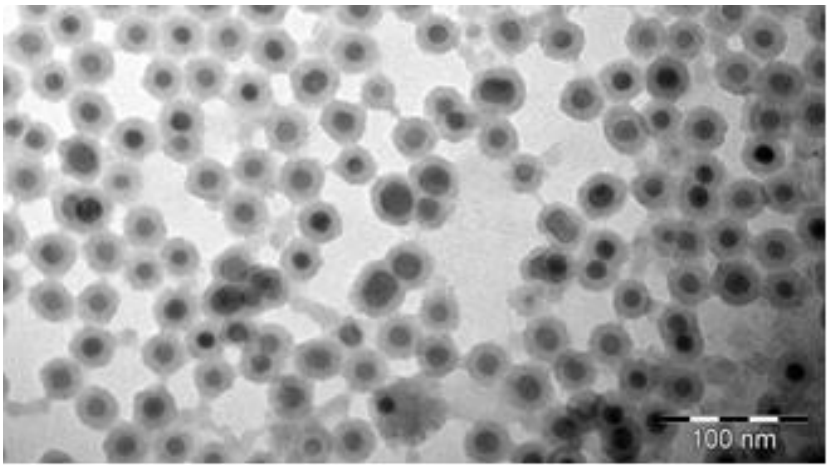

Figure 3.13: TEM image of Silica coated $NaYGdF_4$:Yb/Er UCNPs.

The presence of surface silica, as well as that of APTES, was confirmed using infrared spectroscopy (Figure 3.14). The uncoated UCNPs possess peaks at 1718 cm^{-1} and 2918 cm^{-1} which represent the C=O and CH stretches for oleic acid respectively [251]. A prominent band at around 1070 cm^{-1} represents the Si-O bend (Figure 3.14 b and c) while the NH_2 bend at 1653 cm^{-1} (Figure 3.14 c) supports the presence of surface APTES [251].

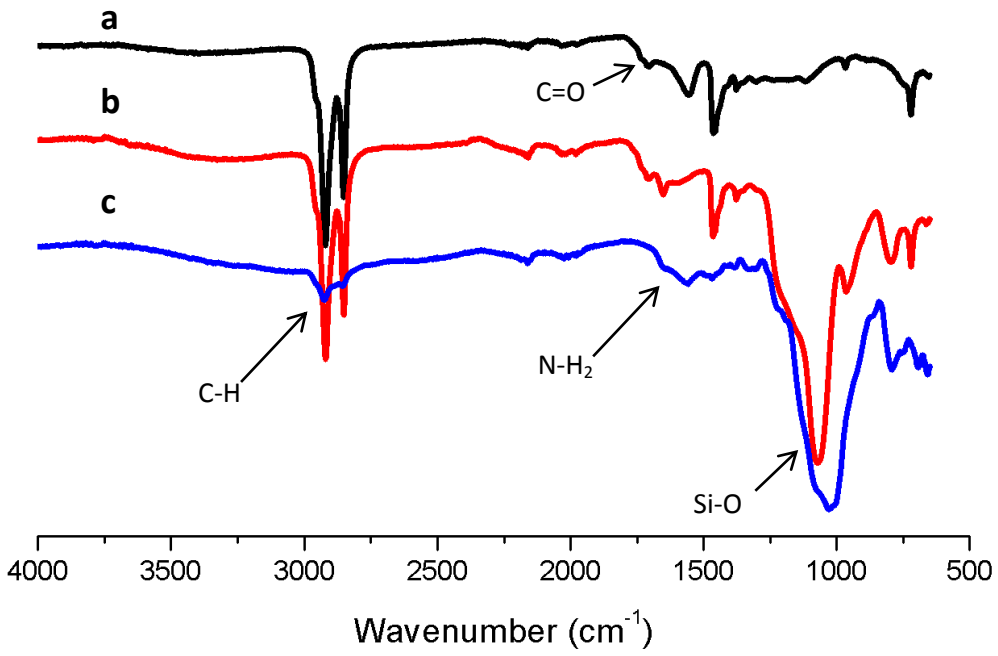

Figure 3.14: Infrared spectra of a) $NaYGdF_4$:Yb/Er, b) $NaYGdF_4$:Yb/Er@Si and c) $NaYGdF_4$:Yb/Er@Si@APTES.

Figure 3.15 shows the upconversion emission spectra for silica coated and uncoated $NaYGdF_4$:Yb/Er spherical particles. The UC emissions for the silica coated particles were obtained in DMSO. Interestingly, silica coating of the oleic acid stabilized UCNPs resulted in the simultaneous increase and decrease of the 410 nm and 840 nm emissions respectively as well as a slight increase in the red emission at 660 nm. These changes are most likely a result of the protection from the environmental quenching effects offered to the UCNP core by the silica shell where population of the higher energy states, at the expense of the lower energy states, is more efficient. An increase in fluorescence lifetimes, for both the red and green emissions, was also observed for the silica coated and APTES

functionalized nanoparticles (Table 3.4). While the green emission lifetime experienced only a slight increase of around 10 μs, that of the red emission was found to increase substantially, despite the larger error values. However, it is also possible that these changes may have been induced by the use of DMSO as a solvent. Some studies have highlighted the effect of increasing lanthanide fluorescence lifetimes upon the use of deuterated solvents which are thought to reduce multiphonon loss owing to the lower vibrational energies associated with C-D, as opposed to C-H, bonds [252]. It is possible that DMSO, which possesses fewer C-H groups than toluene, may also have contributed to a lower induction of multiphonon loss in this case, thereby increasing the lifetimes and emissions of the particles . nanoparticles (Table 3.4).

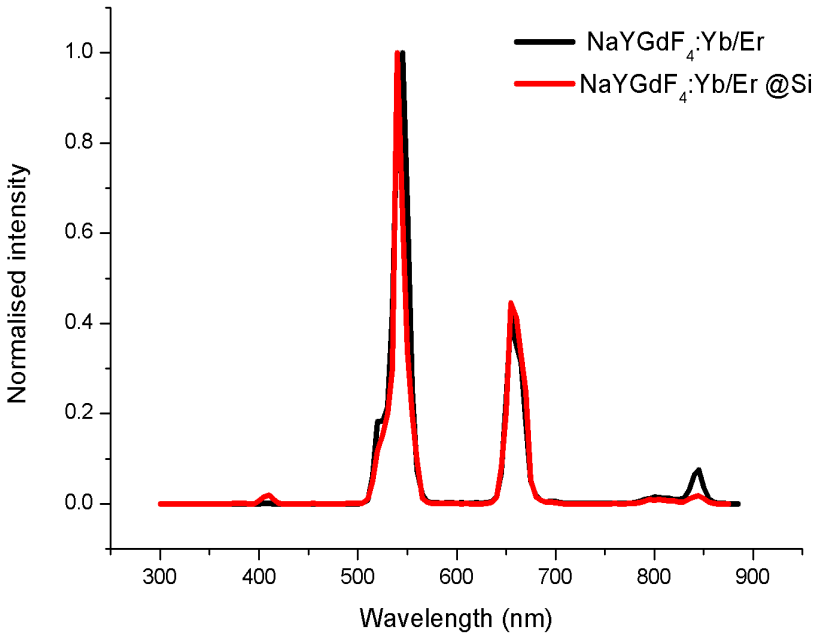

Figure 3.15: Steady state UC emission spectra of $NaYGdF_4$:Yb/Er (in toluene) and $NaYGdF_4$:Yb/Er@Si (in DMSO) UCNPs. λ_{ex} = 972 nm.

Table 3.4: UC Fluorescent lifetimes of $NaYGdF_4$:Yb/Er (toluene), $NaYGdF_4$:Yb/Er@Si (DMSO) and $NaYGdF_4$:Yb/Er@Si@APTES (DMSO) UCNPs.

	Emissions	**τ_F (ms)**	**Errors (ms)**	**χ^2**
NaYGdF4:Yb/Er	Green	0.093	± 0.001	1.005
	Red	0.183	+ 0.015 - 0.013	1.100
NaYGdF4:Yb/Er@Si	Green	0.103	± 0.002	0.974
	Red	0.309	+ 0.032 - 0.026	1.024
NaYGdF4:Yb/Er@Si@APTES	Green	0.106	± 0.004	1.071
	Red	0.240	+ 0.046 – 0.033	0.951

Chapter 4

Spectroscopic and photophysical properties of H_2Pc mixed with sphere and star shaped UCNPs

4.1 Synthesis and characterisation of un-substituted tetrathiophenoxy phthalocyanine (H_2Pc).

Un-substituted tetrathiophenoxy phthalocyanine, abbreviated here simply as H_2Pc, was synthesized via the cyclotetramerization of a 4-thiophenoxy phthalonitrile as shown in Scheme 4.1. Lithium metal was added in order to facilitate the formation of an alkoxide from pentanol, which is known to assist in ring formation. The 4-thiophenoxy phthalonitrile itself was synthesized using a substitution reaction involving thiophenol and 4-nitro phthalonitrile. The synthesis of both compounds has been reported elsewhere [224]. The structure of the H_2Pc was confirmed using mass spectrometry, FT-IR and UV-Vis spectroscopy and the Pc was found to be soluble in non-polar solvents such as toluene and cyclohexane.

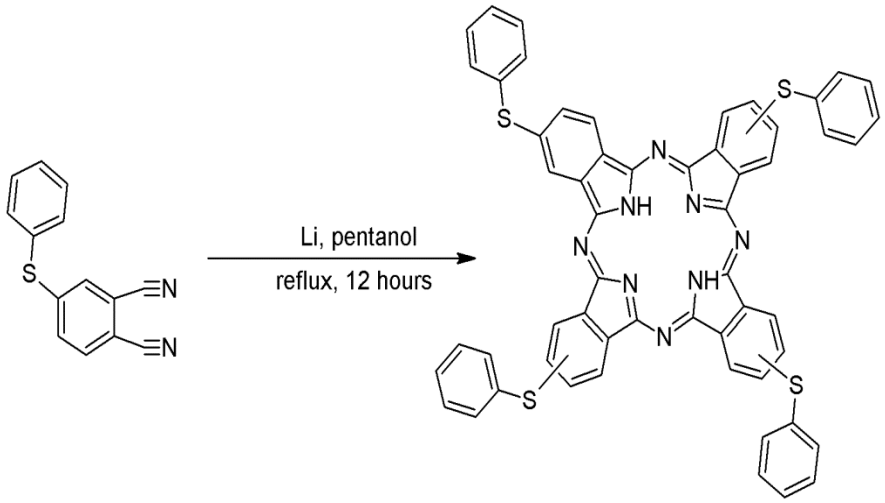

Scheme 4.1: Synthesis of tetrathiophenoxy H_2Pc from a thiophenoxy phthalonitrile precursor.

The UV-Vis spectrum obtained for the H_2Pc in toluene displayed the characteristic, lower symmetry induced, split Q band of an un-substituted phthalocyanine with Q band maxima at 681 nm and 713 nm (Figure 4.1). The excitation spectrum obtained was identical to that of the UV-Vis, indicating that no changes in molecular geometry occurred as a result of excitation, while the emission spectrum

produced a mirror image with a Q band maximum at 725 nm. The presence of one emission band originates from the relaxation of the lowest excited state only as per Kasha's rule [37].

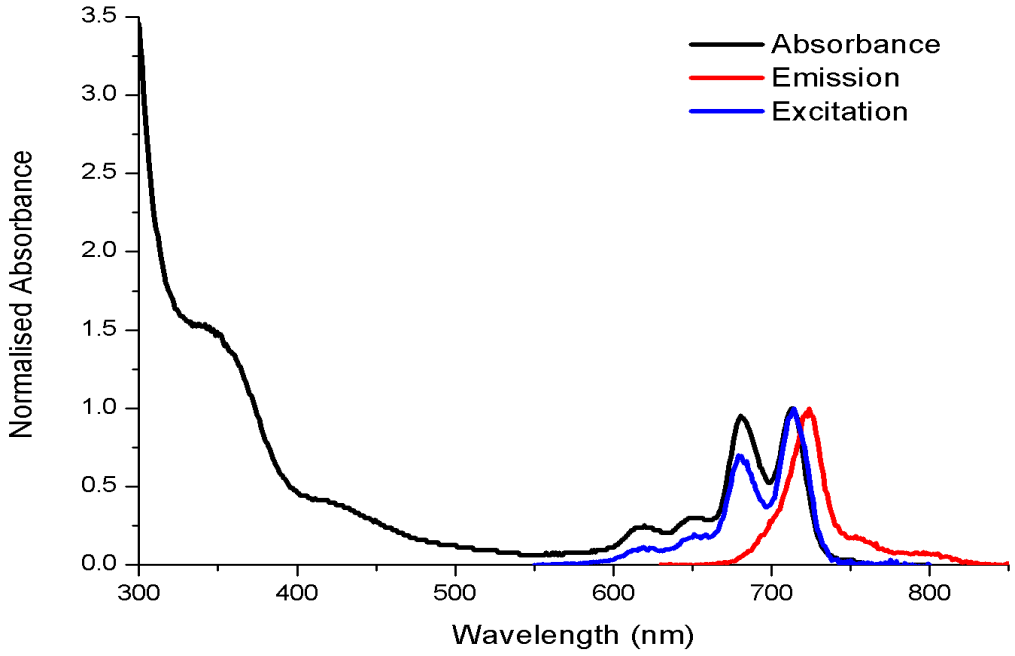

Figure 4.1: Absorption, emission and excitation spectra of tetrathiophenoxy H_2Pc in toluene.

4.2 Spectroscopic and photophysical properties of H_2Pc mixed with sphere and star shaped UCNPs.

The photophysical and spectroscopic properties of H_2Pc mixed with two sphere and two star shaped UCNPs, containing 30 mol % and 5 mol % Gd^{3+} respectively, were examined. The H_2Pc-UCNP mixtures were prepared by dissolving both Pc and UCNPs in several millilitres of toluene and allowing this solution to stir for 12 hours after which the mixture was precipitated using ethanol, collected and dried. The ratio of H_2Pc to UCNP employed was 1 mg to 50 mg respectively. The UV-Vis absorption spectrum of the mixed H_2Pc - $NaYGdF_4$:Yb/Er – sphere sample, alongside the those of the unmixed H_2Pc and UCNP sample, is shown in Figure 4.2. The spectrum of the mixture was found to possess the combined characteristics of both the UCNPs and the H_2Pc. As Yb^{3+} sensitized UCNPs

are known to absorb around 970 – 990 nm in the NIR [68], we attribute the UV-Vis spectral features for the unmixed UCNPs, displayed in Figure 4.2, to light scattering from particle dispersion. The emission and excitation spectra of the mixed sample were also obtained and are displayed in Figure 4.3. The spectroscopic and fluorescence properties of the H_2Pc mixed with the four UCNPs were found to be relatively similar and did not deviate significantly from those of the unmixed H_2Pc (Table 4.1).

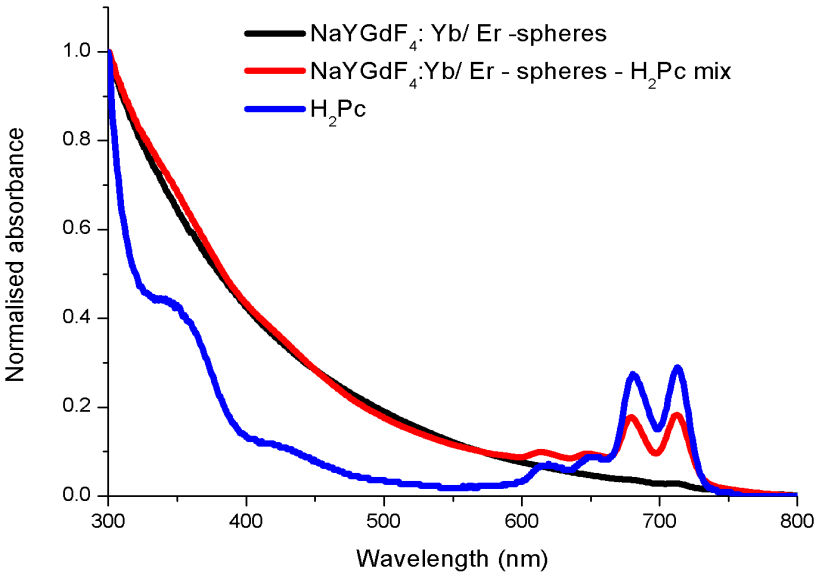

Figure 4.2: Absorbance spectra of H_2Pc, $NaYGdF_4$:Yb/Er spheres and $NaYGdF_4$:Yb/Er spheres – H_2Pc mix in toluene.

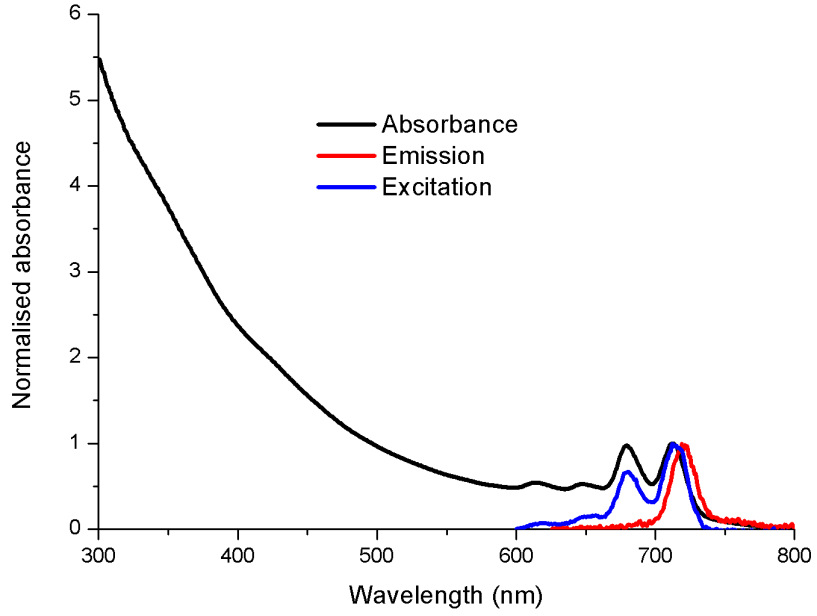

Figure 4.3: Absorbance, emission and excitation spectra of $NaYGdF_4$:Yb/Er spheres – H_2Pc mix in toluene.

Table: 4.1: Spectroscopic and fluorescence parameters of H_2Pc alone and mixed with UCNPs in toluene. Fluorescence lifetimes and fluorescence quantum yields were obtained using 672 nm and 650 nm excitation wavelengths respectively.

	Q_{abs} (nm)	Q_{ex} (nm)	Q_{em} (nm)	τ_F (ns)	χ^2	Φ_f
H_2Pc	681, 713	681, 714	724	5.23 ± 0.01	1.08	0.08
NaYGdF4:Yb/Er-Stars-H_2Pc	680, 713	682, 714	721	5.28 ± 0.01	1.31	0.03
NaYGdF4:Yb/Er-Sphere-H_2Pc	680, 713	680, 715	723	5.27 ± 0.03	1.24	0.02
NaYGdF4:Yb/Tm-Stars-H_2Pc	680, 713	679, 715	723	5.46 ± 0.01	1.15	0.04
NaYGdF4:Yb/Tm-Sphere-H_2Pc	680, 713	680, 714	724	5.25 ± 0.01	1.07	0.03

The mixing of UCNPs with dyes has been undertaken elsewhere and is thought to result in the physical adsorption of the smaller dye molecule to the larger UCNP. In one study, the physical adsorption of an organic, NIR emitting, dye to an UCNP produced a blue shift, of 6 nm, in the UV-Vis absorption peak of the dye [253]. For our mixtures, a small blue shift of 1 nm was observed for the 681 nm absorption peak of the H_2Pc and slightly larger changes were observed for the emission and excitation peak maxima of some samples (Table 4.1). As these changes are neither uniform nor large enough to be considered significant, possibly arising as a result of concentration or solubility effects, it is not possible to confirm the occurrence of physical adsorption. However, other studies examining the spectroscopic properties of un-substituted and Zn substituted Pcs conjugated to Au NPs, have also observed only slight or no changes in absorption, emission and excitation peak positions [254]. Another method used to assess the effect of mixing on the fluorescence properties of the H_2Pc was to examine the fluorescence lifetimes (Table 4.1) which were determined using a multi-exponential reconvolution fit with Equation 4.1 [255]:

$$I(t) = \int_{-\infty}^{t} IRF(t') \sum_{i=1}^{n} A_i e^{-\frac{t-t'}{\tau_i}} dt' \qquad \text{Equation 4.1}$$

where n is the number of exponential components, A_i is the amplitude of the i^{th} exponential component, τ_i is the lifetime of the i^{th} exponential component and *IRF* is the instrument response function given by a scattering sample, in this case, ludox. As the lifetimes of Pc dyes are generally in the nanosecond range [256], a reconvolution fit was undertaken in order to minimise possible

instrumental error by utilizing the instrument response function which establishes the shortest measurable lifetime for a given set of experimental parameters. All measurements were carried out in toluene using 672 nm excitation from a non-tunable pulsed laser. In all cases, the data were best fit to a single exponential component, yielding only one lifetime. Strangely, while the χ^2 values for the H_2Pc alone, as well as the Tm^{3+} doped sphere UCNP mixed sample, were acceptable, those for the remaining samples were large and attempts to fit the data to 2 and 3 exponentials did not yield better χ^2 values. Thus the τ_F values for the additional 3 mixed H_2Pc samples may be somewhat inaccurate. The mixed samples all displayed lifetime values close to those of the H_2Pc alone, though slightly larger. Again, the extent to which the larger values are representative of real physical effects is questionable for the three samples possessing the large χ^2 values. Changes in lifetime values for Pc molecules adsorbed or conjugated to NPs are thought to be influenced by the orientation of the Pc around the nanoparticle surface, and accompanying changes in dipole moments, as well as interactions with large atomic number elements, i.e. transition and lanthanide group metals, which may decrease fluorescence lifetimes as a result of a large spin orbit coupling contribution, and the subsequent enhancement of intersystem crossing, through the heavy atom effect [257, 258]. It is possible that physical adsorption to a nanoparticle surface may cause a decrease in Pc molecule collisions through stabilization and consequently result in an increase in lifetimes. Interestingly the H_2Pc mixed with the largest UCNPs, the Tm^{3+} doped stars, displayed a larger increase in lifetime than the other samples. Fluorescence quantum yields were also determined for the H_2Pc alone as well as the mixed samples, utilizing a ZnPc standard in toluene. The initial fluorescence quantum yield obtained for the H_2Pc was low and displayed small decreases upon mixing with UCNPs. It is possible that interaction with the UCNP surface, or aggregation with other Pc molecules on the surface, may have resulted in fluorescence quenching and consequently lower quantum yields. The increase in fluorescence lifetime accompanying a decrease in fluorescence quantum yield for Pcs mixed or attached to NPs has also been reported before [170].

4.3 Fluorescence properties of UCNPs mixed with H_2Pc

Steady state upconversion fluorescence of the UCNP-H_2Pc mixtures was also undertaken and normalised emissions were compared to those of the unmixed NPs. One example, the mixture containing the Er^{3+} doped sphere UCNPs, is shown in Figure 4.4. The green to red peak ratio of the mixed sample was found to increase in relation to that of the unmixed sample. This trend was also observed for the other UCNP mixed samples, including the Tm^{3+} doped particles, where an increase in the blue to red peak ratio was noted. It is possible that the decrease in red emission may arise, in part, due to the absorption of the red emission itself by the H_2Pc. However, 972 nm excitation of the mixed samples did not result in a visible emission spectrum for the H_2Pc, essentially excluding the presence of fluorescence resonance energy transfer (FRET) [259], which involves the excitation of the H_2Pc dye utilizing the emission from the UCNP in the region of highest Pc absorbance, i.e. the Q band. As the inter atomic distances between donor and acceptor systems required for efficient FRET processes are short [259], this could suggest that physical adsorption of the H_2Pc to the UCNP surface did not occur to an extent where observable FRET processes were possible. It is also likely that the UCNPs, which are known to possess relatively low quantum yields [260], may not have produced an emission with an intensity high enough to excite the H_2Pc. In general, mixing of the UCNPs with H_2Pc appeared to exert no change on the lifetime values for the different UC emissions. Deviation in the mixed UCNP lifetime values in comparison to the unmixed ones could be accounted for by the relatively large errors obtained for the support plane error analysis. Two exceptions were the red emission lifetimes for the H_2Pc mixed Tm^{3+} and Er^{3+} doped star shaped particles, where the red emission lifetimes were found to increase and decrease for the Tm^{3+} and Er^{3+} doped UCNPs respectively. It is possible that the presence of H_2Pc on or near the surface of the UCNPs could have effectuated a change in the decay lifetimes, perhaps as a result of different amounts of H_2Pc interacting with NP surfaces within the different samples. However, it is more likely, that these results originated from a bad model fitting. The unchanging lifetimes for the majority of the UCNP emissions were not unexpected, owing to the shielding of the 4f orbital energy levels within the dopant ions.

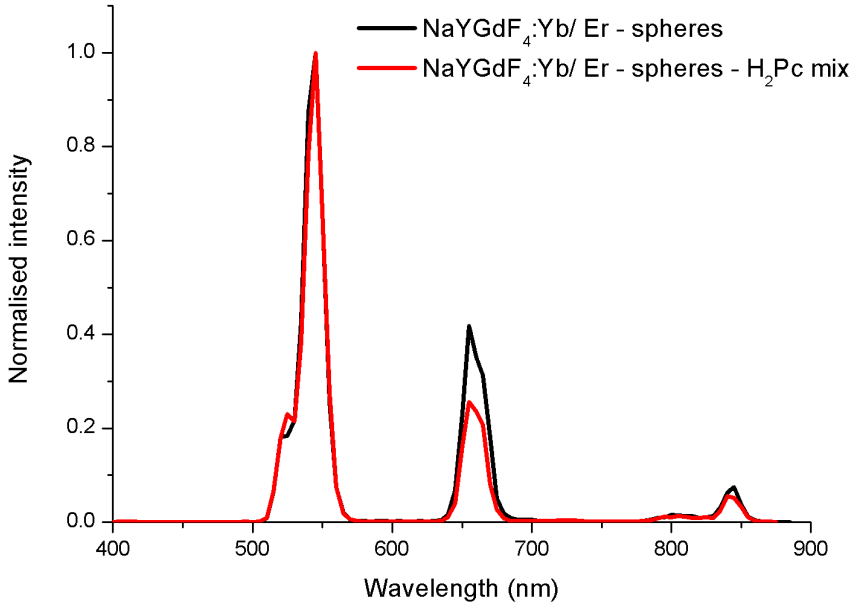

Figure 4.4: Upconversion emission spectra of $NaYGdF_4$:Yb/Er – spheres and $NaYGdF_4$:Yb/Er – spheres – H_2Pc mix in toluene. λ_{ex} = 972 nm.

Table 4.2: Fluorescence emission lifetimes of UCNPs mixed with H_2Pc in toluene.

	Emissions	τ_F (ms)	Errors (ms)	χ^2	τ_F (ms) Unmixed UCNPs
$NaYGdF_4$:Yb/Er Spheres - H_2Pc	Green	0.092	± 0.002	1.042	0.093
	Red	0.206	± 0.004	0.980	0.183
$NaYGdF_4$:Yb/Er Stars - H_2Pc	Green	0.088	± 0.002	1.075	0.082
	Red	0.204	± 0.001	1.028	0.263
$NaYGdF_4$:Yb/Tm Spheres - H_2Pc	Blue	0.547	+ 0.016 - 0.015	0.974	0.579
	Red	0.539	± 0.019	1.014	0.527
	NIR	0.845	± 0.019	0.957	0.800
$NaYGdF_4$:Yb/Tm Stars - H_2Pc	Blue	0.745	± 0.014	1.002	0.748
	Red	0.770	± 0.016	0.991	0.706
	NIR	1.22	+ 0.038 - 0.036	1.057	1.21

4.4 Singlet oxygen studies

Singlet oxygen production was examined utilizing time resolved and steady state phosphorescence spectroscopy. The $^1O_2$ time resolved spectrum is displayed as a small decay curve following the initial laser pulse. Excitation of the H_2Pc was performed utilizing a 672 nm laser. All decay curves were fitted utilizing a multi exponential tail fit model and Equation 3.1. The best fits were found using a single exponential and, subsequently, each sample was found to possess only one lifetime. The phosphorescence decay curve of $^1O_2$ produced by the H_2Pc alone in toluene is shown in Figure 4.5. In order to demonstrate that the signal observed was indeed $^1O_2$, sodium azide, a known $^1O_2$ quencher [261], was added to the solution. As sodium azide is insoluble in toluene, it was added to the H_2Pc as a solution in DMSO. As expected, the sodium azide solution reduced the $^1O_2$ decay signal to zero. The effect of adding DMSO was also examined in order to confirm that signal quenching was performed by sodium azide and not DMSO. The addition of DMSO was found to reduce the $^1O_2$ lifetime; however, it did not result in complete extinction of the decay signal. Lifetimes of $^1O_2$ produced by three of the UCNP H_2Pc mixed samples were also obtained. An example, the $^1O_2$ decay produced by the $NaYGdF_4$:Yb/Er star shaped UCNP sample, is shown in Figure 4.6. The steady state phosphorescence spectra of $^1O_2$ for the mixed and unmixed Pc samples also displayed the typical $^1O_2$ emission peak at around 1270 nm (Figure 4.7). As expected, the unmixed UCNP samples did not produce $^1O_2$. Similar results were obtained for all the UCNP H_2Pc mixed samples. The calculated $^1O_2$ lifetimes resulting from 672 nm excitation of the H_2Pc are shown in Table 4.3. The values are close to those reported in another study for $^1O_2$ production in benzene [184], a similar non-polar solvent system. A noticeable decrease was observed for the mixed samples when compared to the Pc alone. This could be a result of several possibilities, including non-radiative de-excitation and quenching initiated through collisions with the NP surface. This may explain the noticeable decrease in the $^1O_2$ lifetime associated with the smaller sphere shaped particles when compared to the larger star shaped ones, as the smaller particles possess a higher surface area to volume ratio. The presence of large amounts of paramagnetic Gd^{3+} ions, especially for the sphere shaped sample, may also have contributed to the increased quenching of $^1O_2$. This phenomenon has been recorded for some

paramagnetic transition metal ions co-ordinated to photosensitizers and is attributed to a $^1O_2$ to metal energy transfer [262, 263]. An attempt was also made to initiate the production of $^1O_2$ utilizing 972 nm excitation and energy transfer from the UCNPs to the H_2Pc; however, we were unable to obtain any signals for time resolved or steady state measurements. Again, this indicates that the FRET processes between the UCNPs and the H_2Pc are extremely inefficient or, more likely, not occurring at all. Detection of $^1O_2$ utilizing an IR detector and NIR excitation source was also found to be problematic as the NIR laser excitation resulted in a very low signal to noise detection ratio owing to the large number of dark counts produced by the NIR laser. A better technique for the confirmation of singlet oxygen production utilizing a 972 nm laser would be to observe the indirect $^1O_2$ facilitated degradation of DPBF using UV-Vis absorption [217]; however we were unable to perform this experiment owing to time constraints.

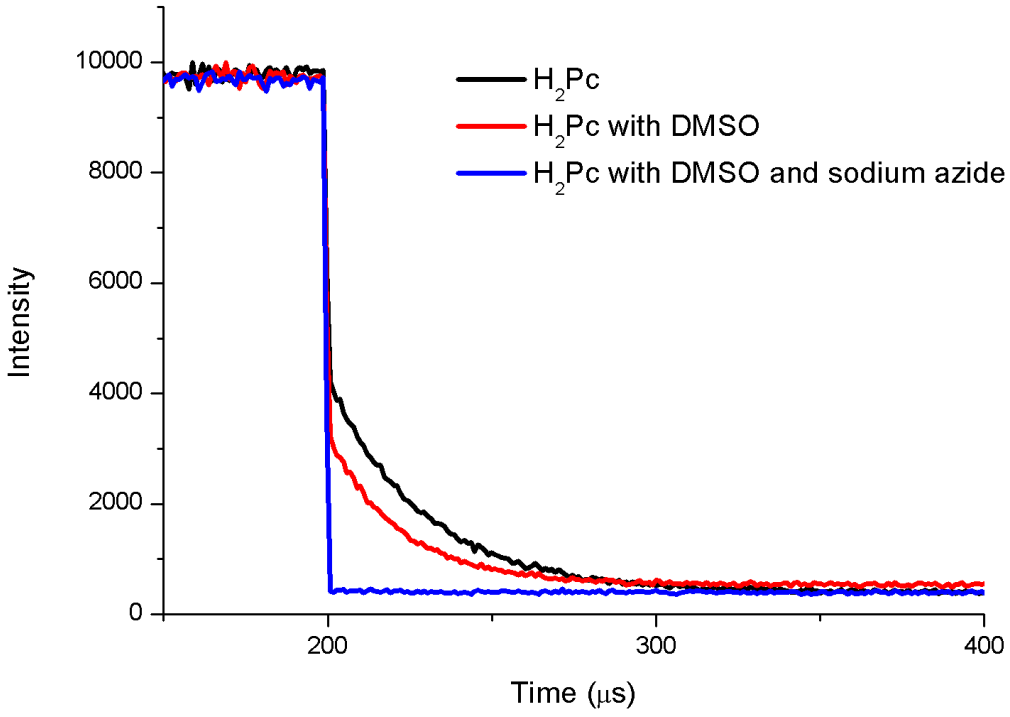

Figure 4.5: Time resolved fluorescence spectra of $^1O_2$ produced by the H_2Pc alone, the H_2Pc with DMSO and the H_2Pc with DMSO and sodium azide in toluene. Excitation of the H_2Pc was performed using a 672 nm laser and $^1O_2$ emissions were detected at 1270 nm.

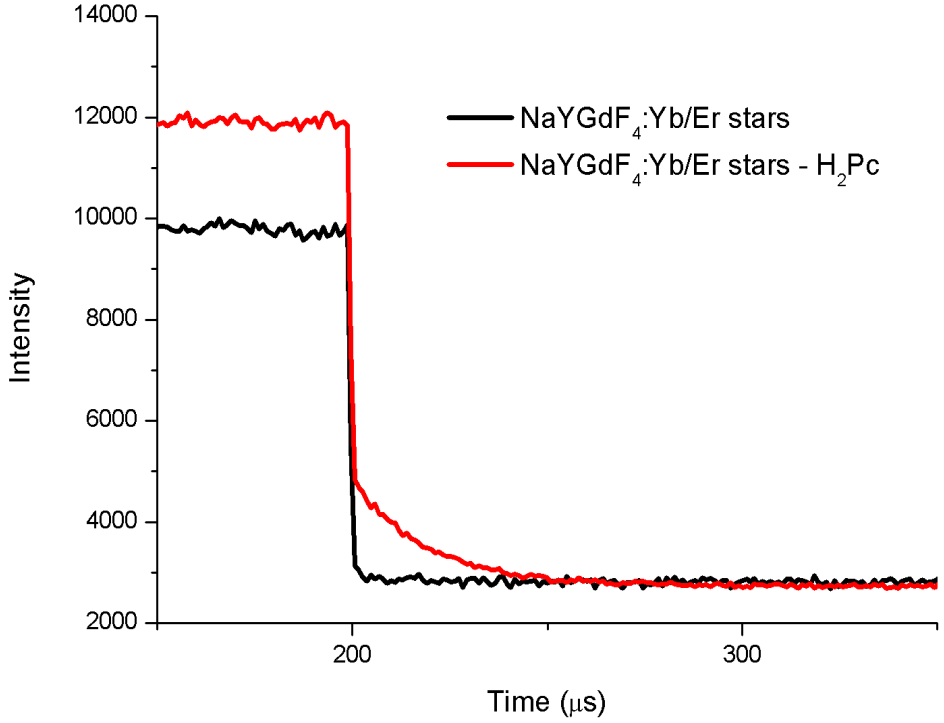

Figure 4.6: Time resolved spectra of $^1O_2$ produced by $NaYGdF_4$:Yb/Er star shaped UCNPs alone and mixed with H_2Pc in toluene. Excitation of the H_2Pc was performed using a 672 nm laser and $^1O_2$ emissions were detected at 1270 nm.

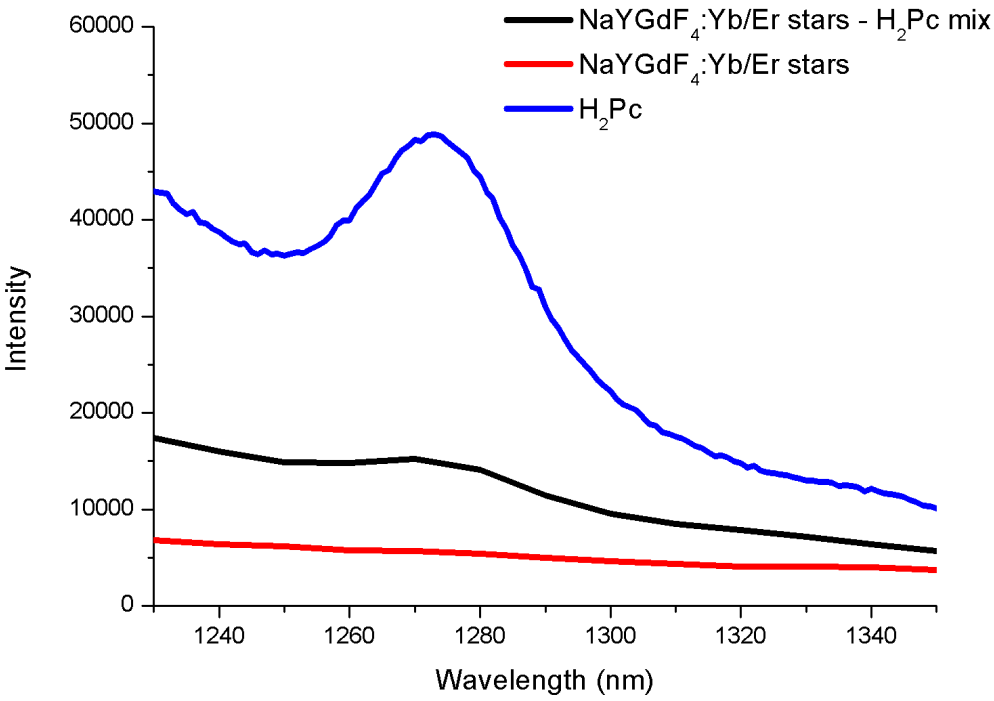

Figure 4.7: Steady state emission spectra of $^1O_2$ produced by $NaYGdF_4$:Yb/Er star shaped UCNPs, H_2Pc and H_2Pc mixed $NaYGdF_4$:Yb/Er star shaped UCNPs in toluene. Excitation of the H_2Pc was performed using a 672 nm laser and $^1O_2$ emissions were detected at 1270 nm.

Table 4.3: Singlet oxygen lifetimes produced by H_2Pc alone and mixed with UCNPs in toluene.

	τ_Δ (μs)	Errors (μs)	χ^2
H_2Pc	29.17	+ 0.42 -0.41	1.04
H_2Pc with DMSO	22.20	+ 0.37 -0.36	1.02
NaYGdF4:Yb/Tm Spheres - H_2Pc	14.55	+ 0.64 -0.62	1.03
NaYGdF4:Yb/Tm Stars - H_2Pc	19.32	+0.77 -0.74	0.86
NaYGdF4:Yb/Tm Stars - H_2Pc	19.17	+0.62 -0.60	1.06

Chapter 5

Synthesis and characterisation of an aluminium octacarboxy phthalocyanine UCNP conjugate

5.1 Synthesis of aluminium octacarboxy phthalocyanine and aluminium octacarboxy phthalocyanine – UCNP conjugate.

Chloride axially ligated aluminium octacarboxy phthalocyanine, abbreviated (Cl)AlOCPc, was synthesized from pyromellitc dianhydride, urea and $AlCl_3$ with a DBU catalyst (Scheme 5.1) [225]. The initially formed product, still containing imides, was hydrolysed using H_2SO_4 to yield eight carboxylic groups at the β positions. After purification using column chromatography with NaOH eluent, the Na salt of (Cl)AlOCPc was yielded. Successful synthesis of the (Cl)AlOCPc was confirmed using mass spectrometry, FT-IR and UV-Vis spectroscopy. Figure 5.1 shows the absorption, emission and excitation spectra of (Cl)AlOCPc in DMSO. The peak maxima, 705 nm, 705 nm and 714 nm for the absorption, excitation and emission spectra respectively, are similar to those obtained in for AlOCPcs in DMSO reported elsewhere [158].

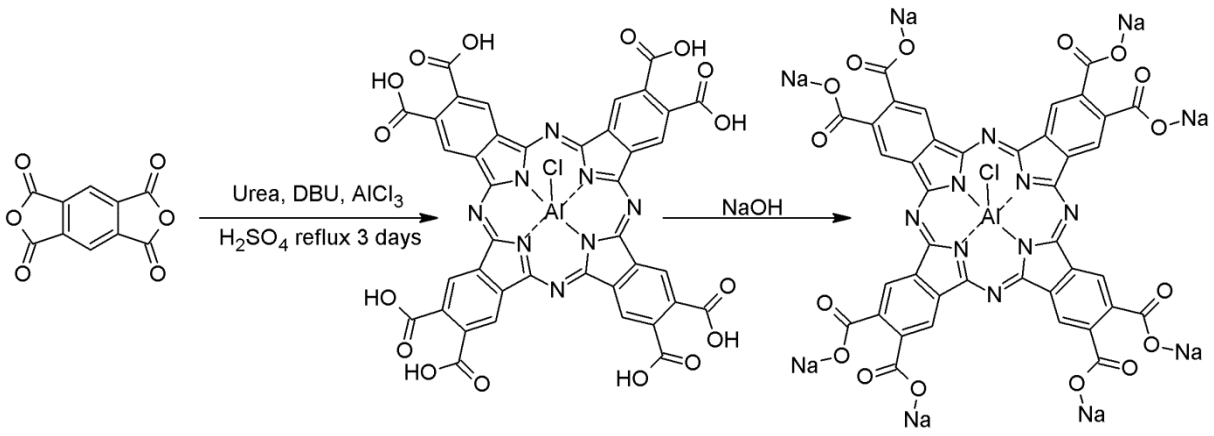

Scheme 5.1: Synthesis of (Cl)AlOCPc sodium salt from pyromellitic dianhydride, urea and $AlCl_3$.

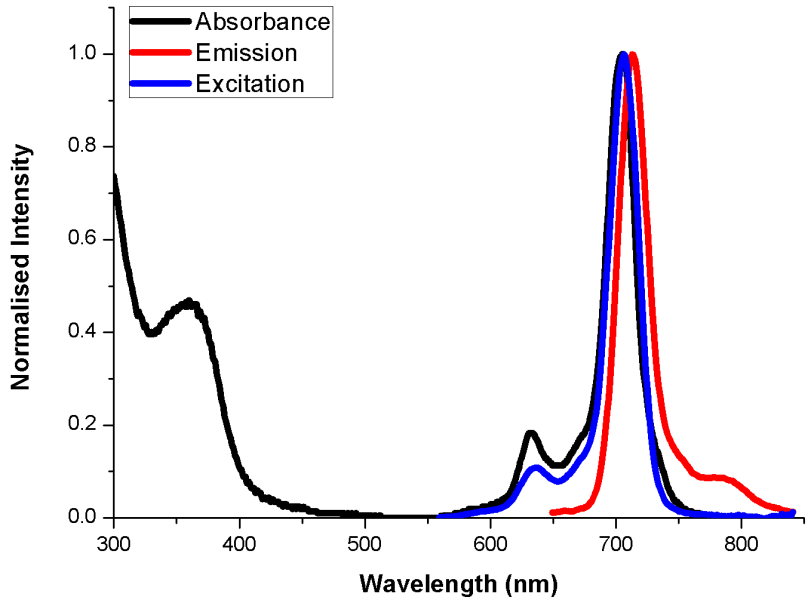

Figure 5.1: Normalised absorbance, emission and excitation spectra of (Cl)AlOCPc in DMSO.

The (Cl)AlOCPc – UCNP conjugate was synthesized by adding amino functionalized UCNPs to (Cl)AlOCPc in the presence of 1-ethyl-3-(3-dimethylaminopropyl) carbodiimde (EDC) and N-hydroxy succinimide (NHS) coupling agents (Scheme 5.2). The combined usage of EDC and NHS as coupling agents for the formation of amide bonds has been shown to be significantly more effective than the use of either species in isolation [264]. The conjugation reaction was undertaken in a phosphate buffer solution (PBS) with a pH of 7.4 in order to minimize the effects of acid/ base hydrolysis on amide bond formation. The presence of the amide bond was confirmed using FT-IR.

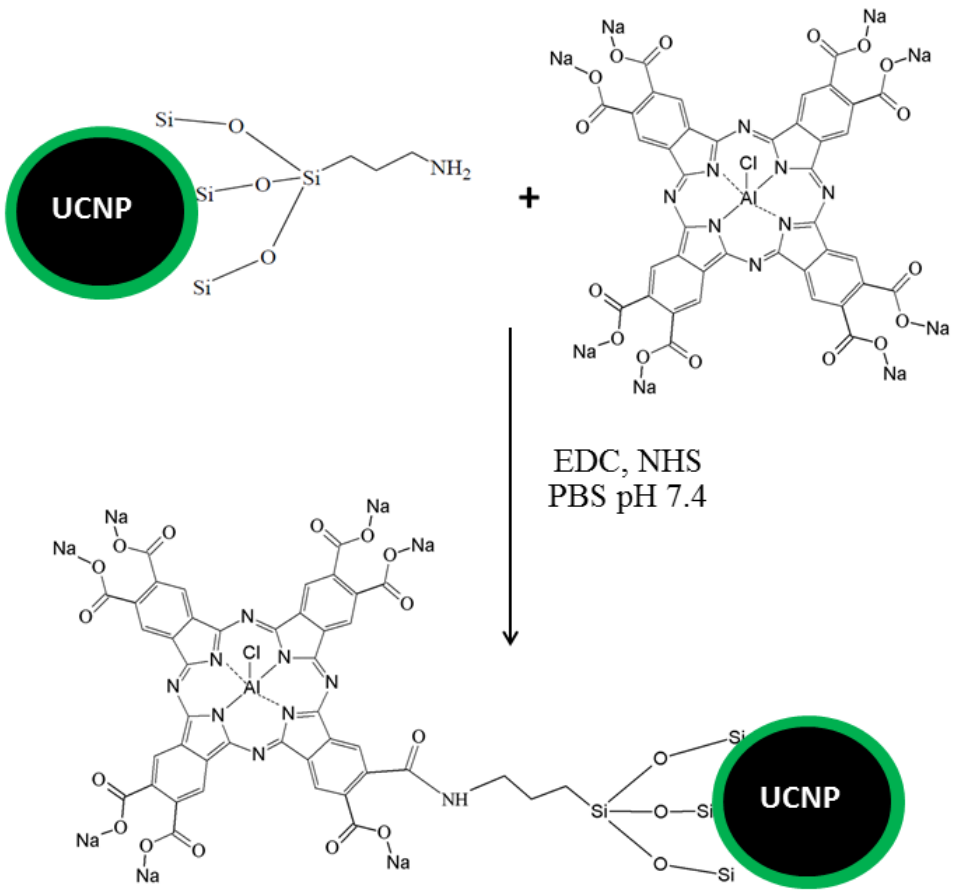

Scheme 5.2: Synthesis of (Cl)AlOCPc – UCNP conjugate.

Figure 5.2a displays the characteristic NH_2 group bends at 1561 cm^{-1} and 1468 cm^{-1} for the amino functionalized UCNPs. The carboxylic acid carbonyl group (C=O) of the (Cl)AlOCPc is also displayed at 1704 cm^{-1}. Upon conjugation, this peak was shown to disappear, being replaced by a 1640 cm^{-1} vibration representing the amide (CONH) functional group. The UCNPs selected for conjugation with (Cl)AlOCPc were the $NaYGdF_4$:Yb/Er sphere shaped particles. The functionalization of these particles with silica and APTES has been discussed in Section 3.6.

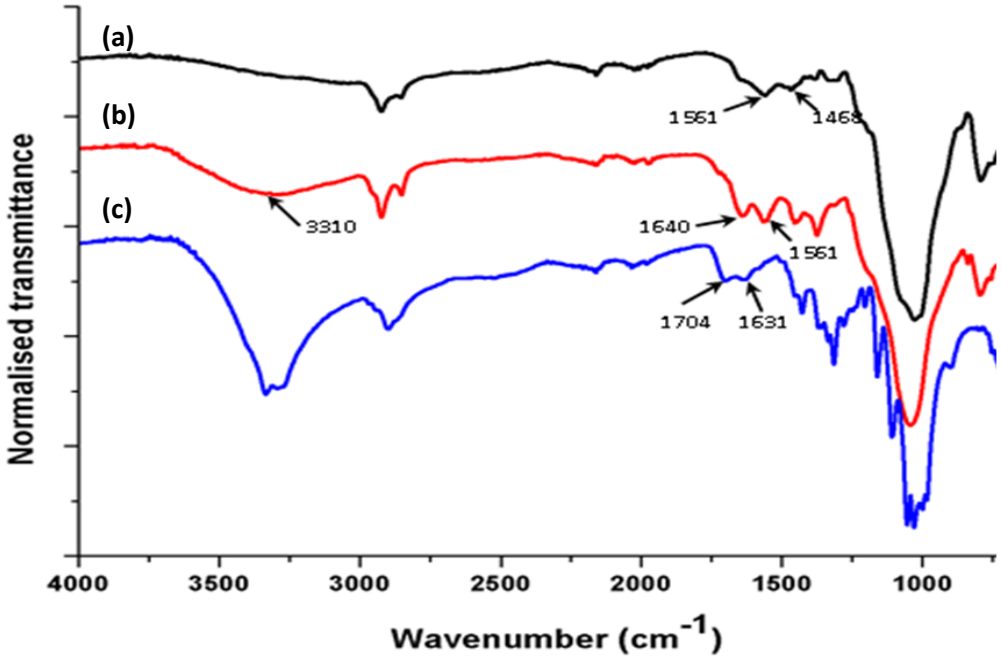

Figure 5.2: IR spectra of (a) NaYGdF4:Yb/Er@Si@APTES UCNPs, (b) (Cl)AlOCPc-UCNP conjugate and (c) (Cl)AlOCPc.

5.2 Spectroscopic and photophysical properties of (Cl)AlOCPc conjugated to silica coated UCNPs.

The UV-Vis absorption Q band of the conjugated (Cl)AlOCPc displayed a striking blue shift of 33 nm from that of the un-conjugated Pc and displayed no peak broadening (Figure 5.3). In addition, the absorption and excitation spectra of the conjugate were found to overlap, indicating that no change in molecular geometry had occurred upon excitation (Figure 5.4).

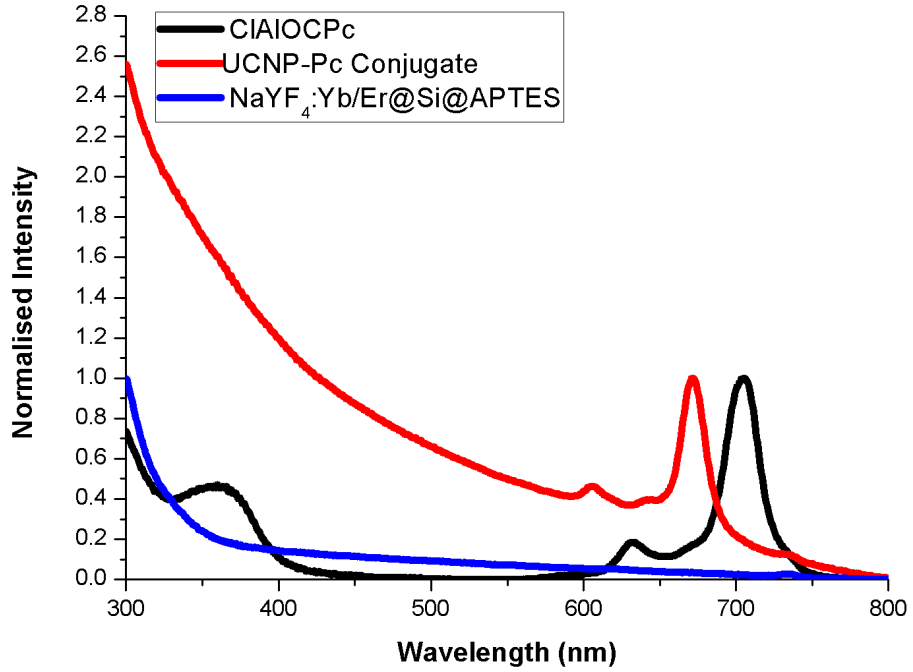

Figure 5.3: Absorbance spectra of (Cl)AlOCPc, (Cl)AlOCPc-UCNP conjugate and NaYGdF4:Yb/Er@Si@APTES UCNPs in DMSO.

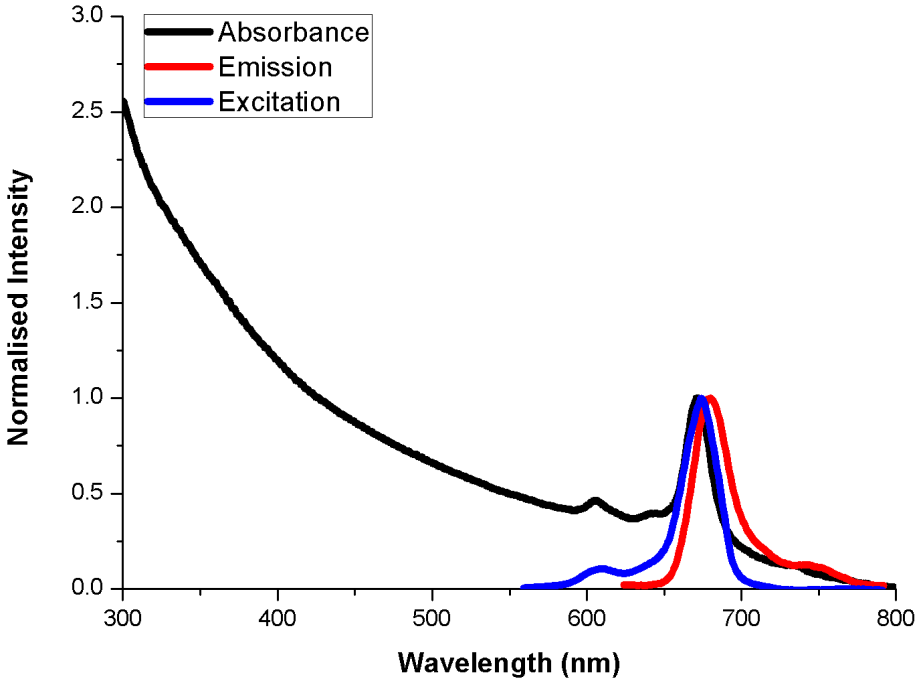

Figure 5.4: Absorbance, emission and excitation spectra of the AlOCPc-UCNP conjugate in DMSO.

Conjugation of the (Cl)AlOCPc also induced significant changes in the fluorescence lifetime whereby the presence of two lifetimes were obtained for the conjugate, one of which, the one in highest abundance, was considerably shorter (3.17 ns) than that of the unconjugated Pc (5.56 ns) (Table 5.1). A small decrease in the fluorescence quantum yield of the (Cl)AlOCPc was also observed upon conjugation (Table 5.1). A blue shift as large as 33 nm resulting from conjugation is particularly unusual and such phenomena have not been reported in most studies concerned with the photophysical properties of Pc – NP conjugates. The blue or red shifting of a Pc absorption peak can be directly related to the relative energies of the molecule's HOMO LUMO levels. As the absorption peak was found to shift to higher energies, one might assume that the energy gap separating the HOMO LUMO levels had increased. Red and blue shifting of Q band absorption peaks has been attributed to the electron withdrawing or donating properties of the Pc substituents [224]. In this case, it is possible that the UCNP effectuates a large removal of electron density from the Pc macrocycle, possibly as a result of the high concentration of electronegative F^- atoms in the UCNP core, and consequently results in a blue shift. Presumably, the extent to which the Q band undergoes a blue shift depends upon the number of conjugated substituents through which electron density may be removed. It is possible that the large blue shift reported for this sample may have arisen as a result of several of the carboxylic acid groups of the Pc conjugating to the nanoparticle surface at once, resulting in the Pc macrocycles lying flat against the UCNP surface in a perpendicular orientation. It is possible that the blue shift may have been induced by co facial aggregation of (Cl)AlOCPc on the surface of the UCNP; however, this kind of aggregation is usually associated with some degree of peak broadening as well as fluorescence quenching, both of which were not observed [175, 265]. Also, the fact that the blue shift was so large makes co facial aggregation unlikely to be the cause. The decrease in fluorescence lifetimes and quantum yields of the conjugated Pc, as opposed to the Pc alone, may have resulted from several possible phenomena. These include a heavy atom effect [258] as well as the relative orientations of the Pc and UCNP dipole moments. Studies on the photophysical properties of dye molecules linked to gold NPs have shown that dyes attached to the NP surface along their longitudinal axes experience an enhancement of their emitting dipole as a result of the constructive summation of the transition dipole and induced dipole of the dye and NP respectively which are

arranged in parallel (Figure 5.5) [257]. This emitting dipole enhancement was shown to result in increased fluorescence. In contrast, the anti-parallel arrangement of dye and NP dipole moments associated with the linkage of the dye to the NP surface in a perpendicular or transverse arrangement, i.e. along its shorter axis, was shown to cause a decrease in fluorescence (Figure 5.5) [257]. The effect of distance between the dye and NP surface was also shown to influence the amount of non-radiative energy loss where close proximity of the dye to the NP surface resulted in an increase in lifetime decay [257]. Based on these assumptions, we might assume that, in the case of this work, the (Cl)AlOCPc was closely attached to the nanoparticle surface in a perpendicular orientation. However, it should be emphasised, that the above mechanisms were elucidated for conjugations with metallic nanoparticles and the extent to which these same mechanisms operate in NPs consisting of metal salts is unknown. The presence of two lifetimes for the conjugated (Cl)AlOCPc also suggests that the Pc occupies two different local environments on the surface of the NP [266]. Again, this may involve different orientations of the Pc on the NP surface [266].

Table 5.1: Spectroscopic and fluorescence properties of (Cl)AlOCPc and the (Cl)AlOCPc-UCNP conjugate in DMSO.

	Q_{abs} (nm)	Q_{ex} (nm)	Q_{em} (nm)	τ_F (ns)	χ^2 (abundance)	Φ_f
(Cl)AlOCPc	705	705	714	5.53 ± 0.02	1.04 (100%)	0.17
NaYGdF4:Yb/Er@Si @APTES-(Cl)AlOCPc	672	674	680	3.17 ± 0.02 0.89 ± 0.03	1.04 (94%) (6%)	0.12

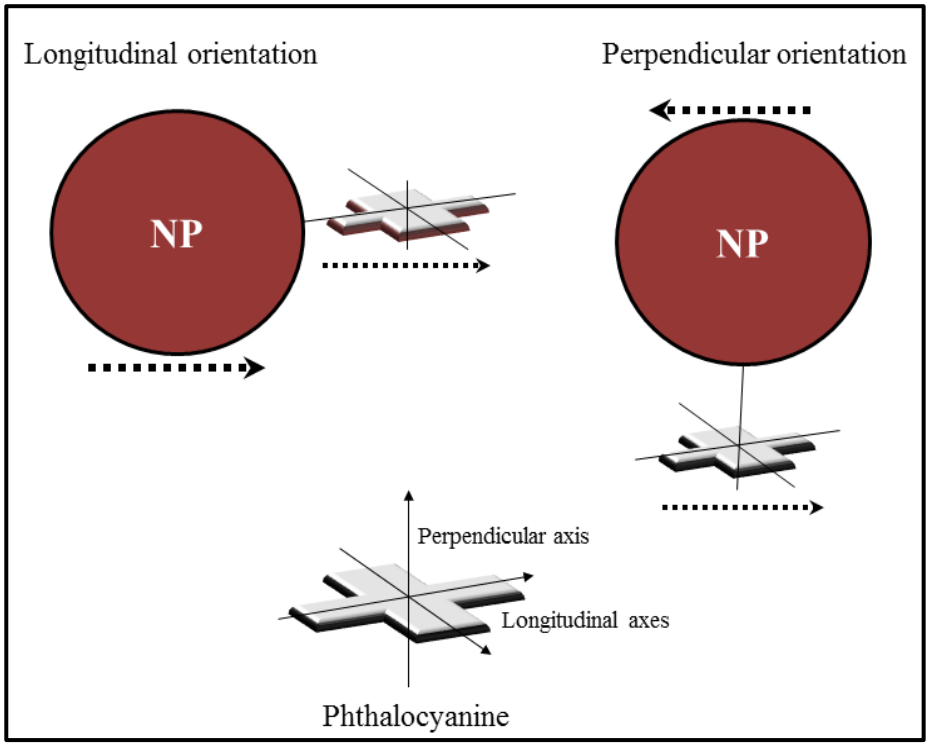

Figure 5.5: A diagrammatic representation of the longitudinal and perpendicular arrangements of dye molecules attached to NP surfaces. Transition dipole moments are represented by dotted arrows. Revised from [257].

Apart from the influence of the electromagnetic field associated with the UCNP surface, there is one other factor which might have effectuated the significant changes observed in the photophysical properties of the Pc. Although this idea is not generally dealt with in literature concerning NP conjugation reactions utilizing coupling agents, there is a slight possibility that bonding of the coupling agents to the Pc, needed to facilitate the formation on an amide bond, actually results in a new Pc with the coupling agents as substituents. This effect can be produced as a result of insufficient amounts of the amine functionalised substituent (in this case the UCNP) being unable to replace to the coupling agent bonded to the COOH group of the second substituent (the (Cl)AlOCPc). We expect that, in this case, such an event may have occurred for three reasons. Firstly, an octacarboxy Pc possesses eight potential binding sites to the NP surface, most of which, we presume are activated by bonding to the coupling agent. The possibility of all eight EDC or NHS activated COOH groups

binding to the amine groups on the NP surface is small. Thus, there is a chance that the substituents which have not reacted with the surface free amine groups, will retain the attached coupling agent. Secondly, the amine functionalization of silica surfaces utilizing amino silanes is known to be relatively inefficient [267], resulting in few free amine groups on the NP surface. Lastly, the silica coated UCNPs utilized in this work were found to be dispersible in polar solvents, such as water and DMSO; however, they possessed a tendency to settle out of suspension quickly. This may also have reduced the amount of interaction between the EDC and NHS activated COOH groups on the Pc and the amine functionalised groups on the NP surface. In order to ascertain whether the coupling agents were indeed resulting in the formation of a Pc with different substituents, we attempted to repeat the conjugation reaction without the addition of the amine functionalized UCNPs. After 15 hours, the time used for a conjugation reaction, a few millilitres of the reaction mixture in PBS pH 7.4 were removed and analysed using UV-Vis spectroscopy. The Pc Q band was not found to have shifted significantly from that of an unreacted (Cl)AlOCPc in PBS pH 7.4. The fact that the coupling agent bond to the Pc is facilitated by an ester may result in the chemical instability of possible coupling agent substituted Pcs, particularly in this case, as the synthesis was performed in aqueous media.

The results presented above were obtained for one of the initial conjugation products synthesized in this work. Unfortunately, the yields obtained for the conjugate were especially low (less than 5 mg) and we were unable to perform any UC experiments using that particular sample. The conjugate results reported above were found to be unrepeatable and subsequent attempts to synthesize the conjugate resulted in the production of samples either whose absorption peaks were so low in intensity that, even with the entire sample yield dissolved in DMSO, fluorescence studies could not be undertaken, or samples whose UV-Vis spectra showed that they were severely aggregated (Figure 5.6). Again, the severely aggregated conjugate samples did not produce visible emissions. Interestingly, however, the Q bands of many of the later made conjugate samples also displayed a blue shift (around 6 nm) when compared to that of the unconjugated Pc, though much smaller than that observed for the initial conjugate sample. From these results, we might conclude that, in general, the linking of (Cl)AlOCPc was inefficient, resulting in few covalently linked Pc molecules per UCNP and thus low absorption peak intensities. We may also conclude that the conjugation of (Cl)AlOCPc

to silica coated UCNPs generally results in a blue shifted Q band. It is possible that the extent to which the Q band is blue shifted is dependent upon the number of Pc substituents co-ordinated to the UCNP as well as orientation of the Pc molecule with respect to the UCNP samples. As these factors may vary each time a conjugate is synthesized, it stands to reason that the extent of Q band shifting may vary for each new conjugate sample.

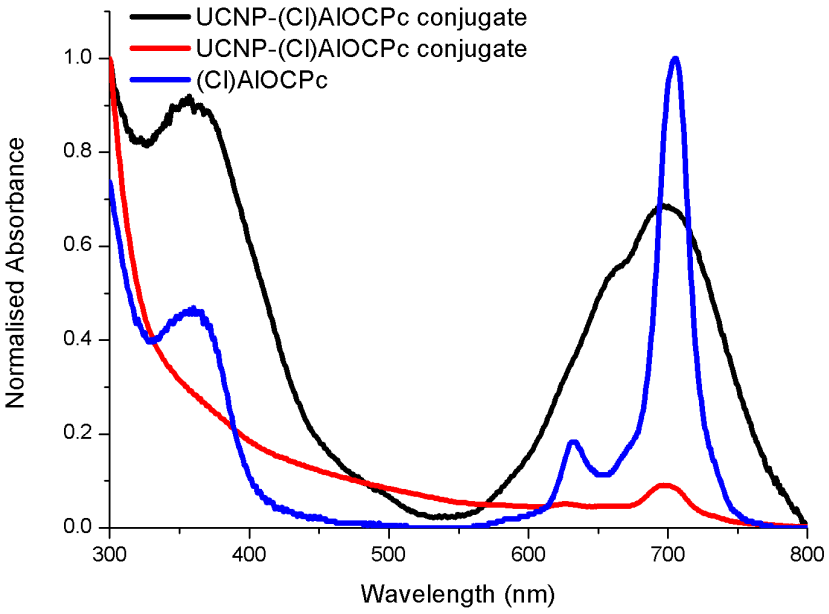

Figure 5.6: UV-Vis spectra of selected (Cl)AlOCPc – UCNP conjugates showing low absorbance and aggregation and unconjugated (Cl)AlOCPc in DMSO.

5.3 Fluorescence properties of UCNPs conjugated to (Cl)AlOCPc

In order to examine the effects of conjugation to (Cl)AlOCPc on the upconversion emissions of the silica coated UCNPs, steady state and time resolved fluorescence measurements were undertaken for the conjugate sample displaying the aggregated Q band in Figure 5.6. As for the mixed Pc and UCNP samples discussed in Chapter 4, the green to red ratio of the silica coated UCNPs increased upon conjugation to the (Cl)AlOCPc. Again, this may be a result of energy transfer processes from the UCNP to the (Cl)AlOCPc. The lifetimes of the conjugated silica coated UCNPs were found to be

similar to those of the unconjugated APTES functionalized silica coated UCNPs, indicating that UC emission lifetimes were unaffected by conjugation, presumably as a result of 4f orbital shielding and additional shielding of the metal ions by the silica shell.

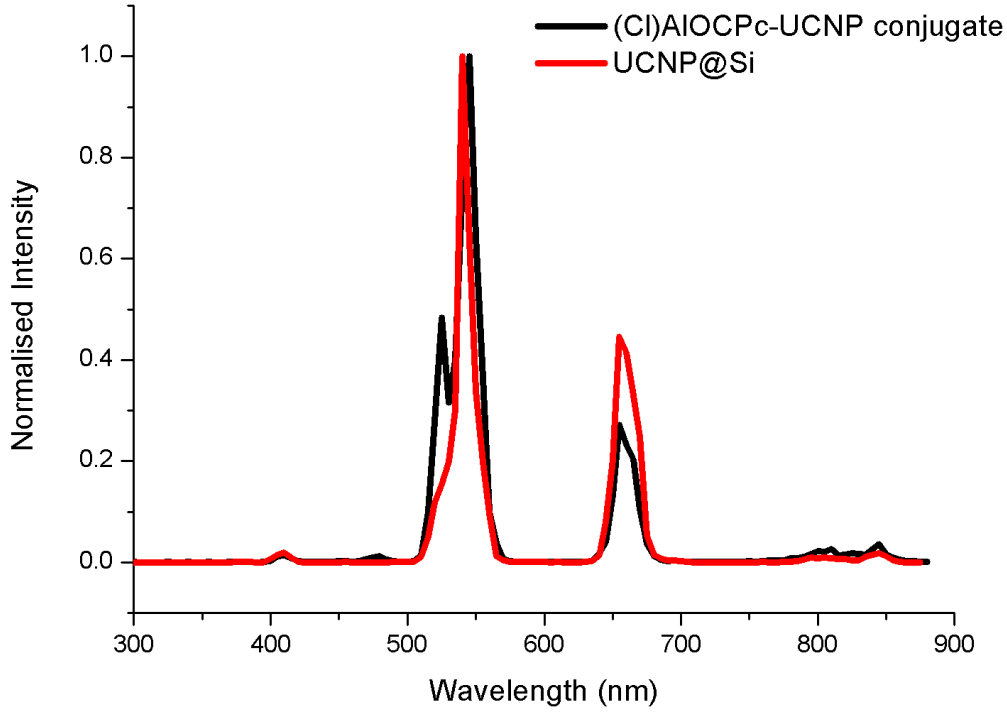

Figure 5.7: Upconversion emission spectra of UCNP@Si and the (Cl)AlOCPc-UCNP conjugate in DMSO. λ_{ex} = 972 nm.

Table 5.2: Fluorescence lifetimes of Cl)AlOCPc-UCNP conjugate and NaYGdF4:Yb/Er@Si@APTES in DMSO

	Emissions	τ_F (ms)	Errors (ms)	χ^2
(Cl)AlOCPc-UCNP conjugate	Green	0.103	± 0.002	0.940
	Red	0.222	+ 0.012 - 0.011	1.100
NaYGdF4:Yb/Er@Si@APTES	Green	0.106	± 0.004	1.071
	Red	0.240	+ 0.046 – 0.033	0.951

Chapter 6

General conclusions

6.1 General Conclusions

Sphere and star shaped $NaYGdF_4$:Yb/Er(Tm) upconversion nanoparticles were successfully synthesized using a thermal decomposition method and displayed characteristic upconversion fluorescence emissions and magnetic properties. The formation of star shaped particles was shown to be highly dependent upon the thermal decomposition temperature. EDX and powder diffraction techniques also suggested that the structural formula of the synthesized UCNPs is likely to be $NaYF_6$. $NaYGdF_4$:Yb/Er nanoparticles were also successfully coated with silica and functionalized with APTES. As expected, silica coating was shown to increase the upconversion emission lifetimes, possibly as a result of decreased surface quenching effects. The effect of mixing / conjugating with UCNPs on the spectroscopic and fluorescence properties two phthalocyanines was also examined. No significant changes in spectroscopic/ fluorescence properties were found for H_2Pc after simple mixing with UCNPs. In contrast, covalent conjugation to silica coated UCNPs was found to induce significant changes in the spectroscopic and fluorescence properties of a (Cl)AlOCPc. These changes included a 30 nm blue shift in the Q band absorption peak of the Pc, as well as the appearance of two fluorescence lifetimes, both of which were shorter than that of the unconjugated Pc. These changes are thought to be influenced by the relative orientations of the Pc and NP dipole moments and the number of Pc carboxylic groups bonded to the NP surface. The synthesis of the conjugated particles was found to be unrepeatable and suffered from low levels of Pc attachment to the UCNP surface as well as from enhanced aggregation effects. The presence of the Pc appeared to exert no change in the fluorescence lifetimes of the UCNPs, whether conjugated or mixed, most likely as a result of shielding of the excited state energy levels within the lanthanide activator ions as well as from the host matrix ions. The presence of UCNPs was also shown to result in a decrease in singlet oxygen lifetimes. Using 972 nm laser excitation, we were unable to observe any FRET processes between the UCNPs and the mixed/ conjugated Pcs. In addition, no upconversion mediated singlet oxygen generation was detected using direct steady state or time resolved measurements of the singlet oxygen NIR emission at 1270 nm. The use of direct NIR detection methods for singlet oxygen may be ineffectual, owing to dark count interference from the NIR lasing. These results seem to indicate that,

while UCNPs possess excellent fluorescent imaging capabilities, they are relatively inefficient at inducing singlet oxygen generation as a result of simple mixing with an H_2Pc.

6.2 Future considerations

Subsequent work would undoubtedly require the resolution of several speculations made regarding the composition and photophysical properties of the nanoparticles/ conjugates. Firstly, the exact elemental composition of the nanoparticles would need to be confirmed using ICP-OES. A comparison of the photophysical properties of the octacarboxylated AlPc UCNP conjugate to UCNPs conjugated to tetra- and mono-carboxylated AlPcs may be useful in elucidating the effect of the number of conjugated COOH groups per Pc macrocycle on the spectroscopic properties of the Pc. 972 nm mediated singlet oxygen generation should also be investigated utilizing a chemical method, i.e. the degradation of DPBF which is observable using UV-vis spectroscopy. A study of the photophysical and singlet oxygen generating properties of UCNPs conjugated to octacarboxy Pcs containing different central metals would be interesting as would their application in fluorescence imaging and PDT in live cell cultures.

References

[1] Feynman, R., *There's plenty of room at the bottom.* Journal of Microelectromechanical Systems, 1992. **1**(1): p. 60-66.

[2] Bhushan, B., *Introduction to nanotechnology*, in *Handbook of nanotechnology*, B. Bhushan, Editor. 2010, Springer: Heidelberg. p. 2012.

[3] Rao, C.N.R., A. Muller, and A.K. Cheetham, *Nanomaterials - an introduction*, in *The chemistry of nanomaterials: synthesis, properties and applications*, C.N.R. Rao, A. Muller, and A.K. Cheetham, Editors. 2004, Wiley-VCH Verlag GmbH & Co: Weinheim, Germany.

[4] Poole, C.P. and F.J. Owens, *Introduction to nanotechnology*. 2003, Hoboken, New Jersey: John Wiley and Sons.

[5] Alivisatos, A.P., *Semiconductor clusters, nanocrystals, and quantum dots.* Science, 1996. **271**(5251): p. 933-937.

[6] Zhang, M., M.Y. Efremov, F. Schiettekatte, E.A. Olson, A.T. Kwan, S.L. Lai, T. Wisleder, J.E. Greene, and L.H. Allen, *Size dependent melting point depression of nanostructures: nanocalorimetric measurements.* Physical Review B, 2000. **62**(15): p. 10548-10557.

[7] Bean, C.P. and J.D. Livingstone, *Superparamagnetism.* Journal of Applied Physics, 1959. **30**(4): p. 120S-129S.

[8] Thorek, D.L.J., A.K. Chen, J. Czupryna, and A. Tsoukas, *Superparamagnetic iron oxide nanoparticles for molecular imaging.* Annals of Biomedical Engineering, 2006. **34**(1): p. 23-38.

[9] Novoselov, K.S., A.K. Geim, S.V. Morozov, D. Jiang, Y. Zhang, S.V. Dubonos, I.V. Grigorieva, and A.A. Firsov, *Electric field effect in atomically thin carbon films.* Science, 2004. **306**(5696): p. 666-669.

[10] Klar, T., M. Perner, S. Grosse, G.v. Plessen, W. Spirkl, and J. Feldman, *Surface-plasmon resonances in single metallic nanoparticles.* Physical Review Letters, 1998. **80**(19): p. 4249-4252.

[11] Yang, Y., S. Matsubara, M. Nogami, J. Shi, and W. Huang, *One-dimensional self-assembly of gold nanoparticles for tunable surface plasmon resonance properties.* Nanotechnology, 2006. **17**(11): p. 2821-2827.

[12] Kelly, K.L., E. Coronado, L.L. Zhao, and G.C. Schatz, *The optical properties of metal nanoparticles: the influence of size, shape, and dielectric moment.* Journal of Physical Chemistry B, 2003. **107**(3): p. 668-677.

[13] Karkare, M., *Nanotechnology: fundamentals and applications*. 2008, New Delhi: I.K. International.

[14] Hou, Y., Z. Xu, and S. Sun, *Controlled synthesis and chemical conversions of FeO nanoparticles.* Angewandte Chemie International Edition, 2007. **46**: p. 6329-6332.

[15] Meulenkamp, E.A., *Synthesis and growth of ZnO nanoparticles.* Journal of Physical Chemistry B, 1998. **102**(29): p. 5566-5572.

[16] Lu, Q., F. Gao, and D. Zhao, *One-step synthesis and assembly of copper sulfide nanoparticles to nanowires, nanotubes, and nanovesicles by a simple organic amine-assisted hydrothermal process.* Nano Letters, 2002. **2**(7): p. 725-728.

[17] Lemyre, J.-L. and A.M. Ritcey, *Synthesis of lanthanide fluoride nanoparticles of varying shape and size.* Chemical Materials, 2005. **17**(11): p. 3040-3043.

[18] Ahmadi, T.S., Z.L. Wang, T.C. Green, A. Henglein, and M.A. El-Sayad, *Shape-controlled synthesis of colloidal platinum nanoparticles.* Science, 1996. **272**(5270): p. 1924-1926.

[19] Daniel, M.-C. and D. Astruc, *Gold nanoparticles: assembly, supramolecular chemistry, quantum-size-related properties, and applications toward biology, catalysis, and nanotechnology.* Chemical Reviews, 2004. **104**(1): p. 293-346.

[20] Ajayan, P.M., *Nanotubes from carbon.* Chemical Reviews, 1999. **99**(7): p. 1787-1799.

[21] Pickering, A.L., C. Mitterbauer, N.D. Browning, S.M. Kauzlarich, and P.P. Power, *Room temperature synthesis of surface-functionalised boron nanoparticles.* Chemical Communications, 2007: p. 580-582.

[22] Skwarczynski, M., M. Zaman, C.N. Urbani, I.-C. Lin, Z. Jia, M.R. Batzloff, M.F. Good, M.J. Monteiro, and I. Toth, *Polyacrylate dendrimer nanoparticles: a self-adjuvanting vaccine delivery system.* Angewandte Chemie International Edition, 2010. **49**(33): p. 5742-5745.

[23] Rao, J.P. and K.E. Geckler, *Polymer nanoparticles: preparation techniques and size-controls parameters.* Progress in Polymer Science, 2011. **36**(7): p. 887-913.

[24] Niemeyer, C.M., *Self-assembled nanostructures based on DNA: towards the development of nanobiotechnology.* Current Opinion in Chemical Biology, 2000. **4**(6): p. 609-618.

[25] Law, M., L.E. Greene, J.C. Johnson, R. Saykally, and P. Yang, *Nanowire dye-sensitized solar cells.* Nature, 2005. **4**: p. 455-459.

[26] Zahmakiran, M. and S. Ozkar, *Transition metal nanoparticles in catalysis for the hydrogen generation from the hydrolysis of ammonia-borane.* Topics in Catalysis, 2013. **56**: p. 1171-1183.

[27] Yan, W., H.-L. Lien, B.E. Koel, and W. Zhang, *Iron nanoparticles for environmental clean-up: recent developments and future outlook.* Environmental Science: Processes and Impacts, 2013. **15**: p. 62-77.

[28] Terris, B.D. and T. Thomson, *Nanofabricated and self-assembled magnetic structures as data storage media.* Journal of Physics D: Applied Physics, 2005. **38**(12): p. R199-R222.

[29] Berman, G.P., G.D. Doolen, and V.I. Tsifrinovich, *Solid-state quantum computation—a new direction for nanotechnology.* Superlattices and Microstructures, 2000. **27**(2-3): p. 89-104.

[30] Zhang, L., F.X. Gu, J.M. Chan, A.Z. Wang, R.S. Langer, and O.C. Farokhzad, *Nanoparticles in medicine: therapeutic applications and developments.* Clinical Pharmacology and Therapeutics, 2008. **83**(5): p. 761-769.

[31] Fang, J., H. Nakamura, and H. Maeda, *The EPR effect: unique features of tumor blood vessels for drug delivery, factors involved, and limitations and augmentation of the effect.* Advanced Drug Delivery Reviews, 2011. **63**(3): p. 136-151.

[32] Gao, W., C.-M.J. Hu, R.H. Fang, B.T. Luk, J. Su, and L. Zhang, *Surface functionalization of gold nanoparticles with red blood cell membranes.* Advanced Materials, 2013. **25**(26): p. 3549-3553.

[33] Liu, Q., B. Guo, Z. Rao, B. Zhang, and J.R. Gong, *Strong two-photon-induced fluorescence from photostable, biocompatible nitrogen-doped graphene quantum dots for cellular and deep-tissue imaging.* Nano Letters, 2013. **13**(6): p. 2436-2441.

[34] Gao, X., Y. Cui, R.M. Levenson, L.W.K. Chung, and S. Nie, *In vivo cancer targeting and imaging with semiconductor quantum dots.* Nature, 2004. **22**: p. 969-976.

[35] Li, H., Y. Zhang, L. Wang, J. Tian, and X. Sun, *Nucleic acid detection using carbon nanoparticles as a fluorescent sensing platform.* Chemical Communications, 2011. **47**: p. 961-963.

[36] Braslavsky, S.E., *Glossary of terms used in photochemistry 3rd edition (IUPAC reccomendations 2006).* Pure and Applied Chemistry, 2007. **79**(3): p. 293-465.

[37] Lakowicz, J.R., *Principles of fluorescence spectroscopy*. 3rd ed. 2006, New York: Springer.

[38] Valeur, B., *Molecular fluorescence: Principles and Applications*. 2002, Weinheim, Germany: Wiley-VCH.

[39] Jaffe, H.H. and A.L. Miller, *The fates of electronic excitation energy.* Journal of Chemical Education, 1966. **43**(9): p. 469-473.

[40] Valeur, B. and M.N. Berberan-Santos, *A brief history of fluorescence and phosphorescence before the emergence of quantum theory.* Journal of Chemical Education, 2011. **88**: p. 731-738.

[41] Kasha, M., *Characterization of electronic transitions in complex molecules.* Discussions of the Faraday Society, 1950. **9**: p. 14-19.

[42] Fery-Forgues, S. and D. Lavabre, *Are fluorescence quantum yields so tricky to measure? A demonstration using familiar stationery products.* Journal of Chemical Education, 1999. **76**(9): p. 1260-1264.

[43] Demas, J.N. and G.A. Crosby, *The measurement of photoluminescence quantum yields. A review.* Journal of Physical Chemistry, 1971. **75**(8): p. 991-1024.

[44] Porres, L., A. Holland, L.-O. Palsson, A.P. Monkman, C. Kemp, and A. Beeby, *Absolute measurements of photoluminescence quantum yields of solutions using an integrating sphere.* Journal of Fluorescence, 2006. **16**(2): p. 267-272.

[45] Olmsted, J., *Calorimetric determinations of absolute fluorescence quantum yields.* Journal of Physical Chemistry 1979. **83**(20): p. 2581-2584.

[46] McGown, L.B. and K. Nithipatikom, *Molecular fluorescence and phosphorescence.* Applied Spectroscopy Reviews, 2000. **35**(4): p. 353-393.

[47] Berezin, M.Y. and S. Achilefu, *Fluorescence lifetime measurements and biological imaging.* Chemical Reviews, 2012. **110**(5): p. 2641-2684.

[48] Birch, D.J.S. and R.E. Imhof, *Time-domain fluorescence spectroscopy using time-correlated single-photon counting*, in *Topics in Fluorescence Spectroscopy*, J.R. Lackowicz, Editor. 1999, Kluwer Academic Publishers: New York. p. 1-96.

[49] Tkachenko, N.V., *Optical Spectroscopy: Methods and Instrumentations*. 2006, Amsterdam: Elsevier.

[50] DeLuca, J.A., *An introduction to luminescence in inorganic solids.* Journal of Chemical Education, 1980. **57**(8): p. 541-545.

[51] Ronda, C.R., *Emission and excitation mechanisms of phosphors*, in *Luminescence: from theory to applications*, C.R. Ronda, Editor. 2008, Wiley-VHC: Weinheim, Germany. p. 1-60.

[52] Nara, S. and S. Ibuki, *Electronic states and optical transitions of solid crystals*, in *Fundamentals of Phosphors*, W.M. Yen, S. Shionoya, and H. Yamato, Editors. 2006, CRC Press: Florida. p. 11 - 24.

[53] Bunzli, J.-C.G., S. Comby, A.-S. Chauvin, and C.D.B. Vandevyer, *New opportunites for lanthanide luminescence.* Journal of Rare Earths, 2007. **25**: p. 257-274.

[54] Bunzli, J.-C.G. and S.V. Eliseeva, *Basics of lanthanide photophysics*, in *Lanthanide Luminescence: Photophysical, Analytical and Biological Aspects*, P. Hanninen and H. Harma, Editors, Springer: Heidelberg. p. 1-46.

[55] Ronda, C.R., T. Justel, and H. Nikol, *Rare earth phosphors: fundamentals and applications.* Journal of Alloys and Compounds, 1998. **275-277**: p. 669-676.

[56] Dorenbos, P., *Lanthanide level locations and its impact on phosphor performance*, in *Fundamentals of Phosphors*, W.M. Yen, S. Shionoya, and H. Yamato, Editors. 2006, CRC Press: Florida. p. 129-143.

[57] Auzel, F., *Upconversion and Anti-Stokes Processes with f and d Ions in Solids.* Chemical Reviews, 2004. **104**(1): p. 139-173.

[58] Suijver, J.F., *Upconversion phosphors*, in *Luminescence: from theory to applications*, C.R. Ronda, Editor. 2008, Wiley-VCH Weinheim, Germany: p. 133-190.

[59] McNaught, D. and A. Wilkinson, eds. *IUPAC Commpendium of Chemical Terminology*. 2nd ed. 1997, Blackwell Scientific: Oxford.

[60] Kaiser, W. and C.G.B. Garret, *Two-photon excitation in $CaF_2:Eu^{2+}$*. Physical Review Letters, 1961. **7**: p. 229-231.

[61] Axe, J.D., *Two photon processes in complex atoms.* Physics Review, 1964. **136**: p. 42-45.

[62] Franken, P.A., A.E. Hill, C.W. Peters, and G. Weinrich, *Generation of optical harmonics.* Physical Review Letters, 1961. **7**: p. 118-119.

[63] Diaspro, A., G. Chirico, and M. Collini, *Two-photon fluorescence excitation and related techniques in biological microscopy.* Quarterly Reviews of Biophysics, 2005. **38**(2): p. 97-166.

[64] Auzel, F., *Upconversion processes in coupled ion systems.* Journal of Luminescence, 1990. **45**: p. 341-345.

[65] Wang, F. and X. Liu, *Recent advances in the chemistry of lanthanide-doped upconversion nanocrystals.* Chemical Society Reviews, 2009. **38**: p. 976-989.

[66] Haase, M. and H. Schafer, *Upconverting Nanoparticles.* Angewandte Chemie International Edition, 2011. **50**(26): p. 5808-5829.

[67] Dijk, J.M.F.v. and M.F.H. Schuurmans, *On the nonradiative and radiative decay rates and a modified exponential energy gap law for 4f–4f transitions in rare-earth ions.* Journal of Chemical Physics, 1983. **78**(9): p. 5317-5323.

[68] Suyver, J.F., J. Grimm, M.K.v. Veen, D. Biner, K.W. Kramer, and H.U. Gudel, *Upconversion spectroscopy and properties of $NaYF_4$ doped with Er^{3+}, Tm^{3+} and/ or Yb^{3+}*. Journal of Luminescence, 2006. **117**: p. 1-12.

[69] Suyver, J.F., A. Aebischer, D. Biner, P. Gerner, J. Grimm, S. Heer, K.W. Kramer, C. Reinhard, and H.U. Gudel, *Novel materials doped with trivalnt lanthanides and transition metal ions showing near infrared to visible photon upconversion.* Optical Materials, 2005. **27**: p. 1111-1130.

[70] Walsh, B., *Judd-Ofelt theory: principles and practies*, in *Advances in Spectroscopy for Lasers and Sensing*, B.D. Bartolo and O. Forte, Editors. 2005, Springer: Dordrecht, The Netherlands. p. 403-433.

[71] Kaminskii, A., *Crystalline lasers: physical processes and operating schemes*. 1996, Boca Raton Florida: CRC Press.

[72] Wang, F. and X. Liu, *Upconversion multicolor fine-tuning: visible to near-infrared emission from lanthanide-doped $NaYF_4$ nanoparticles.* Journal of the American Chemical Society, 2008. **130**(17): p. 5642-5643.

[73] Patra, A., C.S. Friend, R. Kapoor, and P.N. Prasad, *Upconversion in Er^{3+}:ZrO_2 Nanocrystals.* Journal of Physical Chemistry C, 2002. **106**(8): p. 1909-1912.

[74] Patra, A., C.S. Friend, R. Kapoor, and P.N.Prasad, *Fluorescence upconversion properties of Er^{3+} doped TiO_2 and $BaTiO_3$ nanocrystallites.* Chemical Materials, 2003. **15**(19): p. 3650-3655.

[75] Heer, S., O. Lehmann, M. Haase, and H. Gudel, *Blue, green and red upconversion emission from lanthanide-doped $LuPO_4$ and $YbPO_4$ nanocrystals in a transparent colloidal solution.* Angewandte Chemie International Edition, 2003. **42**(27): p. 3179-3182.

[76] Luo, X. and W. Cao, *Ethanol assistant solution combustion method to prepare La_2O_2S:Yb,Pr nanometer phosphor.* Journal of Alloys and Compounds, 2008. **460**(1-2): p. 529-534.

[77] Liu, C. and D. Chen, *Controlled synthesis of hexagon shaped lanthanide-doped LaF_3 nanoplates with multicolor upconversion fluorescence.* Journal of Materials Chemistry, 2007. **17**: p. 3875-3880.

[78] Tsujiuchi, K., A. Okada, D. Matsuura, and K.Soga, *Development of flexible and transparent upconversion display by using polymer-ceramics composite*. Journal of Photopolymer Science and Technology, 2009. **22**: p. 541-546.

[79] Li, C., Z. Quan, P. Yang, S. Huang, H. Lian, and J. Lin, *Shape-controllable synthesis and upconversion properties of lutetium fluoride (doped with Yb^{3+}/Er^{3+}) microcrystals by hydrothermal process.* Journal of Physical Chemistry C, 2008. **112**(35): p. 13395-13404.

[80] Sivakumar, S., P.R. Diamente, and F.C.J.M.V. Veggel, *Silica-coated Ln^{3+} doped LaF_3 nanoparticles as robust down- and upconverting biolabels.* Chemistry - A European Journal, 2006. **12**(22): p. 5878-5884.

[81] Li, C., Z. Quan, P. Yang, J. Yang, H. Lian, and J. Lin, *Shape controllable synthesis and upconversion properties of $NaYbF_4$/$NaYbF_4$:Er^{3+} and YbF_3/YbF_3:Er^{3+} microstructures.* Journal of Materials Chemistry, 2008. **18**: p. 1353-1361.

[82] Thoma, R.E., H. Insley, and G.M. Herbert, *The sodium fluoride-lanthanide trifluoride systems.* Inorganic Chemistry, 1966. **7**(5): p. 1222-1229.

[83] Wang, M., G. Abbineni, A. Clevenger, C. Mao, and S. Xu, *Upconversion nanoparticles: synthesis, surface modification and biological applications.* Nanomedicine: Nanotechnology, Biology, and Medicine, 2011. **7**: p. 710-729.

[84] Wang, L. and Y. Li, *Controlled synthesis and luminescence of lanthanide doped $NaYF_4$ nanocrystals.* Chemical Materials, 2007. **19**: p. 727-734.

[85] Wang, F., Y. Han, C.S. Lim, Y. Lu, J. Wang, J. Xu, H. Chen, C. Zhang, M. Hong, and X. Liu, *Simultaneous phase and size control of upconversion nanocrystals through lanthanide doping.* Nature, 2010. **463**: p. 1061-1065.

[86] Mai, H.-X., Y.-W. Zheng, R. Si, Z.-G. Yan, L.-D. Sun, L.-P. You, and C.-H. Yan, *High-quality sodium rare-earth fluoride nanocrystals: controlled synthesis and optical properties.* Journal of the American Chemical Society, 2006. **128**(19): p. 6426–6436.

[87] Zhang, Y.-W., X. Sun, R. Si, L.-P. You, and C.-H. Yan, *Single-crystalline and monodisperse LaF_3 triangular nanoplates from a single-source precursor.* Journal of the American Chemical Society, 2005. **127**(10): p. 3260–3261.

[88] Zeng, J.-H., J. Su, Z.-H. Li, R.-X. Yan, and Y.-D. Li, *Synthesis and upconversion luminescence of hexagonal-phase $NaYF_4$:Yb, Er^{3+} phosphors of controlled size and morphology.* Advanced Materials, 2005. **17**(17): p. 2119-2123.

[89] Heer, S., K. Kompe, H.-U. Gudel, and M. Haase, *Highly efficient multicolour upconversion emission in transparent colloids of lanthanide-doped $NaYF_4$ nanocrystals.* Advanced Materials, 2004. **16**(23-24): p. 2102-2105.

[90] Zhang, F., J. Li, J. Shan, L. Xu, and D. Zhao, *Shape, size, and phase-controlled rare-earth fluoride nanocrystals with optical up-conversion properties.* Chemistry - A European Journal, 2009. **15**(41): p. 11010-11019.

[91] Li, Z. and Y. Zhang, *An efficient and user-friendly method for the synthesis of hexagonal-phase $NaYF_4$:Yb, Er/Tm nanocrystals with controllable shape and upconversion fluorescence.* Nanotechnology, 2008. **19**(34): p. 345606.

[92] Yang, K., F. Zheng, R. Wu, H. Li, and X. Zhang, *Upconversion luminescent properties of YVO_4:Yb^{3+}, Er^{3+} nano-powder by sol-gel method.* Journal of Rare Earths, 2006. **24**: p. 162-166.

[93] Vetrone, F., J.-C. Boyer, J.A. Capobianco, A. Speghini, and M. Bettinelli, *Significance of Yb^{3+} concentration on the upconversion mechanisms in codoped Y_2O_3:Er^{3+}, Yb^{3+} nanocrystals.* Journal of Applied Physics, 2004. **96**: p. 661-667.

[94] Qin, X., T. Yokomori, and Y. Ju, *Flame synthesis and characterization of rare-earth (Er^{3+}, Ho^{3+}, and Tm^{3+}) doped upconversion nanophosphors.* Applied Physics Letters, 2007. **90**(7): p. 073104.

[95] Lin, M., Y. Zhao, S.-Q. Wang, M. Liu, Z.-F. Duan, Y.-M. Chen, F. Li, F. Xu, and T.-J. Lu, *Recent advances in synthesis and surface modification of lanthanide-doped upconversion nanoparticles for biomedical applications.* Biotechnology Advances, 2012. **30**(6): p. 1551-1561.

[96] Boyer, J.C., F. Vetrone, L.A. Cuccia, and J.A. Capobianco, *Synthesis of colloidal upconverting $NaYF_4$ nanocrystals doped with Er^{3+}, Yb^{3+} and Tm^{3+}, Yb^{3+} via thermal decomposition of lanthanide trifluoroacetate precursors.* Journal of the American Chemical Society, 2006. **128**: p. 7444-7445.

[97] Boyer, J.C., L.A. Cuccia, and J.A. Capobianco, *Synthesis of colloidal upconverting $NaYF_4$:Er^{3+}/Yb^{3+} and Tm^{3+}/Yb^{3+} monodisperse nanocrystals.* Nano Letters, 2007. **7**: p. 847-852.

[98] F.Wang, D.K. Chatterjee, Z.Q. Li, Y. Zhang, X.P. Fan, and M.Q. Wang, *Synthesis of polyethylenimine/ $NaYF_4$ nanoparticles with upconversion fluorescence.* Nanotechnology, 2006. **17**: p. 5786-5791.

[99] Yi, G.S., H. Lu, S. Zhao, Y. Ge, W. Yang, D. Chen, and L.-H. Guo, *Synthesis, characterization and biological application of size-controlled nanocrystalline $NaYF_4$:Yb, Er infrared-to-visible up-conversion phosphors.* Nano Letters, 2004. **4**: p. 2191-2196.

[100] Yi, G.S. and G.M. Chow, *Synthesis of hexagonal-phase $NaYF_4$:Yb,Er and $NaYF_4$:Yb,Tm nanocrystals with efficient up-conversion fluorescence.* Advanced Functional Materials, 2006. **16**(18): p. 2324-2329.

[101] Li, Z. and Y. Zhang, *Monodisperse silica-coated polyvinylpyrrolidone/ $NaYF_4$ nanocrystals with multicolor upconversion fluorescence emission.* Angewandte Chemie International Edition, 2006. **45**(46): p. 7732-7735.

[102] Ong, L.C., M.K. Gnanasammandhan, S. Nagarajan, and Y. Zhang, *Upconversion: road to El Dorado of the fluorescence world.* Luminescence, 2012. **25**(4): p. 290-293.

[103] Xie, P. and S.C. Rand, *Visible cooperative upconversion laser in Er:$LiYF_4$.* Optics Letters, 1992. **17**(17): p. 1198-1200.

[104] Blumenthal, T., J. Meruga, P.S. May, J. Kellar, W. Cross, K. Ankireddy, S. Vunnam, and Q.N. Luu, *Patterned direct-write and screen-printing of NIR-to-visible upconverting inks for security applications.* Nanotechnology, 2012. **23**(18): p. 185305.

[105] Meruga, J.M., W.M. Cross, P.S. May, Q. Luu, G.A. Crawford, and J.J. Kellar, *Security printing of covert quick response codes using upconverting nanoparticle inks.* Nanotechnology, 2012. **23**(39): p. 395201.

[106] Liu, Y., K. Ai, and L. Lu, *Designing lanthanide-doped nanocrystals with both up- and down-conversion luminescence for anti-counterfeiting.* Nanoscale, 2011. **3**: p. 4804-4810.

[107] Gibart, P., F. Auzel, J.-C. Guillaume, and K. Zahraman, *Below band-gap IR response of substrate-free GaAs solar cells using two-photon up-conversion.* Japanese Journal of Applied Physics, 1996. **351**: p. 4401-4402.

[108] Shalav, A., B.S. Richards, T. Trupke, K.W. Kramer, and H.U. Gudel, *Application of $NaYF_4:Er^{3+}$ up-converting phosphors for enhanced near-infrared silicon solar cell response.* Applied Physics Letters, 2005. **86**(1): p. 013505.

[109] Richards, B.S. and A. Shalav, *Enhancing the near-infrared spectral response of silicon optoelectronic devices via up-conversion.* IEEE Transactions on Electron Devices, 2007. **54**: p. 2679-2684.

[110] Lim, S.F., R. Riehn, W.S. Ryu, N. Khanarian, C. Tung, D. Tank, and R.H. Austin, *In vivo and scanning electron microscopy imaging of upconverting nanophosphors in caenorhabditis elegans.* Nano Letters, 2006. **6**(2): p. 169-174.

[111] Nyk, M., R. Kumar, T.Y. Ohulchanskyy, E.J. Bergey, and P.N.Prasad, *High contrast in vitro and in vivo photoluminescence bioimaging using near infrared to near infrared up-conversion in Tm^{3+} and Yb^{3+} doped fluoride nanophosphors.* Nano Letters, 2008. **8**(11): p. 3834-3838.

[112] Idris, N.M., Z. Li, L. Ye, E.K.W. Sim, R. Mahendran, P.C.-L. Ho, and Y. Zhang, *Tracking transplanted cells in live animal using upconversion fluorescent nanoparticles.* Biomaterials, 2009. **30**(28): p. 5104-5113.

[113] Hampl, J., M. Hall, N.A. Mufti, Y.M. Yao, D.B. MacQueen, W.H. Wright, and D.E. Cooper, *Upconverting phosphor reporters in immunochromatographic assays.* Ananlytical Biochemistry, 2001. **288**(2): p. 176-187.

[114] Kuningas, K., T. Rantanen, T. Ukonaho, T. Lovgren, and T. Soukka, *Homogeneous assay technology based on upconverting phosphors.* Analytical Chemistry, 2005. **77**(22): p. 7348-7355.

[115] Hao, S., G. Chen, and C. Yang, *Sensing using rare-earth-doped upconversion nanoparticles.* Theranostics, 2013. **3**(5): p. 331-345.

[116] Kuperman, V., *Magnetic resonance imaging: physical principles and applications.* 2000, San Diego, California: Academic Press.

[117] Na, H.B., I.C. Song, and T. Hyeon, *Inorganic nanoparticles for MRI contrast agents.* Advanced Materials, 2009. **21**: p. 2133-2148.

[118] Reynolds, C.H., N. Annan, K. Beshah, J.H. Huber, S.H. Shaber, R.E. Lekinski, and J.A. Wortman, *Gadolinium-loaded nanoparticles: new contrast agents for magnetic resonance imaging.* Journal of the American Chemical Society, 2000. **122**: p. 8940-8945.

[119] Ren, W.T., L.B. Liang, F. Qi, Z.B. Sun, Z.Y. Yang, X.Q. Huang, Q.Z. Wu, H.Y. Zhu, X.F. Yu, H. Quan, and Q.Y. Gong, *Bimodal fluorescence and magnetic resonance imaging using water-soluble hexagonal $NaYF_4$:Ce,Tb,Gd nanocrystals.* Journal of Nanomaterials, 2011. **531217**.

[120] Wang, Y., L. Ji, B. Zhang, P. Yin, Y. Qiu, D. Song, J. Zhou, and Q. Li, *Upconverting rare-earth nanoparticles with a paramagnetic lanthanide complex shell for upconversion fluorescent and magnetic resonance dual-modality imaging.* Nanotechnology, 2013. **24**(17).

[121] Zhou, J., Y. Sun, X. Du, L. Xiong, H. Hu, and F. Li, *Dual-modality in vivo imaging using rare-earth nanocrystals with near-infrared to near-infrared (NIR-to-NIR) upconversion luminescence and magnetic resonance properties.* Biomaterials, 2010. **31**(12): p. 3287-3295.

[122] Kumar, R., M. Nyk, T.Y. Ohulchanskyy, C.A. Flask, and P.N.Prasad, *Combined optical and MR bioimaging using rare earth ion doped $NaYF_4$ nanocrystals.* Advanced Functional Materials, 2009. **19**(6): p. 853-859.

[123] Qiao, X.-F., J.-C. Zhou, J.-W. Xiao, Y.-F. Wang, L.-D. Sun, and C.-H. Yan, *Triple-functional core–shell structured upconversion luminescent nanoparticles covalently grafted with photosensitizer for luminescent, magnetic resonance imaging and photodynamic therapy in vitro.* Nanoscale, 2012. **4**: p. 4611-4623.

[124] Moser, F.H. and A.L. Thomas, *Phthalocyanine compounds*. 1963, New York: Reinhold publishing corporation.

[125] Herbst, W. and K. Hunger, *Industrial Organic Pigments: Production, Properties, Applications*. 3rd ed. 2004, Weinheim, Germany: Wiley-VCH Verlag GmbH & Co. KGaA.

[126] Linstead, R.P., *Phthalocyanines. Part I. New types of synthetic colouring matters.* Journal of the American Chemical Society, 1934: p. 1016-1017.

[127] Robertson, J.M., *An X-ray study of the structure of the phthalocyanines. Part I. The metal-free, nickel, copper, and platinum compounds.* Journal of the American Chemical Society, 1935: p. 615-621.

[128] Gregory, P., *Industrial applications of phthalocyanines.* Journal of Porphyrins and Phthalocyanines, 2000. **4**: p. 432-437.

[129] Wohrle, D., G. Schnurpfeil, S.G. Makarov, A. Kazarin, and O.N. Suvorova, *Practical applications of phthalocyanines – from dyes and pigments to materials for optical, electronic and photo-electronic devices.* Macroheterocycles, 2012. **5**(3): p. 191-202.

[130] Mustroph, H., M. Stollenwerk, and V. Bressau, *Current developments in optical data storage with organic dyes.* Angewandte Chemie International Edition, 2006. **45**: p. 2016-2055.

[131] Emmelius, M., G. Pawlowski, and H. Vollmann, *Materials for optical storage.* Angewandte Chemie International Edition, 1989. **28**(11): p. 1445-1471.

[132] Majumdar, H., A. Bandyopadhyay, and A.J. Pal, *Data-storage devices based on layer-by-layer self-assembled films of a phthalocyanine derivative.* Organic Electronics, 2003. **4**: p. 39-44.

[133] Zhao, F., F. Harnisch, U. Schroder, F. Scholz, P. Bogdanoff, and I. Herrman, *Application of pyrolysed iron(II) phthalocyanine and CoTMPP based oxygen reduction catalysts as cathode materials in microbial fuel cells.* Electrochemistry Communications, 2005. **7**: p. 1405-1410.

[134] Kaliya, O.L., E.A. Lukyanets, and G.N. Vorozhtsov, *Catalysis and photocatalysis by phthalocyanines for technology, ecology and medicine.* Journal of Porphyrins and Phthalocyanines, 1999. **3**: p. 592-610.

[135] Sorokin, A.B., *Phthalocyanine Metal Complexes in Catalysis.* Chemical Reviews, 2013. **113**: p. 8152-8191.

[136] Gokce, S., E.T. Saka, Z. Biyikhoglu, and H. Kantekin, *Synthesis, characterization of metal-free, metallophthalocyanines and catalytic activity of cobalt phthalocyanine in cyclohexene oxidation.* Synthetic Materials, 2013. **176**: p. 108-115.

[137] Torre, G.d.l., P. Vazquez, F. Agullo-Lopez, and T. Torres, *Phthalocyanines and related compounds: organic targets for nonlinear optical applications.* Journal of Materials Chemistry, 1998. **8**(8): p. 1671-1683.

[138] Petritsch, K., J.J. Dittmer, E.A. Marseglia, R.H. Friend, A. Lux, G.G. Rozenberg, S.C. Moratti, and A.B. Holmes, *Dye-based donor/acceptor solar cells.* Solar Energy Materials & Solar Cells, 2000. **61**: p. 63-72.

[139] Hohnholz, D., S. Steinbrecher, and M. Hanack, *Applications of phthalocyanines in organic light emitting devices.* Journal of Molecular Structure, 2000. **521**: p. 231-237.

[140] Patois, T., J.-B. Sanchez, F. Berger, P. Fievet, O. Segut, V. Moutarlier, M. Bouvet, and B. Lakard, *Elaboration of ammonia gas sensors based on electro deposited polypyrrole—cobalt phthalocyanine hybrid films.* Talanta, 2013. **117**: p. 45-54.

[141] Bouvet, M., P. Gaudillat, and J.-M. Suisse, *Phthalocyanine-based hybrid materials for chemosensing.* Journal of Porphyrins and Phthalocyanines, 2013. **17**: p. 913-919.

[142] Zhou, R., F. Josse, W. Gopel, Z.Z. Ozturk, and O. Bekaroglu, *Phthalocyanines as sensitive materials for chemical sensors.* Applied Organometallic Chemistry, 1996. **10**(8): p. 557-577.

[143] Liu, M.O., C. Tai, M. Sain, A.T. Hu, and F. Chou, *Photodynamic applications of phthalocyanines.* Journal of Photochemistry and Photobiology A: Chemistry, 2004. **165**: p. 131-136.

[144] Jancula, D., B. Marsalek, and P. Babica, *Photodynamic effects of 31 different phthalocyanines on a human keratinocyte cell line.* Chemosphere, 2013. **93**: p. 870-874.

[145] McKeown, N.B., *The synthesis of symmetrical phthalocyanines*, in *The Porphyrin Handbook*, K.M. Kadish, K.M. Smith, and R. Guilard, Editors. 2003, Academic Press: San Diego, California. p. 61-116.

[146] Uchida, H., P.Y. Reddy, S. Nakamura, and T. Toru, *Novel efficient preparative method for phthalocyanines from phthalimides and phthalic anhydride with HMDS.* Journal of Organic Chemistry, 2003. **68**: p. 8736-8738.

[147] Byrne, G.T., R.P. Linstead, and A.R. Lowe, *Phthalocyanines. Part II. The preparation of phthalocyanine and some metallic derivatives from o-cyanobenzamide and phthalimide.* Journal of the American Chemical Society, 1934: p. 1017-1022.

[148] Hurley, T.J., M.A. Robinson, and S.I. Trotz, *Complexes derived from 1,3-diiminoisoindoline-containing ligands. II. The stepwise formation of nickel phthalocyanine.* Inorganic Chemistry, 1967. **6**(2): p. 389-392.

[149] Linstead, R.P. and A.R. Lowe, *Phthalocyanines. Part III. Preliminary experiments on the preparation of phthalocyanines from phthalonitrile.* Journal of the American Chemical Society, 1934: p. 1022-1027.

[150] Thompson, J.A., K. Murata, D.C. Miller, J.L. Stanton, W.E. Broderick, B.M. Hoffman, and J.A. Ibers, *Synthesis of high-purity phthalocyanines (pc): high intrinsic conductivities in the molecular conductors H2(pc)I and Ni(pc)I.* Inorganic Chemistry, 1993. **32**(16): p. 3554-3556.

[151] Gurol, I., V. Ahsena, and O. Bekaroglu, *Synthesis of tetraalkylthio-substituted phthalocyanines and their complexation with Ag^{I} and Pd^{II}.* Journal of the Chemical Society, Dalton Transactions, 1994. p. 497-500.

[152] Snow, A.W., J.R. Griffith, and N.P. Marullo, *Syntheses and characterization of heteroatom-bridged metal-free phthalocyanine network polymers and model compounds.* Macromolecules, 1984. **17**: p. 1614-1624.

[153] Tomoda, H., S. Saito, S. Ogawa, and S. Shiraishi, *Synthesis of phthalocyanines from phthalonitrile with organic strong bases.* Chemistry Letters, 1980. **10**: p. 1277-1280.

[154] Rodriguez-Morgade, M.S., G.d.l. Torre, and T. Torres, *Design and synthesis of low symmetry phthalocyanines and related systems*, in *The Porphyrin Handbook*, K.M. Kadish, K.M. Smith, and R. Guillard, Editors. 2003, Academic Press: San Diego, California. p. 61-116.

[155] Idowu, M. and T. Nyokong, *Photophysicochemical and fluorescence quenching studies of tetra- and octa-carboxy substituted silicon and germanium phthalocyanines.* Journal of Photochemistry and Photobiology A: Chemistry, 2009. **204**(1): p. 63-68.

[156] Shaposhnikov, G.P., V.E. Maizlish, and V.P. Kunlinich, *Carboxy-substituted phthalocyanine metal complexes.* Russian Journal of General Chemistry, 2004. **75**(9): p. 1480-1488.

[157] Jin, L., W. Chen, and D. Chen, *Synthesis and photovoltaic properties of octacarboxy-metallophthalocyanine dyes applied in dye-sensitized solar cells.* Journal of the Serbian Chemical Society, 2012. **77**(9): p. 1223-1237.

[158] Malinga, N., O. Dolotova, R. Bulgakov, E. Antunes, and T. Nyokong, *Synthesis and physicochemical behaviour of aluminium trikis and tetrakis (diaquaplatinum) octacarboxyphthalocynine.* Dyes and Pigments, 2012. **95**(3): p. 572-579.

[159] Modisha, P., E. Antunes, J. Mack, and T. Nyokong, *Improvement of the photophysical parameters of zinc octacarboxy phthalocyanine upon conjugation to magnetic nanoparticles.* International Journal of Nanoscience, 2013. **12**(2): p. 1350010.

[160] George, R.D., A.W. Snow, J.S. Shirk, and W.R. Barger, *The alpha susbstitution effect on phthalocyanine aggregation.* Journal of Porphyrins and Phthalocyanines, 1998. **2**(1): p. 1-7.

[161] Hone, D.C., P.I. Walker, R. Evans-Gowing, S. FitzGerald, A. Beeby, I. Chambrier, M.J. Cook, and D.A. Russel, *Generation of cytotoxic singlet oxygen via phthalocyanine-stabilized gold nanoparticles: a potential delivery vehicle for photodynamic therapy.* Langmuir, 2002. **18**: p. 2985-2987.

[162] Kotiaho, A., R. Lahtinen, A. Efimov, H.-K. Metsberg, E. Sariola, H. Lehtivuori, N.V. Tkachenko, and H. Lemmetyinen, *Photoinduced charge and energy transfer in phthalocyanine-functionalized gold nanoparticles.* Journal of Physical Chemistry C, 2009. **114**(1): p. 162-168.

[163] Mack, J. and M.J. Stillman, *Electronic structures of metal phthalocyanine and porphyrin complexes from analysis of the uv–visible absorption and magnetic circular dichroism spectra and molecular orbital calculations*, in *The Porphyrin Handbook*, K.M. Kadish, K.M. Smith, and R. Guilard, Editors. 2003, Academic Press: San Diego, California. p. 43-113.

[164] Dini, D. and M. Hanack, *Physical Properties of Phthalocyanine-based Materials*, in *The Porphyrin Handbook: Phthalocyanines: Properties and Materials*, K.M. Kadish, K.M. Smith, and R. Guilard, Editors. 2003, Academic Press: San Diego, California. p. 1-36.

[165] Gouterman, M., G.H. Wagniere, and L.C. Snyder, *Spectra of porphyrins Part II. Four orbital model.* Journal of Molecular Spectroscopy, 1963. **11**(1-6): p. 108-127.

[166] Nyokong, T. and H. Isago, *The renaissance in optical spectroscopy of phthalocyanines and other tetraazaporphyrins.* Journal of Porphyrins and Phthalocyanines, 2004. **8**: p. 1083-1090.

[167] Handa, M., A. Suzuki, S. Shoji, K. Kasuga, and K. Sogabe, *Spectral and electrochemical properties of vanadyl hexadecafluorophthalocyanine.* Inorganica Chimica Acta, 1995. **230**(1): p. 41-44.

[168] Dolotova, O.V., N.I. Bundina, O.L. Kaliya, and E.A. Lukyanets, *Manganese phthalocyanine coordination chemistry: recent results and present status.* Journal of Porphyrins and Phthalocyanines, 1997. **1**(4): p. 355-366.

[169] Nyokong, T. and E. Antunes, *Photochemical and Photophysical Properties of Metallophthalocyanines*, in *Handbook of Porphyrin Science: Physicochemical characterization*, K.M. Kadish, K.M. Smith, and R. Guilard, Editors. 2010, World Scientific: Singapore. p. 247-258.

[170] Forteath, S., E. Antunes, W. Chidawanyika, and T. Nyokong, *Unquenched fluorescence lifetime for beta-phenylthio substituted zinc phthalocyanine upon conjugation to gold nanoparticles.* Polyhedron, 2012. **34**: p. 114-120.

[171] Chidawanyika, W., C. Litwinski, E. Antunes, and T. Nyokong, *Photophysical study of a covalently linked quantum dot - low symmetry phthalocyanine conjugate.* Journal of Photochemistry and Photobiology A: Chemistry, 2010. **212**(1): p. 27-35.

[172] Masilela, N., E. Antunes, and T. Nyokong, *Axial coordination of zinc and silicon phthalocyanines to silver and gold nanoparticles: an investigation of their photophysicochemical and antimicrobial behaviour*. Journal of Porphyrins and Phthalocyanines, 2013. **17**: p. 417-430.

[173] Zhang, X.F. and H.J. Xu, *Influence of halogenation and aggregation on photosensitizing properties of zinc phthalocyanine (ZnPc).* Journal of the Chemical Society, Faraday Transactions, 1993. **89**(18): p. 3347-3351.

[174] Idowu, M., A. Ogunsipe, and T. Nyokong, *Excited state dynamics of zinc and aluminium phthalocyanine carboxylates.* Spectrchimica Acta Part A, 2007. **68**: p. 995-999.

[175] Snow, A.W., *Phthalocyanine Aggregation*, in *The Porphyrin Handbook*, K.M. Kadish, K.M. Smith, and R. Guilard, Editors. 2003, Academic Press: San Diego, California. p. 129-176.

[176] Kasha, M., *Energy transfer mechanisms and the molecular exciton model for molecular aggregates.* Radiation Research, 1963. **20**: p. 55-71.

[177] Kasha, M., H.R. Rawls, and M.A. El-Bayoumi, *The exciton model in molecular spectroscopy.* Pure and Applied Chemistry, 1965. **11**(3-4): p. 371-392.

[178] Gumus, G., A. Gul, and V. Ahsen, *Synthesis and characterization of new soluble metallo-phthalocyanines with bulky substituents.* New Journal of Chemistry, 1997. **21**: p. 589-594.

[179] DeRosa, M.C. and R.J. Crutchley, *Photosensitized singlet oxygen and its applications.* Coordination Chemistry Reviews, 2002. **233-234**: p. 351-371.

[180] Clennan, E.L. and A. Pace, *Advances in singlet oxygen chemistry.* Tetrahedron, 2005. **61**(28): p. 6665-6691.

[181] Davies, M.J., *Singlet oxygen-mediated damage to proteins and its consequences.* Biochemical and Biophysical Research Communications, 2003. **305**: p. 761-770.

[182] Grossweiner, L.I., *The Science of Phototherapy: An Introduction*. 2005, Dordrecht, The Netherlands: Springer.

[183] Durmus, M., *Photochemical and Photophysical Characterization*, in *Photosensitizers in Medicine, Environment, and Security*, T. Nyokong and V. Ahsen, Editors. 2012, Springer: Heidelberg. p. 135-266.

[184] Ogilby, P.R. and C.S. Foote, *Chemistry of singlet oxygen. 42. Effect of solvent, solvent isotopic substitution, and temperature on the lifetime of singlet molecular oxygen.* Journal of the American Chemical Society, 1983. **105**: p. 3423-3430.

[185] Staicu, A., A. Pascu, A. Nuta, A. Sorescu, V. Raditoiu, and M.L. Pascu, *Studies about phthalocyanine photosensitizers to be used in photodynamic therapy.* Romanian Reports in Physics, 2013. **65**(3): p. 1032-1051.

[186] Dolmans, D.E.J., D. Fukumura, and R.K. Jain, *TIMELINE: Photodynamic therapy for cancer.* Nature Reviews Cancer, 2003. **3**(5): p. 380-388.

[187] Bown, S.G., A.Z. Rogowska, D.E. Whitelaw, W.R. Lees, L.B. Lovat, P. Ripley, L. Jones, P. Wyld, A. Gillams, and A.W.R. Hatfield, *Photodynamic therapy for cancer of the pancreas.* Gut, 2002. **50**(4): p. 549-557.

[188] Dimofte, A., T.C. Zhu, S.M. Hahn, and R.A. Lustig, *In vivo light dosimetry for motexafin lutetium-mediated PDT of recurrent breast cancer.* Lasers in Surgery and Medicine, 2002. **31**(5): p. 305-312.

[189] Biel, M.A., *Photodynamic therapy and the treatment of head and neck neoplasia.* The Laryngoscope, 2009. **108**(9): p. 1259-1268.

[190] Gomer, C.J., J.V. Jester, N.J. Razum, B.C. Szirth, and A.L. Murphree, *Photodynamic therapy of intraocular tumors, examination of hematoporphyrin derivative distribution and long-term damage in rabbit ocular tissue.* Cancer Research, 1985. **45**: p. 3718-3725.

[191] McCaughan, J.S., W. Hicks, L.Laufman, E. May, and R. Roach, *Palliation of esophageal malignancy with photoradiation therapy.* Cancer 1984. **54**(12): p. 2905-2910.

[192] Barr, H., N. Krasner, P.B. Boulos, P. Chatlani, and S.G. Brown, *Photodynamic therapy for colorectal cancer: A quantitative pilot study.* British Journal of Surgery, 1990. **77**(1): p. 93-96.

[193] Popovic, E.A., A.H. Kaye, and J.S. Hill, *Photodynamic therapy of brain tumors.* Journal of Clinical Laser Medicine and Surgery, 1996. **14**(5): p. 251-261.

[194] Mang, T.S., R. Allison, G. Hewson, W. Snider, and R. Moskowitz, *A phase II/III clinical study of tin ethyl etiopurpuri (Purlytin)-induced photodynamic therapy for the treatment of recurrent cutaneous metastatic breast cancer.* Cancer Journal from Scientific American, 1998. **4**(6): p. 378-84.

[195] Hoff, D.D.V., R. Schilsky, C.M. Reichert, R.L. Reddick, M. Rozencweiq, R.C. Young, and F.M. Muggia, *Toxic effects of cis-dichlorodiammineplatinum(II) in man.* Cancer Treatment Reports, 1979. **63**(9-10): p. 1527-1531.

[196] Moan, J. and K. Berg, *The photodegradation of porphyrins in cells can be used to estimate the lifetime of singlet oxygen.* Photochemistry and Photobiology, 1991. **53**(4): p. 549-553.

[197] Sternberg, E.D., D. Dolphin, and C. Bruckner, *Porphyrin-based photosensitizers for use in photodynamic therapy.* Tetrahedron, 1998. **54**: p. 4151-4202.

[198] Sekkat, N., H.v.d. Bergh, T. Nyokong, and N. Lange, *Like a bolt from the blue: phthalocyanines in biomedical optics.* Molecules, 2012. **17**: p. 98-144.

[199] Uspenskii, L.V., L.V. Christov, E.A. Kogan, V.B. Loshchenov, I.A. Ablitsov, V.K. Rybin, V. Zavodnov, D.I. Shiktorov, N.F. Serbinenko, and I.G. Semenova, *Endobronchial laser therapy in complex preoperative preparation of patients with lung diseases.* Khirugiia, 2000. **2**: p. 38-40.

[200] Miller, J.D., E.D. Baron, H. Scull, A. Hsia, J.C. Berlin, T. McCormick, V. Colussi, M.E. Kenney, K.D. Cooper, and N.L. Oleinick, *Photodynamic therapy with the phthalocyanine photosensitizer Pc 4: the case experience with preclinical mechanistic and early clinical–translational studies.* Toxicology and Applied Pharmacology, 2007. **224**(3): p. 290-299.

[201] Guo, Y., M. Kumar, and P. Zhang, *Nanoparticle-based photosensitizers under CW infrared excitation.* Chemical Materials, 2007. **19**(25): p. 6071-6072.

[202] Liu, K., X. Liu, Q. Zeng, Y. Zhang, L. Tu, T. Liu, X. Kong, Y. Wang, F. Cao, S.A.G. Lambrechts, M.C.G. Aalders, and H. Zhang, *Covalently assembled NIR nanoplatform for simultaneous fluorescence imaging and photodynamic therapy of cancer cells.* ACS Nano, 2012. **6**(5): p. 4054-4062.

[203] Ungun, B., R.K. Prud'homme, S.J. Budijono, J. Shan, S.F. Lim, Y. Ju, and R. Austin, *Nanofabricated upconversion nanoparticles for photodynamic therapy.* Optics Express, 2009. **17**(1): p. 80-86.

[204] Shan, J., S.J. Budijono, G. Hu, N. Yao, Y. Kang, Y. Ju, and R.K. Prud'homme, *Pegylated composite nanoparticles containing upconverting phosphors and meso-tetraphenyl porphine (TPP) for photodynamic therapy.* Advanced Functional Materials, 2011. **21**(13): p. 2488-2495.

[205] Idris, N.M., M.K. Gnanasammandhan, J. Zhang, P.C. Ho, R. Mahendran, and Y. Zhang, *In vivo photodynamic therapy using upconversion nanoparticles as remote-controlled nanotransducers.* Nature, 2012. **18**(10): p. 1580-1586.

[206] Zhang, P., W. Steelant, M. Kumar, and M. Scholfield, *Versatile photosensitizers for photodynamic therapy at infrared excitation.* Journal of the American Chemical Society, 2007. **129**(15): p. 4526-4527.

[207] Park, Y.I., H.M. Kim, J.H. Kim, K.C.Moon, B. Yoo, K.T.Lee, N.Lee, Y. Choi, W. Park, D. Ling, K. Na, W.K. Moon, S.H. Choi, H.S. Park, S.-Y. Yoon, Y.D. Suh, S.H. Lee, and T. Hyeon, *Theranostic probe based on lanthanide-doped nanoparticles for simultaneous in vivo dual-modal imaging and photodynamic therapy.* Advanced Materials, 2012. **24**(42): p. 5755-5761.

[208] Tian, G., W. Ren, L. Yan, S. Jian, Z. Gu, L. Zhou, S. Jin, W. Yin, S. Li, and Y. Zhao, *Red-emitting upconverting nanoparticles for photodynamic therapy in cancer cells under near-infrared excitation.* Small, 2012. **9**(11): p. 1929-1938.

[209] Wang, C., H. Tao, L. Cheng, and Z. Liu, *Near-infrared light induced in vivo photodynamic therapy of cancer based on upconversion nanoparticles.* Biomaterials, 2011. **32**(26): p. 6145-6154.

[210] Zhou, A., Y. Wei, B. Wu, Q. Chen, and D. Xing, *Pyropheophorbide A and c(RGDyK) comodified chitosan-wrapped upconversion nanoparticle for targeted near-infrared photodynamic therapy.* Molecular Pharmaceutics, 2012. **9**(6): p. 1580-1589.

[211] Chen, F., S. Zhang, W. Bu, Y. Chen, Q. Xiao, J. Liu, H. Xing, L. Zhou, W. Peng, and J. Shi, *A uniform sub-50 nm-sized magnetic/ upconversion fluorescent bimodal imaging agent capable of generating singlet oxygen by using a 980 nm laser.* Chemistry - A European Journal, 2012. **18**(23): p. 7082-7090.

[212] Gu, Z., L. Yan, G. Tian, S. Li, Z. Chai, and Y. Zhao, *Recent advances in design and fabrication of upconversion nanoparticles and their safe theranostic applications.* Advanced Materials, 2013. **25**(28): p. 3758-3779.

[213] Zhao, Z., Y. Han, C. Lin, D. Hu, F. Wang, X. Chen, Z. Chen, and N. Zheng, *Multifunctional core–shell upconverting nanoparticles for imaging and photodynamic therapy of liver cancer cells.* Chemistry an Asian Journal 2012. **7**: p. 830-837.

[214] Chatterjee, D.K. and Z. Yong, *In vivo photodynamic therapy using upconversion nanoparticles as remote-controlled nanotransducers.* Nanomedicine, 2008. **3**(1): p. 73-82.

[215] Qian, H.S., H.C. Guo, P.C.-L. Ho, R. Mahendran, and Y. Zhang, *Mesoporous-silica-coated up-conversion fluorescent nanoparticles for photodynamic therapy.* Small, 2009. **5**(20): p. 2285-2290.

[216] Guo, H., H. Qian, N.M. Idris, and Y. Zhang, *Singlet oxygen-induced apoptosis of cancer cells using upconversion fluorescent nanoparticles as a carrier of photosensitizer.* Nanomedicine: Nanotechnology, Biology, and Medicine, 2010. **6**: p. 486-495.

[217] Cui, S., H. Chen, H. Zhu, J. Tian, X. Chi, Z. Qian, S. Achilefu, and Y. Gu, *Amphiphilic chitosan modified upconversion nanoparticles for in vivo photodynamic therapy induced by near-infrared light.* Journal of Materials Chemistry, 2012. **22**: p. 4861-4873.

[218] Lim, M.E., Y. Lee, Y. Zhang, and J.J.H. Chu, *Photodynamic inactivation of viruses using upconversion nanoparticles.* Biomaterials, 2012. **33**: p. 1912-1920.

[219] Cui, S., D. Yin, Y. Chen, Y. Di, H. Chen, Y. Ma, S. Achilefu, and Y. Gu, *In vivo targeted deep-tissue photodynamic therapy based on near-infrared light triggered upconversion nanoconstruct.* ACS Nano, 2013. **7**(1): p. 676-688.

[220] Wang, Y., H. Wang, D. Liu, S. Song, X. Wang, and H. Zhang, *Graphene oxide covalently grafted upconversion nanoparticles for combined NIR mediated imaging and photothermal/ photodynamic cancer therapy.* Biomaterials, 2013. **34**: p. 7715-7724.

[221] Ogunsipe, A., D. Maree, and T. Nyokong, *Solvent effects on the photophysical and fluorescence properties of zinc phthalocyanine derivatives.* Journal of Molecular Structure, 2003. **650**(1-3): p. 131-140.

[222] Johnson, N.J.J., N.M. Sangeetha, J.C. Boyer, and F.C.J.M.v. Veggel, *Facile ligand-exchange with polyvinylpyrrolidone and subsequent silica coating of hydrophobic upconverting beta-$NaYF_4$:Yb^{3+}/Er^{3+} nanoparticles.* Nanoscale, 2010. **2**: p. 771-777.

[223] Chang, J.H., K.H. Kang, J. Choi, and Y.K. Jeong, *High efficiency protein separation with organosilanes assembled silica-coated magnetic nanoparticles.* Superlattices and Microstructures, 2008. **44**: p. 442-448.

[224] Kobayashi, N., H. Ogata, N. Nonaka, and E.A. Luk'yanets, *Effect of peripheral substitution on the electronic absorption and fluorescence spectra of metal-free and zinc phthalocyanines.* Chemistry-A European Journal, 2003. **9**: p. 5123-5134.

[225] Sakamoto, K. and E. Ohno, *Synthesis and electron transfer property of phthalocyanine derivatives.* Progress in Organic Coatings, 1997. **31**: p. 139-145.

[226] Lundberg, J.O., M. Carlstrom, F.J. Larsen, and E. Weitzberg, *Roles of dietary inorganic nitrate in cardiovascular health and disease.* Cardiovascular Research, 2011. **89**(3): p. 525-532.

[227] Bonacci, G., P.R.S. Baker, S.R. Salvatore, D. Shores, N.K.H. Khoo, J.R. Koenitzer, D.A. Vitturi, S.R. Woodcock, F. Golin-Bisello, M.P. Cole, S. Watkins, C.S. Croix, C.I. Batthyany, B.A. Freeman, and F.J. Schopfer, *Conjugated linoleic acid is a preferential substrate for fatty acid nitration.* Journal of Biological Chemistry, 2012. **287**(53): p. 44071-44082.

[228] Na, H., K. Woo, and K. Lim, *Rational morphology control of b-$NaYF_4$:Yb,Er/Tm upconversion nanophosphors using a ligand, an additive, and lanthanide doping.* Nanoscale, 2013. **4**: p. 4242-4251.

[229] Sanjalal, P.R., T.S. Sreeprasad, A.K. Samal, and T. Pradeep, *Anisotropic nanomaterials: structure, growth, assembly, and functions.* Nano Reviews, 2011. **2**: p. 5883-5945.

[230] Viswanatha, R. and D.D. Sarma, *Growth of nanocrystals in solution*, in *Nanomaterials Chemistry: Recent Developments and New Directions*, C.N.R. Rao, A. Muller, and A.K. Cheetham, Editors. 2007, Wiley-VHC: Weinheim, Germany. p. 139-170.

[231] Zhang, F., Y. Wan, T. Yu, F. Zhang, Y. Shi, S. Xie, Y. Li, L. Xu, B. Tu, and D. Zhao, *Uniform nanostructured arrays of sodium rare-earth fluorides for highly efficient multicolor upconversion luminescence.* Angewandte Chemie International Edition, 2007. **46**: p. 7976-7979.

[232] Zeng, S., G. Ren, C. Xu, and Q. Yang, *High uniformity and monodispersity of sodium rare-earth fluoride nanocrystals: controllable synthesis, shape evolution and optical properties.* Crystal Engineering Communications, 2010. **13**: p. 1384-1390.

[233] Shan, J., N. Yao, and Y. Ju, *Phase transition induced formation of hollow structures in colloidal lanthanide-doped $NaYF_4$ nanocrystals.* Journal of Nanoparticle Research, 2009. **12**(4): p. 1429-1438.

[234] Kakani, S.L., *Material Science*. 2006, New Delhi: New Age International.

[235] Liu, G., C.E. Conn, and C.J. Drummond, *Lanthanide oleates: chelation, self-assembly, and exemplification of ordered nanostructured colloidal contrast agents for medical imaging.* Journal of Physical Chemistry B, 2009. **113**: p. 15949-15959.

[236] Langford, J.I. and A.J.C. Wilson, *Scherrer after sixty years: a survey and some new results in the determination of crystallite size.* Journal of Applied Crystallography, 1978. **11**: p. 102-113.

[237] Renero-Lecuna, C., R. Martin-Rodriguez, R. Valiente, J. Gonzalez, F. Rogriguez, K.W. Kramer, and H.U. Gudel, *Origin of the high upconversion green luminescence efficiency in β-$NaYF_4$:2%Er^{3+},20%Yb^{3+}*. Chemical Materials, 2011. **23**: p. 3442-3448.

[238] Kramer, K.W., D. Biner, G. Frei, H.U. Gudel, M.P. Hehlen, and S.R. Luthi, *Hexagonal sodium yttrium fluoride based green and blue emitting upconversion phosphors.* Chemical Materials, 2004. **16**(7): p. 1244-1251.

[239] Burns, J.H., *Crystal structure of hexagonal sodium neodymium fluoride and related compounds.* Inorganic Chemistry, 1965. **4**(881-886).

[240] Baker, J.M., *EPR and ENDOR in the lanthanides*, in *Electron Spin Resonance Part 2*, M.C.R. Symons, Editor. 1993, Royal Society of Chemistry: Cambridge. p. 131-177.

[241] Komban, R., J.P. Klare, B. Voss, J. Nordmann, H.J. Steinhoff, and M. Haase, *An electron paramagnetic resonance spectroscopic investigation on the growth mechanism of $NaYF_4$:Gd nanocrystals.* Angewandte Chemie International Edition, 2012. **51**: p. 6506-6510.

[242] Jadhav, N.V., A.I. Prasad, A. Kumar, R.Mishra, S. Dhara, K.R. Babu, C.L. Prajapat, N.L. Misra, R.S. Ningthoujam, B.N. Pandey, and R.K. Vatsa, *Synthesis of oleic acid functionalized Fe_3O_4 magnetic nanoparticles and studying their interaction with tumor cells for potential hyperthermia applications.* Colloids and Surfaces B: Biointerfaces, 2013. **108**: p. 158-168.

[243] D.Yuan, M.C. Tan, R.E. Riman, and G.M. Chow, *Comprehensive study on the size effects of the optical properties of $NaYF_4$:Yb,Er nanocrystals.* Journal of Physical Chemistry C, 2013. **117**: p. 13297-13304.

[244] Shan, J., M. Uddi, R. Wei, N. Yao, and Y. Ju, *The hidden effects of particle shape and criteria for evaluating the upconversion luminescence of the lanthanide doped nanophosphors.* Journal of Physical Chemistry C, 2010. **114**: p. 2452-2461.

[245] Zhao, C., X. Kong, X. Liu, L. Tu, F. Wu, Y. Zhang, K. Liu, Q. Zeng, and H. Zhang, *Li^+ ion doping: an approach for improving the crystallinity and upconversion emissions of $NaYF_4$:Yb^{3+}, Tm^{3+} nanoparticles.* Nanoscale, 2013. **5**: p. 8084-8089.

[246] Wang, J., F. Wang, J. Xu, Y. Wang, Y. Liu, X. Chen, H. Chen, and X. Liu, *Lanthanide-doped $LiYF_4$ nanoparticles: synthesis and multicolor upconversion tuning.* Compus Rendus Chimie, 2010. **13**: p. 731-736.

[247] Schietinger, S., T. AIchele, H. Wang, T. Nann, and O. Benson, *Plasmon-enhanced upconversion in single $NaYF_4$:Yb^{3+}/Er^{3+} codoped nanocrystals.* Nano Letters, 2012. **10**: p. 134-138.

[248] Wlodarczyk, J. and B. Kierdaszuk, *Interpretation of fluorescence decays using a power-like model.* Biophysical Journal, 2003. **85**(1): p. 589-598.

[249] Chakrabarty, M.M., *Chemistry and technology of oils and fats*. 2003, New Dehli: Allied Publishers.

[250] R.Koole, M.M.v. Schooneveld, J. Hilhorst, C.d.M. Donega, D.C.t. Hart, A.v. Blaaderen, D. Vanmaekelbergh, and A. Meijerink, *On the incorporation mechanism of hydrophobic quantum dots in silica spheres by a reverse microemulsion method.* Chemical Materials, 2008. **20**: p. 2503-2512.

[251] Mayo, D.W., F.A. Miller, and R.W. Hannah, *Course notes on the interpretation of infrared and raman spectra*. 2003, Hoboken, New Jersey: John Wiley and Sons.

[252] Hebbink, G.A., J.W. Stouwdam, D.N. Reinhoudt, and F.C.J.M.v. Veggel, *Lanthanide (III) - doped nanoaprticles that emit in the near-infrared.* Advanced Materials, 2002. **14**(16): p. 1147-1150.

[253] Zou, W., C. Visser, J.A. Maduro, M.S. Pshenichnikov, and J.C. Hummelen, *Broadband dye-sensitized upconversion of near infrared light.* Nature Photonics, 2012. **6**: p. 560-564.

[254] Nombona, N., E. Antunes, C. Litwinski, and T. Nyokong, *Synthesis and photophysical studies of phthalocyanine-gold nanoparticle conjugates.* Dalton Transactions, 2011. **40**(44): p. 11876-11884.

[255] Birch, D.J.S. and R.E. Imhof, *Time-domain fluorescence spectroscopy using time correlated single photon counting*, in *Topics in Fluorescence Spectroscopy: Techniques*, J.R. Lakowicz, Editor. 1991, Kluwer Academic Publishers: New York. p. 1-96.

[256] Okura, I., *Photosensitization of Porphyrins and Phthalocyanines*. 2000, Tokyo: Kodansha.

[257] Vukovic, S., S. Corni, and B. Mennucci, *Fluorescence enhancement of chromophores close to metal nanoparticles. Optimal setup revealed by the polarizable continuum model.* Journal of Physical Chemistry C, 2009. **113**: p. 121-133.

[258] Seybold, P.G. and M. Gouterman, *Porphyrins: XIII: Fluorescence spectra and quantum yields.* Journal of Molecular Spectroscopy, 1969. **31**: p. 1-13.

[259] Clegg, R.M., *Fluorescence resonance energy transfer*. Current Opinion in Biotechnology, 1995. **6**: p. 103-110.

[260] Boyer, J.C. and F.C.J.M.v. Veggel, *Absolute quantum yield measurements of colloidal $NaYF_4:Er^{3+},Yb^{3+}$ upconverting nanoparticles.* Nanoscale, 2010. **2**: p. 1417-1419.

[261] Hasty, N., P.B. Merkel, P. Radlick, and D.R. Kearns, *Role of azide in singlet oxygen reactions: reaction of azide with singlet oxygen.* Tetrahedron Letters, 1972. **13**(1): p. 49-52.

[262] Kearns, D.R., *Physical and chemical properties of singlet molecular oxygen.* Chemical Reviews. **71**(4): p. 395-427.

[263] Bonnett, R. and G. Martinez, *Photobleaching of sensitizers used in photodynamic therapy.* Tetrahedron Letters, 2001. **57**: p. 9513-9547.

[264] Jiang, L., A. Glidle, A. Griffith, C.J. McNeil, and J.M. Cooper, *Characterising the formation of a bioelectrochemical interface at a self-assembled monolayer using X-ray photoelectron spectroscopy.* Bioelectrochemistry and Bioenergetics, 1997. **42**: p. 15-23.

[265] Cong, F.-D., G. Gao, J.-X. Li, G.-Q. Huang, Z. Wei, F.-Y. Yu, X.-G. Du, and K.-Z. Xing, *Synthesis and aggregation study of optically active tetra-beta-[(S)-2-octanyloxy]-substituted copper and nickel phthalocyanines.* Journal of Chemical Sciences, 2010. **122**(6): p. 813-818.

[266] Kotiaho, A., R. Lahtinen, A. Efimov, H.-K. Metsberg, E. Sariola, H. Lehtivuori, N.V. Tkachenko, and H. Lemmetyinen, *Photoinduced charge and energy transfer in phthalocyanine-functionalized gold nanoparticles.* Journal of Physical Chemistry C, 2010. **114**(1): p. 162-168.

[267] Zhang, F. and M.P. Srinivasan, *Self-assembled molecular films of aminosilanes and their immobilization capacities.* Langmuir, 2004. **20**: p. 2309-2314.